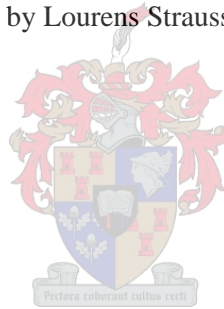


Modelling of 3D structures in fire as skeletal frames using the Fire Beam Element (FBE) for simplified analysis and design

by Lourens Strauss



*Thesis presented in partial fulfilment of the requirements for the degree of
Master of Engineering in the Faculty of Engineering, Stellenbosch University*

Supervisor: Prof. Richard S. Walls

Date: March 2021

Declaration

By submitting this thesis electronically, I declare that the entirety of the work contained therein is my own, original work, that I am the sole author thereof (save to the extent explicitly otherwise stated), that reproduction and publication thereof by Stellenbosch University will not infringe any third party rights and that I have not previously in its entirety or in part submitted it for obtaining any qualification.

Signature:

Date: March 2021

Copyright © 2021 Stellenbosch University of Stellenbosch

All rights reserved

Abstract

In recent years performance-based design has become more popular in structural fire engineering as it often leads to more cost effective and safe designs. Real incidents, such as the Broadgate fire in 1990, and large-scale experiments, such as the Cardington tests, have shown that composite structures have significantly higher resistance in fire than what is typically predicted by prescriptive designs based on isolated members. However, performance-based design tools require significant expertise and computational effort. Simplified tools, such as the Fire Beam Element (FBE) methodology and the Slab Panel Method (SPM), can individually be used to analyse the skeletal frame of a structure in fire or composite floor panels respectively. However, few tools exist for consulting engineers to be able to comprehensively, but efficiently, consider global structural analyses for fire.

The FBE methodology is based on a finite element that has a movable Neutral Axis (NA) and can consider material and geometric nonlinearity. In this research the FBE methodology is extended to include a three-dimensional (3D) beam element and is implemented in a finite element software, OpenSees, so that it could be applied to 3D skeletal composite structures. The SPM is a design tool for composite slabs that considers the concrete deck and unprotected secondary beams as a whole. In the SPM, the ultimate load-carrying capacity is calculated for the slab panel taking into account the Tensile Membrane Action (TMA) mechanism that develops due to large deformations of the slab panel. In this thesis, a design methodology is proposed linking the FBE methodology with the SPM. In the proposed design methodology, the composite slab and the supporting skeletal structure are considered as two separate systems which are able to interact with each other.

The 3D FBE design methodology is validated with three-case studies, obtained in literature, which are used to validate the behaviour of the supporting skeletal structure. The case-studies show that the 3D FBE is able to capture the behaviour of the structure where the Bernoulli-Euler assumption holds, and typically shows good correlations between FBE and literature supplied deformations. The second case study investigated indicates that continuity should be taken into account when determining the yieldline pattern and load distribution to the support beams. The third case study highlights a limitation of the FBE analysis that is applicable when the primary support beams lose their strength, and the loads are carried through Membrane Action.

Lastly, the FBE and SPM design methodology are applied to a ten-storey office building which provides a proof of concept of the overall design methodology. The results obtained from the FBE analysis demonstrated the behaviour of the supporting skeletal structure and the impact that the rest of the structure has on the support beams. The ultimate load-carrying capacity of the slab panel are calculated with the updated edge deflection determined with the FBE analysis. It is highlighted how SPM predictions can be updated based on improved information regarding perimeter supporting beam deflections.

Opsomming

In die afgelope jare, het prestasie-gebaseerde ontwerp gewilder geword in struktuur brand ingenieurswese aangesien dit dikwels tot meer koste-effektiewe en veilige ontwerpe lei. Werklike voorvalle, soos die Broadgate-brand in 1990, en grootskaalse toetse, soos die Cardington toetse, het getoon dat saamgestelde strukture aansienlike hoër brandweerstand het as wat tipies voorspel word deur voorskriftelike ontwerpe op geïsoleerde lede. Prestasie-gebaseerde ontwerp hulpmiddels vereis egter beduidende kundigheid en berekeningspoging. Vereenvoudigde hulpmiddels, soos die Brand-Balk Element (FBE) metodologie en die Blad Paneel Metode (SPM) kan op hul eie beurt gebruik word om die skeletstruktuur van 'n struktuur in brand te of om saamgestelde vloer panele te analiseer. Daar is egter min hulpmiddels vir raadplegende ingenieurs wat in 'n omvattende, maar doeltreffende, die globale struktuur analise vir brand kan in ag neem.

Die FBE metodologie is gebaseer op 'n eindige element wat 'n mobiele Neutrale As (NA) het en die materiaal en geometriese nie-lineariteit in ag kan neem. In die navorsing word die FBE metodologie uitgebrei om 'n drie-dimensionale (3D) balk-element in te sluit en word geïmplementeer in eindige element sagteware, OpenSees, sodat dit toegepas kan word om 3D skelet strukture te analiseer. Die SPM is 'n ontwerp hulpmiddel vir saamgestelde blaaie wat die betonblad en onbeskermdes sekondêre balke as 'n geheel in ag neem. In die SPM word die lasdraende kapasiteit van die blad paneel bereken deur om die Trekmembraanwerking (TMA), wat veroorsaak word deur die groot vervorming van die blad paneel, in ag te neem. In die tesis word 'n ontwerp metodologie voorgestel wat die FBE metodologie met die SPM verbind. In die voorgestelde ontwerp metodologie word die saamgestelde blad en die ondersteunings skelet struktuur as twee aparte sisteme geag wat met mekaar kan kommunikeer.

Die 3D FBE ontwerp metodologie wat gebruik word om is deur drie gevallestudies, uit die literatuur, bevestig. Die gevallestudies het getoon dat die 3D FBE in staat is om die gedrag van die struktuur vas te stel waar die Bernoulli-Euler aannames hou, en dat dit tipies goeie korrelasie toon tussen die FBE en buiging voorsien in die literatuur. Die tweede gevallestudie wat ondersoek was, het getoon dat kontinuïteit in ag geneem moet word wanneer die vloeilyn-patroon en die las verspreiding na die ondersteunings balk bepaal word. Die derde gevallestudie het die beperkings van die FBE analise beklemtoon wanneer die primêre ondersteunings balke hul sterkte verloor en die las deur die Membraanwerking gedra word.

Laastens is die FBE en SPM ontwerp metodologie toegepas op 'n tien verdieping kantoor gebou wat as 'n bewys van konsep dien vir die algehele ontwerp metodologie. Die resultate van die FBE analise het die gedrag van die skelet struktuur gedemonstreer en die impak wat die res van die struktuur het op die ondersteunings balke. Die lasdraende kapasiteit van die blad paneel word bereken met die opgedateerde rand buiging wat bepaal is met die FBE analise. Dit word beklemtoon hoe die SPM voorspelling opgedateer kan word gebaseer op verbeterde inligting met verband met die omtrekkende ondersteunings balke buiging.

Acknowledgements

I would like to thank the following people for the significant contributions made towards this work:

- My supervisor, Prof Richard Walls, for all your input and guidance during the research and your patience, quick and thorough response and feedback.
- The ISI scholarship, for funding the research and providing the opportunity
- To Prof Charles Clifton for the discussion, input and feedback regarding the Slab Panel Method.
- My parents and my siblings for supporting me and your interest. My parents for all the sacrifices you have made up to this point that made my studies and my research possible. My brother and sister for your company and always listening to all my explanations of what I am busy with.
- To my friends for walking this path with me, your support and all the discussions.

Table of contents

Declaration	ii
Abstract	iii
Opsomming	iv
Acknowledgements	v
Table of contents	vi
List of figures	xi
List of tables	xiv
List of abbreviations	xv
List of symbols	xvi
1 Introduction	1
1.1 Background to the study	1
1.2 Problem statement	1
1.3 Research objectives	3
1.4 Scope and limitations of this research	3
1.5 Proposed design methodology	4
1.6 Layout of the thesis	6
2 Literature review	9
2.1 Introduction	9
2.2 Structural fire design	9
2.2.1 Prescriptive and performance based design	9
2.2.2 Behaviour of real compartment fires	10
2.2.3 Fire models	11
2.2.4 Fire Resistance Rating (FRR)	13
2.2.5 Protection of a structure	13
2.3 Material models	14
2.3.1 Steel	14
2.3.2 Concrete	17
2.4 Composite structures in fire	21

2.4.1	Behaviour of a structure in fire compared to ambient temperature	21
2.4.2	Behaviour of a composite slab in a fire	21
2.4.3	Collapse mechanisms of a slab panel	23
2.4.4	Tensile Membrane Action (TMA).....	23
2.5	Analysis of structures in fire.....	24
2.5.1	Coupled and decoupled analysis.....	24
2.5.2	“Consistent level of crudeness” of an analysis	25
2.5.3	Available software for the analysis of composite structures in fire.....	26
2.6	Conclusion.....	28
3	Development of the Fire Beam Element for the analysis of three-dimensional skeletal structures	29
3.1	Introduction	29
3.2	Previous development and implementation of the FBE	29
3.3	Fundamental theory of the Fire Beam Element.....	30
3.3.1	Fibre section	30
3.3.2	Loading on the Fire Beam Element	31
3.3.3	Axial strains in a fire	33
3.3.4	Calculation of the total strain.....	33
3.4	Method for updating of the Neutral Axis and the stiffness of a section	36
3.4.1	Input required to calculate the neutral axis and section stiffness	36
3.4.2	Initial phase	37
3.4.3	Iterative phase.....	38
3.5	Finite element matrices for a Fire Beam Element in a 3D frame model	38
3.5.1	Finite element matrices for a Euler-Bernoulli beam element	39
3.5.2	Derivation of the modified stiffness matrix.....	41
3.6	Applying the Fire Beam Element into the design methodology.....	44
3.7	Conclusion.....	46
4	Implementation of a three-dimensional FBE into OpenSees.....	47
4.1	Introduction	47
4.2	Finite element software: OpenSees	47

4.2.1	Background of OpenSees	47
4.2.2	Previous implementation of the FBE in OpenSees.....	47
4.3	Thermo-mechanical analysis in OpenSees	48
4.3.1	Predictor phase	50
4.3.2	Corrector phase.....	50
4.4	Classes developed in OpenSees for implementing the FBE.....	50
4.4.1	FireFiberSectionGJ	51
4.4.2	FireEl3d	54
4.4.3	FireEl3dUni	59
4.5	The TCL commands in order to call the FBE classes in OpenSees	59
4.6	Conclusion.....	61
5	Interaction between the FBE analysis and Slab Panel Method	62
5.1	Introduction	62
5.2	Slab Panel Method.....	62
5.2.1	Effect of edge support beams deflection on the load capacity of the slab panel	63
5.2.2	Design procedures of the Slab Panel Method.....	64
5.2.3	Design guidance for design of the support beams of the slab panel.....	66
5.3	Interaction between the SPM and FBE analysis.....	67
5.3.1	Load transfer from the slab to the supporting beams.....	67
5.3.2	Updating of the deflection of the edge support of the slab panel	68
5.4	Conclusion.....	69
6	Validation	70
6.1	Introduction	70
6.2	Case Study 1: Composite slab with four columns	71
6.2.1	Model details and modelling considerations	71
6.2.2	Results and discussion	74
6.3	Case Study 2: Munich Second Test.....	76
6.3.1	Test setup and modelling considerations.....	76
6.3.2	Results and discussion	81

6.4	Case 3: Cardington Corner Compartment Test	82
6.4.1	Test setup and modelling consideration	83
6.4.2	Results and discussion	88
6.5	Conclusion	90
7	Application of the FBE and SPM design methodology to an office building	92
7.1	Introduction	92
7.2	Building details	92
7.2.1	Composite slab	94
7.2.2	Steel beams and columns	95
7.2.3	Loading of the structure	96
7.3	Design of the compartment	97
7.4	Results and comparison of the design methodology	99
7.4.1	Analysis of skeletal structure	100
7.4.2	Calculation of load-carrying capacity of the slab panel	103
7.5	Conclusion	105
8	Conclusion	106
8.1	Overview	106
8.2	Consideration of objectives	107
8.3	Summary of findings	107
8.3.1	Interaction between the FBE analysis and SPM	107
8.3.2	Validation of FBE analysis	107
8.3.3	Application of the FBE and SPM design methodology	108
8.4	Future work	108
8.5	Closing remarks	109
9	References	110
	Appendix A – Functions developed for the FireFiberSectionGJ and FireEl3d classes in OpenSees	115
A.1	Functions developed for <i>FireFiberSectionGJ</i> -class	115
A.1.1	calculateC-function	115
A.2	Functions developed for <i>FireEl3d</i> -class	117

A.2.1	addLoad-function.....	117
A.2.2	update-function.....	119
A.2.3	getTangentStiff-function	120
Appendix B – SPM software input details for the design example of the ten-storey office building		122
Appendix C – One-dimensional heat transfer of concrete slabs.....		124
C.1	Second Munich Test	124
C.2	Cardington Corner Test (Test 3).....	125
C.3	Design Example: Ten-storey office building.....	126

List of figures

1.1	Available design tools ranging from simplified calculation models to advanced and complex calculation models (Walls, 2016).....	2
1.2	Flowchart illustrating the proposed design methodology to design a full composite concrete-steel structures	5
1.3	Layout of thesis to address the research objectives.....	8
2.1	The behaviour of a typical real fire in a compartment (Walls, 2016)	10
2.2	The temperature-time curves for the ISO 834 curve, Hydrocarbon Curve and External Fire Curve..	11
2.3	The Parametric Fire Curve for a compartment with an opening factor of 0.02, 0.04 and 0.06.....	12
2.4	Reduction factors for the yield strength, proportional limit and stiffness of steel at elevated temperature defined according to EN 1993-1-2 (BSI, 2005)	15
2.5	Stress strain-curve for steel at elevated temperature according to the EN 1993-1-2 (BSI, 2005).....	15
2.6	Relative elongation of steel at elevated temperature according to EN 1993-1-2 (BSI, 2005)	17
2.7	Stress strain-curve for concrete at elevated temperature according to the EN 1992-1-2 (BSI, 2004a)	19
2.8	The inclusion of a descending branch to account for tension stiffening after the concrete have cracked (Deeny, 2010)	19
2.9	Thermal elongation of concrete consisting of (1) Siliceous aggregate and (2) Calcareous aggregate according to EN 1993-1-2 (BSI, 2004a)	20
2.10	The progressive behaviour modes of a slab panel with increasing temperatures during a fire (Bailey and Moore, 2000a)	22
2.11	The different failing mechanism that can occur for a rectangular slab panel when plastic hinges form in the support beams (Abu & Burgess, 2010)	23
2.12	The development of tensile stresses at the centre of the slab panel and a compression ring at the perimeter of the slab panel due to large deformations of the slab panel (Abu, 2008).....	24
2.13	The level of credibility for the combination of fire models with structural model according to Gales et al (2012)	26
2.14	Modelling of composite beam in Vulcan connecting the beam element to the shell elements with a shear connector (Huang, Burgess and Plank, 1999).....	27
2.15	Modelling of a composite beam in OpenSees using shell elements and beam elements (Jiang, Usmani and Li, 2014).....	28

3.1	Example of a cross-section of a 3D beam-element with an eccentric NA from the RA, discretised into fibres	31
3.2	A cross-section subjected to a non-uniform temperature profile with the corresponding thermal strains, equivalent thermal strain (ETS) and resultant thermal strain load (RTSL) and moments (RTSM)	32
3.3	The total strain over a section that are subjected to an axial force and moments about the strong and the weak axis	34
3.4	The mechanical strain that develops in a section in response to a non-linear thermal strain over a section	35
3.5	The stiffness profile, stress profile and stress resultant for a given mechanical strain profile over a cross-section	35
3.6	Flow chart illustrating the iterative method to calculate the neutral axis and section stiffness (adopted from Volkmann (2018))	36
3.7	Three-dimensional beam element with twelve degrees of freedom	39
3.8	Deformed beam between Node 1 and Node 2 at time t with the NA parallel to the RA	42
3.9	The deflection of a node of the beam in the YZ-plane from step t to step $t + \Delta t$, indicating the position of the RA and the NA	42
3.10	Modelled cross-section in the FBE analysis for the support beams accounting for the laterally support provided by the slab panel	45
4.1	A flow diagram illustrating the steps in a thermo-mechanical analysis. The classes required for the thermo-mechanical analysis are shown on the left (adopted from Jiang and Usmani (2013))	49
4.2	Hierarchy of classes implemented in OpenSees for thermo-mechanical analysis (Jiang, 2015) including the classed developed for the FBE methodology	51
4.3	The steps followed to calculate the position of the NA in the calculateC-function (adopted from Volkmann (2018))	53
4.4	The loads (left) and deformation (right) of a beam element in the basic system	54
4.5	The equivalent nodal loads in a basic system representing an UDL, point load or thermal action on the beam element	55
4.6	A flow diagram illustrating the steps taken to update the deformation of the cross-section of the beam	57
4.7	A flow diagram illustrating the step followed in order to calculate the global tangent stiffness matrix of the FBE	58
5.1	Plan view of a composite floor divided into rectangular slab panels (Clifton, 2006)	63
5.2	Distributed loads transferred from the slab panel to the support edge beams	67
5.3	Maximum deflection of the support beams relative to the displacement of their supports	68

6.1	Dimensions of the composite slab with columns at its corners (COST, 2014).....	71
6.2	Temperature profile, as a factor of the ISO 834 temperatures, of the composite support beams.....	73
6.3	Time-temperature curves that would be applied to the steel beams and the concrete slab calculated as a fraction of the Standard Fire Curve (COST, 2014).....	73
6.4	Yieldline pattern of the simply supported slab panel determined with the SPM	74
6.5	Deflection against time for the edge beams and columns, comparing the results of the FBE against Vulcan results (COST, 2014)	75
6.6	Eccentricity of the Neutral Axis relative to the Reference Axis over time for the edge beam in the y-direction	75
6.7	The Second Munich Test layout and the details of the composite slab and edge (Walls, 2016)	77
6.8	Mean gas temperatures and temperatures of the steel beam for the second Munich test (Mensing et al, 2011; Stadler, 2012).....	79
6.9	Time-temperature curves at different depths of the concrete from the soffit determined with a one-dimensional heat transfer analysis.....	79
6.10	Yieldline pattern calculated according to the SPM vs the yieldline pattern assuming continuity at ambient temperature.....	80
6.11	Vertical deflection predicted with the FBE analysis compared to the measured displacements and previous analyses of the Second Munich Test (Adopted from Walls (2016))	81
6.12	Comparison of the displacement at mid-span of the intermediate beam predicted by FBE analysis to the experiment (Stadler, 2012)	82
6.13	Layout of the Cardington structure. The highlighted area indicated the area of the floor subjected to the fire for Corner Compartment Test (Test 3) (adopted from British Steel plc (1999)).....	83
6.14	The dimensions of the trapezoidal profile of the composite slab (Sanad, 2000).....	84
6.15	Time-temperature curve of the corner compartment subjected to a natural fire	85
6.16	Time-temperature curve of the bottom flange, web and top flange of the unprotected steel beam on Gridline 2	86
6.17	Temperature profile of the concrete slab with an equivalent thickness of 102.8 mm at 80 min.....	86
6.18	Loads applied to the adjacent slab panels that are not subjected to the fire.....	87
6.19	The predicted displacement of the support beam at Gridline E by the FBE Analysis compared to the measured displacement and previous analyses of the Cardington Corner Test.....	88
6.20	The predicted displacement of the support beam at Gridline 1 by the FBE Analysis compared to the measured displacement of the Cardington Corner Test.....	90

7.1	Layout of the structure indicating the columns and secondary beam sections (Fischer et al, 2019)...	93
7.2	Typical layout of the floor indicating the compartment to which the design methodology will be applied (Fischer et al, 2019).....	94
7.3	Dimensions of the composite slab with a trapezoidal deck profile	95
7.4	Time-temperature curve of the W12 × 58 columns, W18 × 35 beams and W12 × 19 beams subjected to the Standard Fire Curve	95
7.5	Temperature profile of the concrete slab with an equivalent thickness of 107.5 mm at 60 min.....	96
7.6	Layout of the substructure that were modelled in the FBE Analysis	98
7.7	Yieldline pattern of the slab panel determined with the SPM.....	99
7.8	Vertical deflection at the midspan of the interior support beams during the fire.....	100
7.9	Axial forces (Compression) within the supporting beams induced by the thermal expansion	101
7.10	Lateral deflection of column about its weak and it strong axis.....	102
7.11	The bending moment about the weak and the strong axis within the corner column due to expansion of the support beams	103
B.1	Input details of the slab panel for the ten-storey building for the SPM software.....	123

List of tables

2.1	Reduction factors for normal weight concrete with Siliceous and Calcareous aggregates according to EN 1992-1-2 (BSI, 2004a).....	18
7.1	Dead loads applied to the slab panel	96
7.2	Summary of the results obtained in each iteration of the design method starting with an edge deflection approximated as Span/75. The successive deflections are based upon the FBE analysis results.	104
7.3	Comparison between different cases where the edge deflection are ignored, approximated as span/75 or determined with the FBE Analysis.....	104
C.1	Temperatures within the concrete slab determined with heat transfer calculations for the Second Munich Test	124
C.2	Temperatures within the concrete slab determined with heat transfer calculations for the Cardington Corner Test (Test 3).	125
C.3	Temperatures within the concrete slab determined with heat transfer calculations for the design example of the ten-storey building.....	126

List of abbreviations

ASFP	Association for Specialist Fire Protection
BRE	Building Research Establishment
BS	British Standard
BSI	British Standard Institute
CFD	Computational Fluid Dynamics
COST	European Cooperation in the field of Scientific and Technical Research
DOF	Degree of Freedom
EN	Europe Norm (Eurocode document)
ETS	Equivalent Thermal Stress
FBE	Fire Beam Element
FEA	Finite Element Analysis
FEM	Finite Element Method
FRR	Fire Resisting Rating
HERA	Heavy Engineering Research Association
ISO	International Standards Organisation
NA	Neutral Axes
RA	Reference Axes
RTSL	Resultant Thermal Strain Load
RTSM	Resultant Thermal Strain Moment
SABS	South African Bureau of Standards
SANS	South African National Standard
SCI	Steel Construction Institute
SPM	Slab Panel Method
TCL	Tool Command Language
TS	Tension Stiffening
TMA	Tensile Membrane Action
UDL	Uniform Distributed Load

List of symbols

Roman

a	Parameter 1 for calculation of EN 1993-1-2 stress-strain curve of steelwork
A	Cross-sectional area
b	Parameter 2 for calculation of EN 1993-1-2 stress-strain curve of steelwork
b_{ref}	Reference thermal inertia used in the Parametric Fire Curve
c	Parameter 3 for calculation of EN 1993-1-2 stress-strain curve of steelwork
c	Eccentricity of Neutral Axis from the Reference Axis
E	Young's modulus
EA	Axial stiffness
EI	Bending stiffness
$f_{c,\theta}$	Ultimate stress of the concrete at temperature θ
f_{ck}	Characteristic cylindric compression strength of concrete
f_{ctm}	Mean axial tensile strength of concrete
f_p	Proportional limit of steelwork
f_y	Yield stress of steelwork
$\{F\}$	Load vector
$\{F_\sigma\}$	Stress resultant
$\{F_\theta\}$	Thermal load vector
$\{f\}$	Local load vector
GJ	Torsional stiffness
h_{rc}	Height of rip of a ribbed slab
I	Second moment of inertia
I_{yz}	Product moment of inertia about the weak axis
$k_{*,\theta}$	Reduction factor of material property at temperature θ
$[k]$	Local stiffness matrix
$[K]$	Global stiffness matrix
L	Length
L_{*b}	Maximum span of support beam in *-direction of slab panel
m	Positive moment capacity per unit length
m'	Negative moment capacity per unit length
M	Bending moment
$M_{*,\theta}$	Resultant Thermal Strain Moment (RTSM)
n	Number of fibres
N	Axial load

N_θ	Resultant Thermal Strain Load (RTSL)
O	Opening factor
O_{ref}	Reference opening factor of compartment used in the Parametric Fire Curve
P	Applied point load
P	Axial force within beam-element
$\{q\}$	Load vector in basic reference frame
$\{q_0\}$	Element load vector in basic reference frame
$\{q_\theta\}$	Thermal load vector in basic reference frame
$[Q_{AB}]$	Matrix relating initial nodal coordinate to updated coordinate system
$[Q_b]$	Matrix relating initial nodal coordinate to updated coordinate system in basic reference frame
t	Time
t_0	Total thickness of a slab
T	Temperature
T	Torsion
$\{u\}$	Local deformation vector
$\{U\}$	Global displacement vector
w_u	Ultimate load-carrying capacity of slab panel
w_{yl}	Yield line load-carrying capacity of slab panel
$[W_{AB}]$	Transpose matrix relating forces in updated to initial coordinate system
y	Distance from reference axes along y-axis
z	Distance from reference axis along z-axis

Greek

Δ	Deflection
$\Delta_{*,spsb}$	Maximum deflection of support beams
Δu	Axial deformation of a beam element
$\Delta \theta$	Torsional deformation of a beam element
ε	Strain
ε_{c1}	Strain of concrete at maximum stress
ε_θ	Thermal strain
ε_t	Limiting strain for yield strength
θ	Rotation
θ_g	Gas Temperature [$^{\circ}C$]
σ	Stress

Subscripts

12	Element at reference axis between Node 1 and Node 2
<i>a</i>	Steelwork
<i>AB</i>	Element at neutral axis between Node A and Node B
<i>b</i>	Basic reference frame
<i>el</i>	Elastic
<i>g</i>	Geometric
<i>lim</i>	Limiting
<i>m</i>	Mechanical applied
<i>max</i>	Maximum
<i>NA</i>	Neutral Axes reference frame
<i>p</i>	Proportional
<i>RA</i>	Reference Axes reference frame
<i>reol1</i>	First layer of reinforcement mesh within slab
<i>spsb</i>	Slab panel supporting beam
<i>S</i>	Secant
<i>T</i>	Tangent
<i>T</i>	Total
<i>u</i>	Ultimate
<i>x</i>	x-direction of slab panel (between primary beam supports)
<i>y</i>	y-direction of slab panel (between secondary beam supports)
<i>y</i>	Yield
<i>y</i>	Weak-axis of steel beam
<i>z</i>	Strong axis of steel beam
σ	Mechanical stress
θ	Temperature

1 Introduction

1.1 Background to the study

The Broadgate fire occurred in 1990 in a 14-storey composite steel structure, which was still under construction (SCI, 1991). A fully developed fire occurred at the ground floor while no passive protection had been applied to the steel beams yet. This caused the individual steel beams to fail, causing large deflections to occur in the slab. However, despite the failure of the individual steel beams, no collapse occurred. The Broadgate fire led to the Cardington full-scale tests in 1994 by the Building Research Establishment (British Steel plc., 1999) in which several tests were performed on a 8-storey office building. Only the perimeter beams and the columns were protected, while all the interior beams were left unprotected. In the fire tests conducted, extensive deformations of the slabs were observed during fire tests, but no structural collapse occurred, highlighting the need to better define structural resistance and failure. The Cardington tests confirmed that the structure had significantly higher resistance than what was predicted based on the isolated members. This highlights the importance that a structure in fire should be designed and analysed as a whole, and not as isolated members.

1.2 Problem statement

In recent years, performance-based fire engineering design has become more popular as it can reduce the cost of a structure, as well as provide safer designs. However, the design tools that are generally available for performance-based design are expensive to use and require significant expertise, and are typically only justified in the design of complex structures. Therefore, the need for simpler design tools, which are able to capture the behaviour of a structural system with suitable accuracy has risen. Various design methods currently available are presented in Figure 1.1 on a scale ranging from simple prescriptive design tables to complex general finite element software analyses, placing the research conducted in this thesis in context.

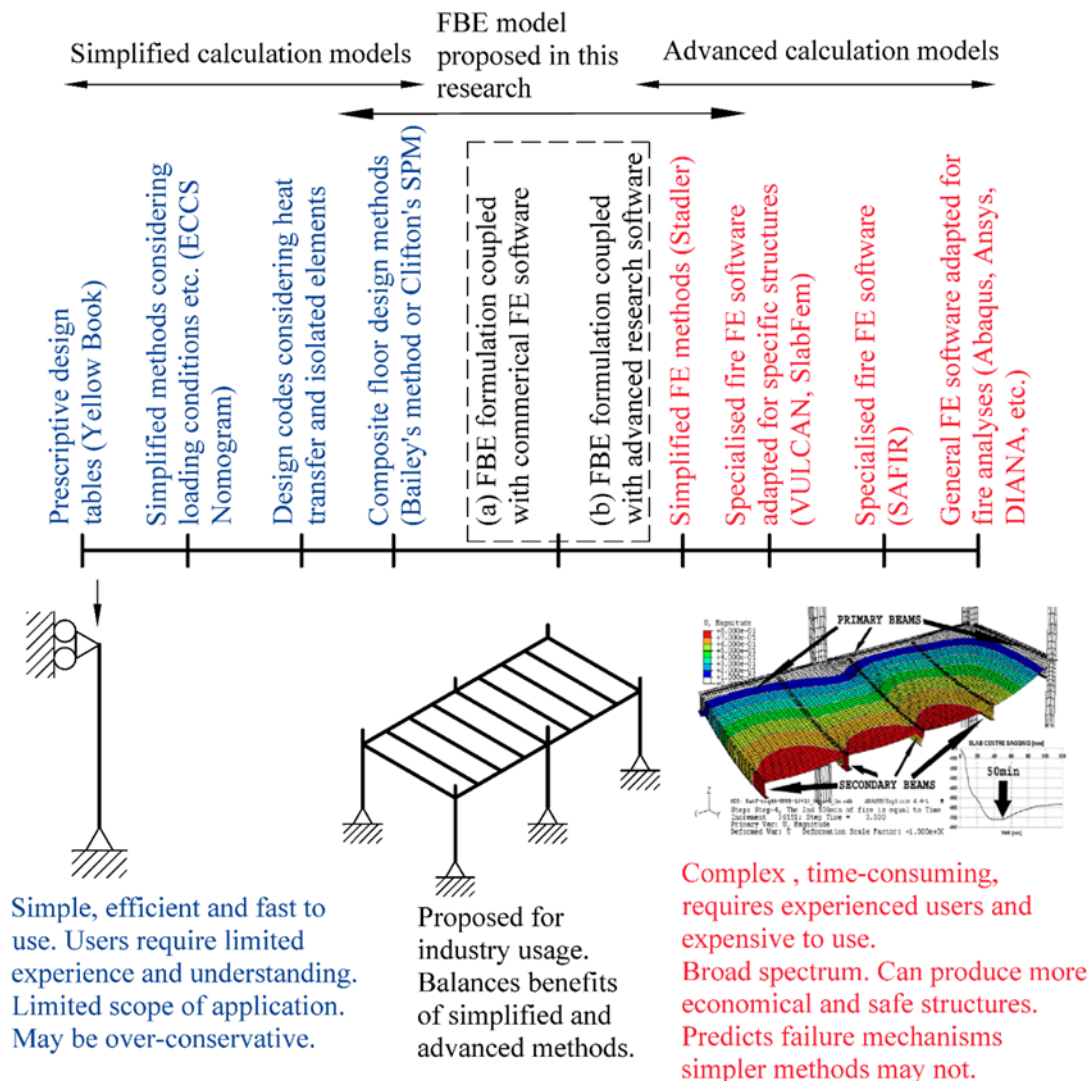


Figure 1.1: Available design tools ranging from simplified calculation models to advanced and complex calculation models (Walls, 2016)

The Fire Beam Element (FBE) methodology was developed by Walls et al (2016; 2018, 2019a, 2019b) with the goal of providing a simplified analysis tool that is still sufficiently accurate for quantifying important structural phenomena. The FBE methodology uses beam elements, which are able to consider nonlinear structural and thermal behaviour, and can also consider the global behaviour of a structure. The original work was extended by Volkmann et al (2018; 2020) to be included within OpenSees, enable to the design system to be applied to structures more easily and efficiently. However, up until this stage the methodology has not directly considered composite floor systems, and only two-dimensional (2D) analyses have been conducted, meaning that global structural interactions have not been investigated. In order to consider all structural components it was recommended in the original FBE work to combine the FBE methodology with a tensile membrane model, such as the Bailey-BRE method (Bailey and Moore, 2000a, 2000b), the Slab Panel Method (Clifton, 2006) or the analytical approach developed by Burgess and Chan (2020), and this work seeks to address this topic.

The Slab Panel Method (SPM) is based on the Bailey-BRE method and is used to design composite floors in fire. Both aforementioned design methods divide a continuous composite slab into rectangular slab panels and design each slab panel in isolation. Each slab panel is designed as a unit consisting of protected edge beams and unprotected interior beams. The SPM guidelines and methodology provide details regarding the reinforcement needed for slab panels and additional checks for shear adequacy, integrity and compression crushing of the concrete. Such checks and information help guard against localised failure, rebar rupture, integrity requirements and similar issues that global structural models are often not able to identify.

1.3 Research objectives

The aim of this research is to develop a simplistic design methodology that can be used to analyse and design a full three-dimensional (3D) structure that is subjected to a compartment fire. This design methodology will focus on composite steel structures (although is applicable to other construction systems) and is based upon the FBE methodology to analyse the skeletal frames whilst using the SPM to design floors. Therefore, the approach of this design methodology will be similar to an ambient design where a slab panel and the structure supporting the slab panel will be considered as separate systems. In order to achieve this goal, the objectives of the work are as follows:

- To develop the FBE methodology for a 3D element, in order to apply the FBE to 3D skeletal structures. In previous work the FBE formulation has only been implemented for 2D structures. The FBE methodology for the 3D element will be implemented within a finite element software, named OpenSees, which will be used to analyse the 3D frame structures.
- To validate the behaviour of the FBE in a 3D model using experimental and numerical studies. The validations will be used to understand the behaviour of the FBE approach in a 3D model, and to understand and illustrate the limitations of the FBE. It is important to identify limitations to illustrate when models developed should not be applied.
- To enable the FBE analysis to interact with the SPM, where the SPM can be used to update the loads on the supporting structure. In return, the FBE analysis can be used to update the deflections of the support beams that are used in the SPM when calculating the ultimate load of the slab panel. This linking of design methods provides a novel approach to modelling such systems.
- To apply the design methodology to a structure and investigate the effect that the updating of the support deflections have on the predicted ultimate load capacity of the slab panel. This serves as an initial proof of concept, which will require further research.

1.4 Scope and limitations of this research

The analysis of a structure in a fire usually consists of a fire model, a heat transfer model and a structural model (Buchanan and Abu, 2017) of which these models can either be coupled or decoupled. However, as the aim of this research is to develop a simple design method, a decoupled approach is implemented. Furthermore, the

focus of this research is to implement the FBE methodology for a 3D skeletal model to analyse the structural behaviour and to link the analysis system with the SPM.

In this research bending about the strong and the weak axis will be investigated in order to implement the FBE methodology for a 3D model. The effect of torsion on the element is assumed to be negligible as the aim of the research is to implement the FBE methodology for composite beams where the slab provides lateral and torsional stiffness. In the case where the FBE is used for a column, an assumption is made that the effect of torsion will be negligible. This will be true for most symmetric sections such as I-sections or H-sections. For non-symmetric sections where the effect of torsional buckling is not negligible, further research is required to determine the effect of fire on the torsional stiffness of an element.

An underlying assumption of the FBE formulation is the Bernoulli-Euler assumption that plane sections remain plane and that small rotations occur. Therefore, sudden changes in the beam stiffness or cross-sectional properties, which lead to shear deformation, are not explicitly captured by the FBE formulation and in such instances analyses become less accurate.

In the combined FBE/SPM design methodology proposed, the edge support beams are assumed to support the slab panel. Therefore, the FBE analysis will only be accurate as long as the edge beams have sufficient strength to support the slab panel. If the edge beams do not have sufficient strength to support the slab panel, the analysis will predict failure significantly earlier, especially if the entire slab panel becomes a hanging catenary from columns or is supported by the rest of the structure that is not affected by a fire.

The implementation of the FBE methodology in a 3D frame model will be validated with numerical and experimental cases. The material models that are used are based on the Eurocodes. Furthermore, tension stiffening is included in the material model for concrete and is based on the work of Deeny (2010).

1.5 Proposed design methodology

The proposed design methodology to design a composite concrete-steel structure is introduced at this stage to place the remainder of this thesis and the objectives listed above in context. The proposed design methodology consists of considering the composite slab and the supporting skeletal structures as separate systems, which can interact with each other. The composite slab is designed with the SPM and the supporting skeletal structure is analysed with the FBE analysis. The FBE analysis refers to a 3D analysis of a skeletal structure that is performed using the FBE formulation. The SPM is used to determine the loads on the edge support beams in the FBE analysis, while the deflections determined with the FBE analysis will be used to update the edge deflection of the FBE. The linking of the FBE analysis to the SPM is discussed in Chapter 5.

It is important to bear in mind that the purpose of the SPM is to analyse and design a slab panel for a given fire severity and therefore, only predicts the state of the slab panel, including aspects such as the maximum deflections, yieldline patterns and load-carrying capacity, at the given fire severity at the point of failure. The

FBE analysis, conversely, is able to analyse and predict the behaviour of the supporting skeletal structure for the duration of the fire. Therefore, with the FBE and SPM design methodology the behaviour of the supporting skeletal structure is determined according to the ultimate load-carrying capacity and yieldline pattern of the slab panel for the given fire severity. The proposed design methodology is illustrated in Figure 1.2, indicating how the SPM and FBE analysis will interact with each other.

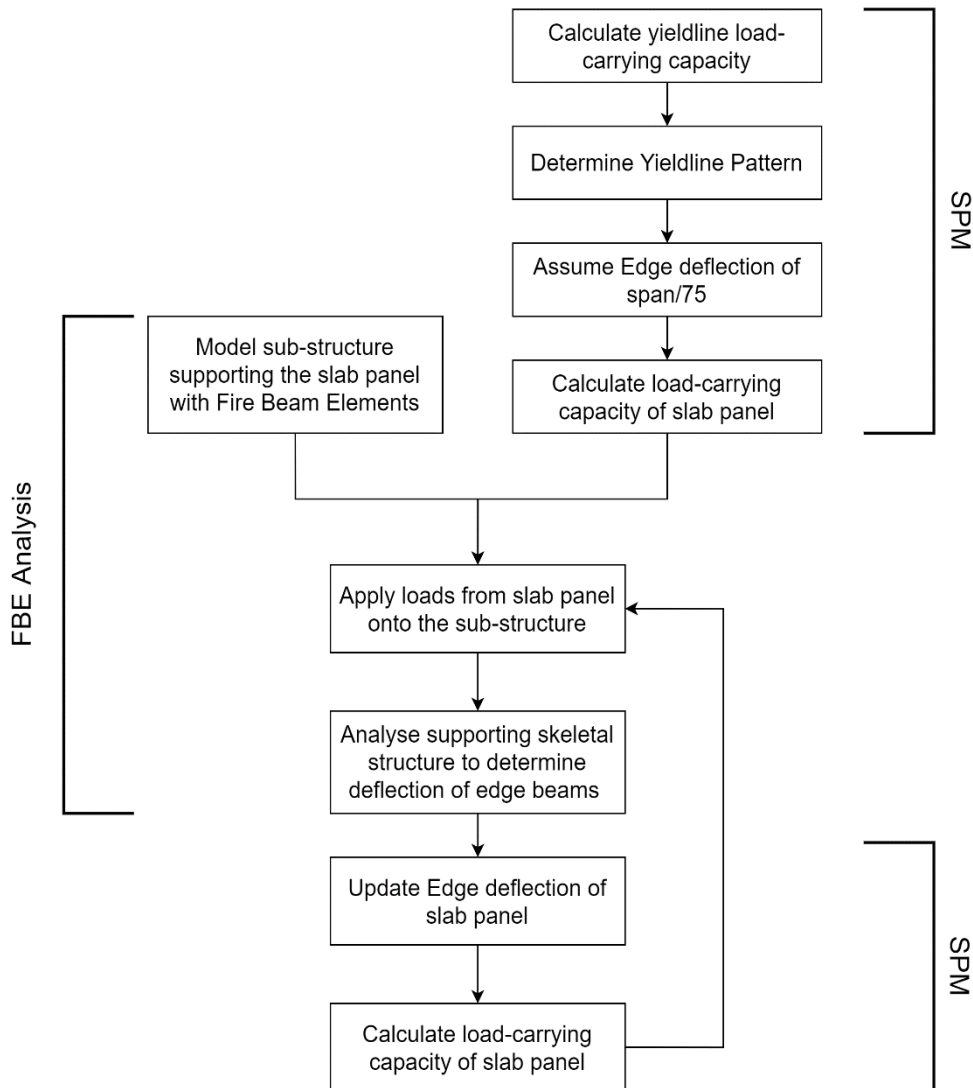


Figure 1.2: Flowchart illustrating the proposed design methodology to design a full composite concrete-steel structures

In the design methodology, the slab panel is first designed with the SPM, assuming an edge deflection of span/75. This can be done with the aid of spreadsheets or with the SPM software. The load-carrying capacity calculated by the SPM defines the failure yieldline pattern, which is used to determine the load pattern on primary beams by defining tributary areas for loading.

Thereafter, the supporting skeletal structure is modelled with the FBE approach in OpenSees. The skeletal structure includes the columns and beams supporting the slab panel, as well as (if needed) at least half the

length of the adjacent beams to create a sub-model from a larger structure. If half of the length of the adjacent beams is modelled, symmetric boundary condition should be applied to the end of the beams. Lateral support should be provided by these boundary conditions. The columns are fixed at the bottom and pinned at the top. Additional to the loads transferred to the edge beam, point loads are applied to the columns to take into account the loads transferred through the columns from storeys above the compartment.

After the analysis is setup, the deformation of the support edge beams can be determined and used in the SPM to calculate the new load-carrying capacity of the slab panel. This load-carrying capacity will then be applied to the structure in order to determine a more accurate deflections of the edge beams, until the load-carrying capacity converges. Convergence is typically achieved within a small number of iterations.

1.6 Layout of the thesis

Chapter 2 will provide an outline on the literature regarding structural fire design, fire models, material models of steel and concrete, the behaviour of composite structures, and the tools available to perform elevated temperature structural analyses.

In Chapter 3, the development and the fundamental theory of the FBE formulation for 3D analyses will be discussed. A brief overview on the previous development and implementation of the FBE formulation will be given. The fundamental theory of the FBE in terms of a 3D element will be discussed and important concepts, such as an eccentric Neutral Axes (NA) a distance from the Reference Axes (RA), Resultant Thermal Strain Load (RTSL) and Moments (RTSM) will be introduced. Thereafter the integration of the 3D FBE into the FE theory will be discussed.

In Chapter 4, the implementation of the FBE methodology for a 3D element in a finite element software, namely OpenSees, will be discussed. A brief overview will be given of the thermo-mechanical analysis being used in OpenSees, highlighting where the FBE methodology will be incorporated in the analysis. Thereafter, the classes developed for a 3D FBE and the TCL script (the format for inputting files into OpenSees) by which the classes are called are discussed.

In Chapter 5, the focus will shift to the SPM and the interaction between the SPM and the FBE Analysis. An overview will be given on the development of the SPM and the design procedures of the SPM. Thereafter, the interaction between the SPM and the FBE Analysis will be addressed, focussing on (a) the transfer of the load from the slab panel and (b) the updating of the edge support deflection of the slab panel which influences predicted capacities.

In Chapter 6, the FBE analysis model developed in OpenSees will be validated with three case studies. The interaction of the SPM with the FBE analysis will not be validated directly, as the SPM design methodology provides the load-carrying capacity for the slab panel, while the case studies focus on validating the behaviour of the structure, with a specific emphasis on deformations. However, the SPM is still required to determine the

yieldline pattern of the slab panels in order to determine the loads on the support beams. The case studies vary in complexity, from a simple numerical benchmark study to a full scale test of a real composite structure.

Chapter 7 will provide an example application of the design methodology to a compartment fire which is part of a large 10-storey office building. In the example, the analysis of the skeletal support structure will be discussed, as well as the SPM and the interaction between the SPM and the FBE analysis.

Lastly, Chapter 8 will conclude with a summary of the findings in the research and recommendations for future development in the field. A basic roadmap is given in Figure 1.3 by which the objectives of the research will be addressed.

The annexes of this work provide information such as input files for models developed, scripts for subroutines in OpenSees to implement the FBE and results of calculations. The classes developed for the FBE and the input files for the FBE analysis is provided in an online repository (Strauss and Walls, 2021).

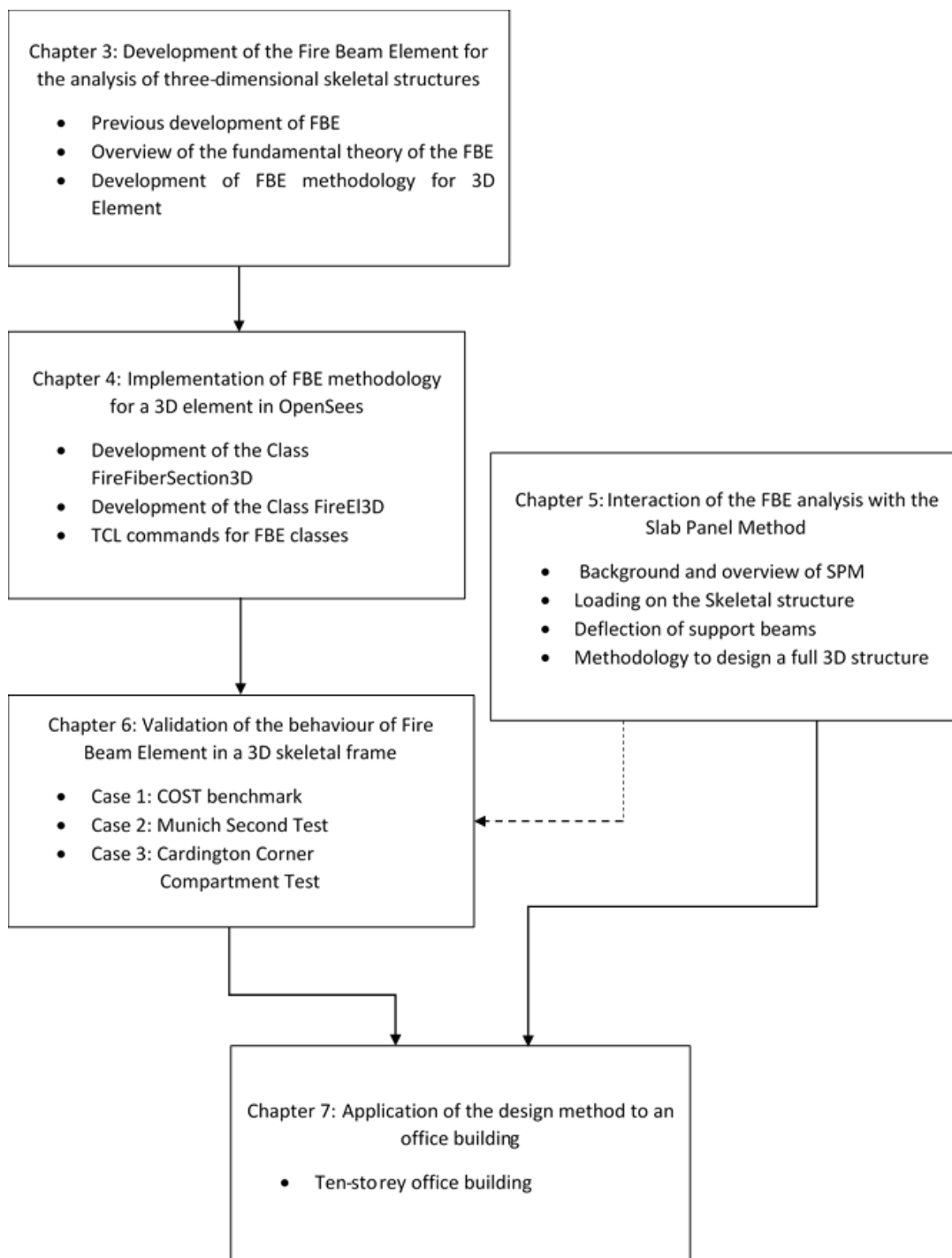


Figure 1.3: Layout of thesis to address the research objectives

2 Literature review

2.1 Introduction

In this chapter an overview will be given of the literature regarding structural fire design, especially with respect to composite structures. Important topics regarding structural fire design will be discussed. This includes topics such as prescriptive and performance based design, the behaviour of compartment fires and fire models and the protection of structures. The material models for concrete and steel are discussed as provided by EN 1992-1-2 (BSI, 2004a) and EN 1993-1-2 (BSI, 2005). Thereafter, composite structure in fire are discussed in which the behaviour of structures in fire is compared to ambient conditions and the behaviour of composite slabs in fire. Lastly, the analysis of a structure is discussed in terms of analysis considerations such coupled and decoupled analysis, crudeness of the models and available software with which structures can be analysed in a fire.

2.2 Structural fire design

2.2.1 *Prescriptive and performance based design*

Prescriptive based design refers to design methods that are based on prescribed specifications for a structure that will ensure a certain minimum level of safety for the structure (Buchanan and Abu, 2017). For example, prescriptive based requirements would usually stipulate the maximum temperature of a structural element to ensure the structure would not fail. Prescriptive based design approaches often involve the use of design tables or simple design calculations of isolated elements. An example of a prescriptive base design method is the use of the Yellow Book (ASFP, 2007) to determine the required protection for a steel member to obtain a specified fire resistance rating.

Prescriptive design usually results in a less economical design, as it requires that every member in the structure needs to be protected. Furthermore, the behaviour of a structural member depends on its constraints and may behave differently depending on the surrounding structure. Thus, the level of safety of a structure cannot always be assured by using a prescriptive based design.

Performance-based design methods, in contrast, give freedom to the designer to achieve a specified performance and required level of safety. With performance based design, the designer is able to consider the behaviour of the whole structure, instead of each element separately. Consequently, performance-based designs typically yield more economical designs and more complex structures can be considered. In a study Khorasani et al (2019) concluded that the amount of beams that required protection according to a prescriptive design could be reduced by 40%-50% when a performance-based design was used. Furthermore, according to Guo et al (2013), the understanding of the behaviour of structures enables that the reliability of structures can be determined. Therefore, a sufficient level of safety of a structure can be assured.

However, performance-based design requires that the designer has a deeper understanding of the behaviour of fire and of the structure in fire. Furthermore, performance-based design requires more time and computational effort to perform an analysis of a whole structure, especially for complex structures.

2.2.2 Behaviour of real compartment fires

The behaviour of real compartment fires are complex due to numerous factors that can influence the behaviour. Factors that influence the behaviour include the geometry and size of the compartment, the amount of openings and their positioning, the amount of fuel in the compartment, the presence of active fire protection and the type of material used in the compartment. Some of these factors may completely change the nature of the fire, for example in a large and open warehouse a localized fire may occur or if active fire protection is present, the fire may not become fully developed.

Figure 2.1 illustrates the development of a typical fully developed compartment fire. After a fire has ignited, a fully developed compartment fire consists of three phases: the growth/smouldering phase, the fully-developed phase and a decay phase. Some authors list flashover as an independent phase as well, rather than being a point in time. During the growth phase, the fire is still localised, until sufficient heat has built up so that all the combustibles in the compartment ignite spontaneously and the whole compartment is engulfed in flames. This point is known as flashover and is characterised by a rapid increase in the compartment temperatures. Flashover marks the transition from the growth phase to the fully-developed phase. The fully-developed phase is characterised by a more steady burning rate and temperature due to ventilation control. The fully-developed phase normally reaches temperatures around 800-1200 °C and can last around 30 minutes (Lennon and Moore, 2003), depending on the fuel and the ventilation conditions of the compartment. As the fuel in the compartment is exhausted, the fire enters the decay phase, where the temperature of the compartment eventually decreases to ambient temperatures.

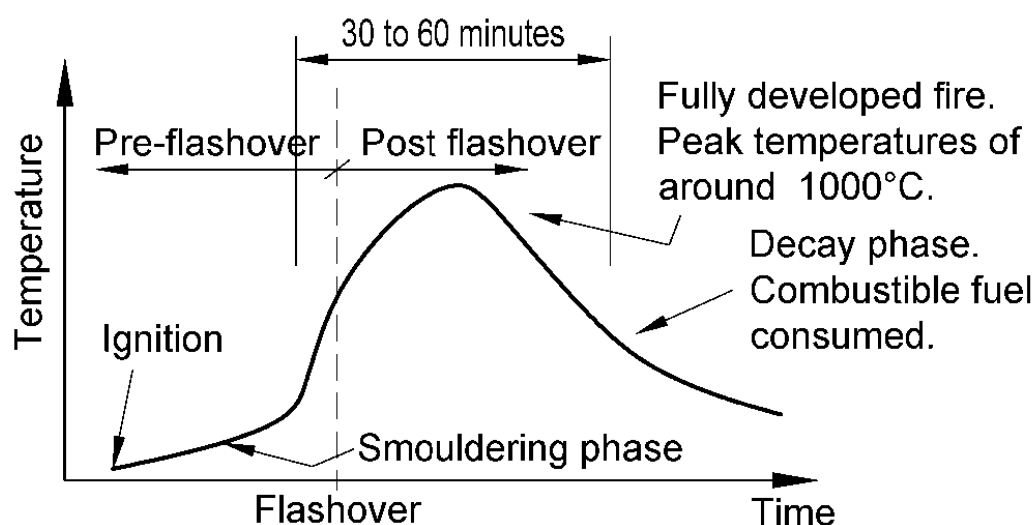


Figure 2.1: The behaviour of a typical real fire in a compartment (Walls, 2016)

2.2.3 Fire models

Different models exist to estimate the temperatures within a compartment during a fire. These models range from simplistic temperature-time curves to complex computer field models.

Nominal temperature-time curves

The most common nominal temperature-time curve is the ISO 834 curve (ISO, 1999), which is also known as the Standard Fire Curve. The Standard Fire Curve is used in furnace tests to test the Fire Resistance Rating (FRR) of structural members and fire stopping systems.

The Standard Fire Curve is not a good representation of the behaviour of a real fire, as it is not dependent on the properties of the compartment, for example the ventilation. The Standard Fire Curve also does not include a cooling phase, in which a structure could also fail. However, the Standard Fire Curve provides a useful benchmark and is commonly being utilised in the design of structures.

Additional nominal temperature-time curves that are defined by the Eurocode (BSI, 2002c) include the Hydrocarbon Fire Curve, which is applicable for petrochemical fires, and the External Fire Curve. Figure 2.2 shows the different nominal temperature-time curve as defined by the Eurocode (BSI, 2002c).

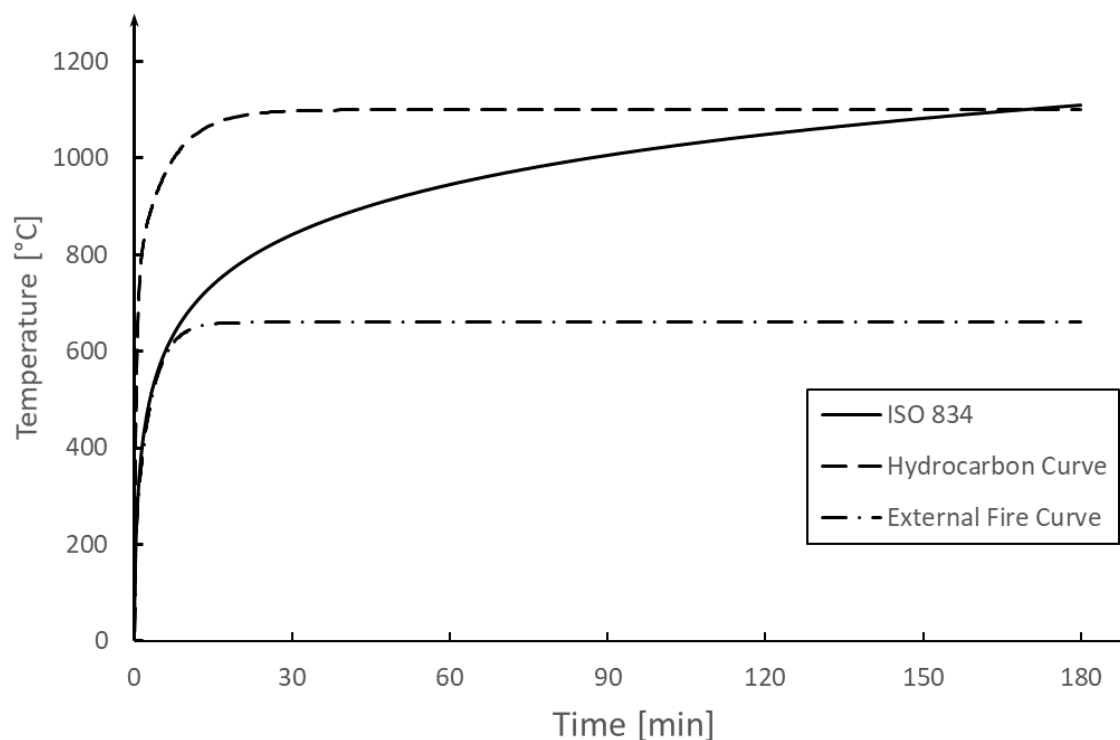


Figure 2.2: The temperature-time curves for the ISO 834 curve, Hydrocarbon Curve and External Fire Curve

For the Standard Fire Curve:

$$\theta_g = 20 + 345 \log(8t + 1) \quad (2.1)$$

where θ_g is the gas temperature, in °C, of the compartment
 t is the time in minutes

For the Hydrocarbon Fire:

$$\theta_g = 20 + 1080 (1 - 0.325e^{-0.167t} - 0.675e^{-2.5t}) \quad (2.2)$$

For the External Fire:

$$\theta_g = 20 + 660 (1 - 0.687e^{-0.32t} - 0.313e^{-3.8t}) \quad (2.3)$$

Parametric Fire Curve

In the Annex A of the Eurocode 1 Part 1.2 (BSI, 2002c) a parametric fire curve is defined. The Parametric Fire Curve is very useful for designing a structure for fire as it takes into account the ventilation, the thermal inertia, and the fuel load density of the compartment. Furthermore, the Parametric Fire Curve includes a cooling phase that approximates the decay phase for the structure linearly. The Parametric Fire Curve is calibrated such that the heat up phase closely follows the Standard Fire Curve for a reference opening factor, $O_{ref} = 0.04 \text{ m}^{1/2}$, and thermal inertia, $b_{ref} = 1160 \text{ J/m}^2\text{s}^{1/2}\text{K}$. The opening factor, O , represent the ventilation of the compartment and area of the compartment and the opening. Figure 2.3 illustrates Parametric Fire Curves with different ventilation condition.

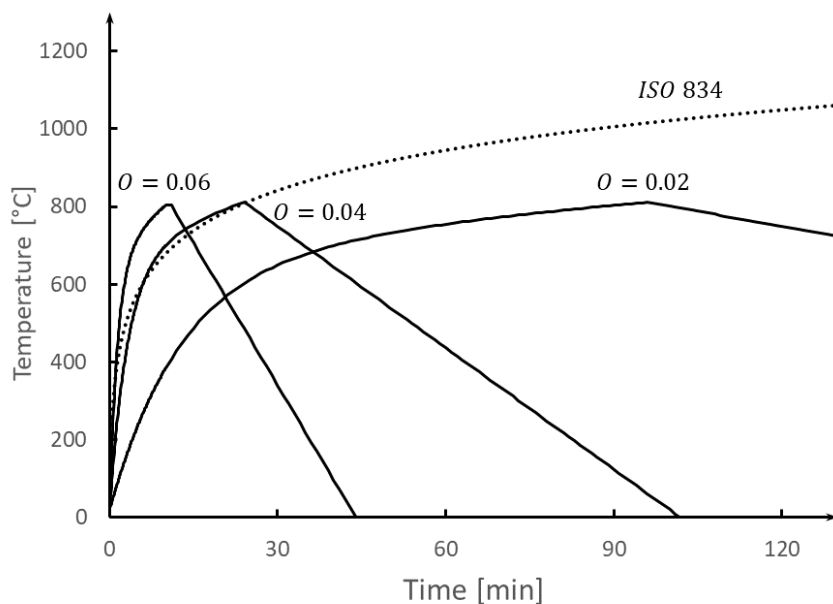


Figure 2.3: The Parametric Fire Curve for a compartment with an opening factor of 0.02, 0.04 and 0.06

From Figure 2.3 it can be seen that a higher opening factor leads to higher temperatures within the compartment, but a shorter duration. Whereas, a lower opening factor leads to lower temperatures within the compartment for a longer duration.

Zone models

Zone models are simple models in which pre-flashover and post-flashover fire can be modelled. Pre-flashover fires are modelled with a two-zone model, whereas a post-flashover fire can be modelled using a one zone model. A zone refers to a homogeneous layer. The zone models are based on the equations for the conservation of mass and energy and are able to calculate height of each zone and heat flux to the lower zone, in the case of a two zone model, the temperature of the floor and wall, as well as of the zone and the flow of smoke and toxic products (Buchanan and Abu, 2017). For input, these models require the heat output of the fire and a more detailed description of the geometry of the compartment, for example the position of the openings in the compartment.

Field models

Field models are the most advanced models in which Computational Fluid Dynamics (CFD) are used to model the behaviour of the compartment fire. Due to the complexity and high computational effort required, CFD models are rarely used in practise and are mostly used for research.

2.2.4 Fire Resistance Rating (FRR)

The FRR of a system is defined as the duration to which a structure can be subjected to a standard fire (ISO 834) before it fails (Law and Bisby, 2020). Three failure criteria are specified for the FRR, which are the Stability (R), Insulation (I) and Integrity (E) resistance. The criteria are defined by the Eurocode (BSI, 2002c) as follows: Structural stability is the ability to resist specified actions during the fire, Insulation resistance is the ability to restrict the temperature rise on the unexposed side of the member and Integrity is the ability to prevent the spread of hot gasses, such as smoke, and flames through the member.

To obtain an FRR, a construction member should satisfy one or more of the failure criteria. For example, a beams and column should only be able to satisfy the stability criteria, whereas doors should satisfy the insulation and integrity criteria and floor systems should satisfy all three of the criteria.

2.2.5 Protection of a structure

The protection of a structure in a fire can be divided into two groups: active fire protection and passive fire protection. Active fire protection requires a mechanism, person or an system to initiate and operate the protection mechanism (Buchanan and Abu, 2017). Active fire protection is usually used to delay or prevent a fire entering the fully developed phase. Therefore, active fire protection is most effective before flashover occurs, when it is still possible that the fire can be easily extinguished. An example of an active fire protection mechanism is a sprinkler system that will be activated by a significant increase in temperature in a compartment.

Passive fire protection is built into the structure and does not require that any action is taken to activate the protection mechanism (Buchanan and Abu, 2017). The goal of passive fire protection is to prevent the spread of the fire to adjacent compartments and to provide protection to the structural element after the fire has reached flashover. Concrete members can be protected by providing sufficient cover to the reinforcement steel, whereas steel members need to be protected by an insulating material. Examples of such materials are intumescent paints, fibre cement boards, gypsum boards or concrete encasement.

2.3 Material models

2.3.1 Steel

Steel is vulnerable to a fire, because steel has a high thermal conductivity, members are typically thin, and therefore they heat up quickly and lose significant strength at elevated temperature. Steel loses about half its strength at ambient temperatures at around 600°C. The Eurocode (BSI, 2005) provides details regarding temperature-stress-strain curves for carbon and stainless steels. However, for this research only carbon steel will be used.

Mechanical properties

At ambient temperature design, steel can be regarded to having perfect elastic-plastic behaviour, with a defined yield strength. However, at elevated temperature, steel has a gradual transition from elastic behaviour until the steel yields. The start of this transition is marked by the proportional limit, which is defined as the stress at which the stress-strain curve becomes non-linear. In the Eurocode, the creep and the transition thermal effects are explicitly incorporated in the stress-strain curve.

The Eurocode calculates the strength and stiffness of steel at elevated temperatures with the use of reduction factors. The Eurocode defines the following reduction factors:

- Effective yield strength: $k_{y,\theta} = \frac{f_{y,\theta}}{f_y}$ (2.4.1)

- Proportional limit: $k_{p,\theta} = \frac{f_{p,\theta}}{f_y}$ (2.4.2)

- Slope of the linear elastic range: $k_{E,\theta} = \frac{E_{a,\theta}}{E_a}$ (2.4.3)

The effective yield strength, $k_{y,\theta}$, and the proportional limit, $k_{p,\theta}$, are defined relative to the yield strength at 20°C and the slope of the linear elastic range is defined relative to the slope at 20°C. Figure 2.4 shows the reduction factors for steel.

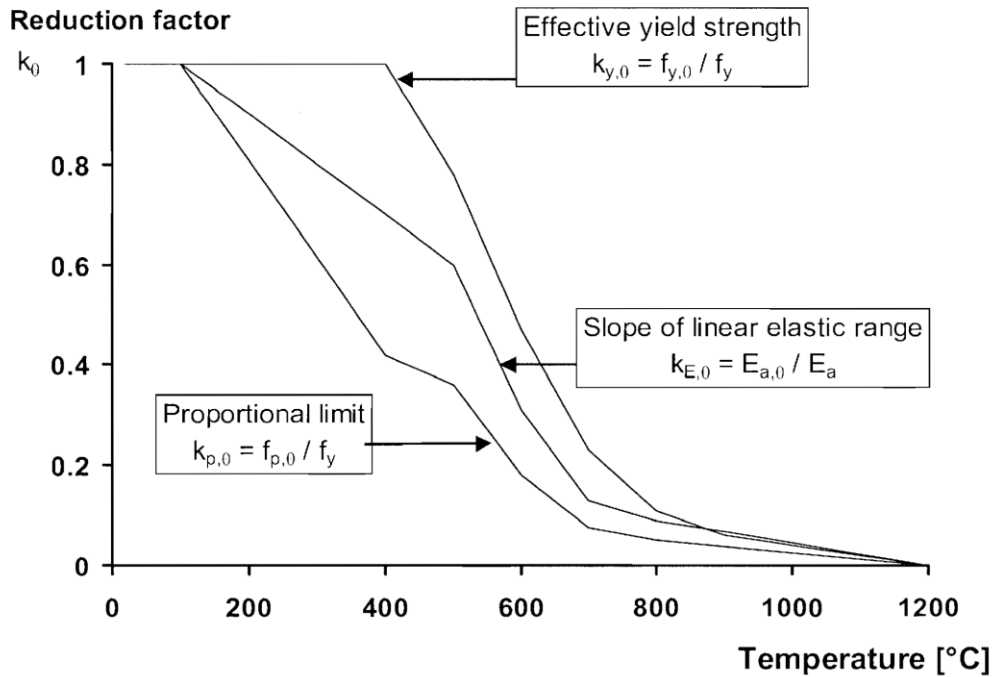


Figure 2.4: Reduction factors for the yield strength, proportional limit and stiffness of steel at elevated temperature defined according to EN 1993-1-2 (BSI, 2005)

Figure 2.5 illustrates the stress-strain curve for steel at elevated temperature. Initially, steel behaves in a linear elastic manner, until the stress reaches the proportional limit. Thereafter, the material enters the transitional phase until the stress reaches the effective yield stress. The stress of the steel then remains at the effective yield stress until the limiting strain for yield strength, $\epsilon_{t,\theta}$, is reached. Lastly, the stress descends linearly to zero stress at the ultimate strain, $\epsilon_{u,\theta}$.

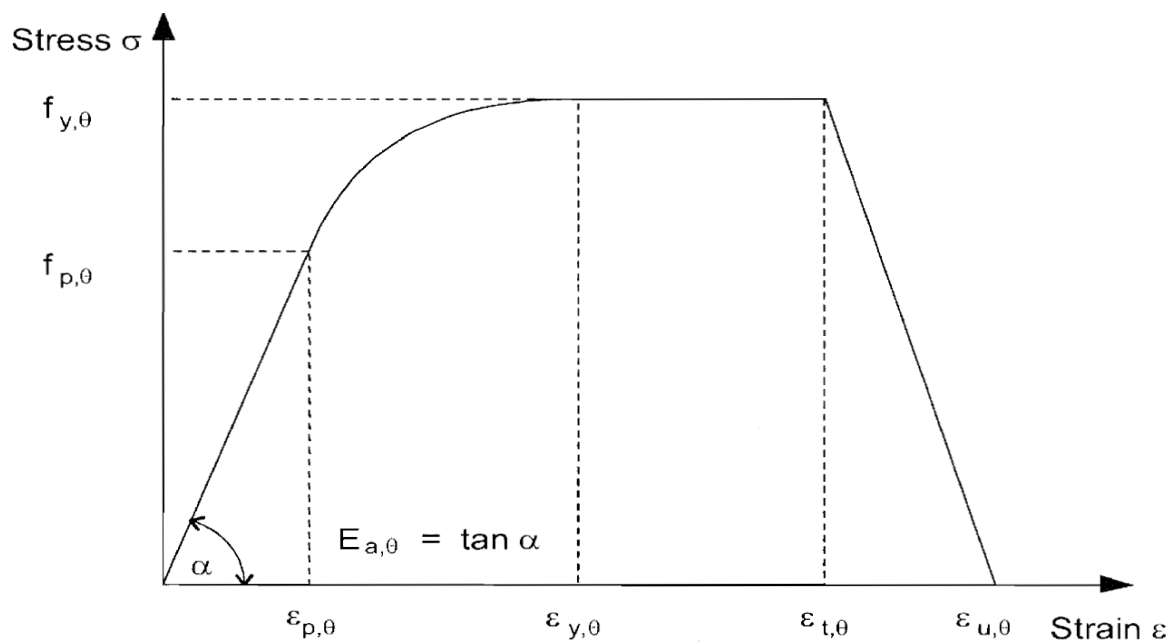


Figure 2.5: Stress strain-curve for steel at elevated temperature according to the EN 1993-1-2 (BSI, 2005)

The temperature-stress-strain curve can be represented by the following equations given in the Eurocode:

$$\sigma = \varepsilon \cdot E_{s,\theta} \quad \text{for} \quad \varepsilon < \varepsilon_{p\theta} \quad (2.5)$$

$$\sigma = f_{p,\theta} - c + \left(\frac{b}{a}\right) \cdot \left[a^2 - (\varepsilon_{y,\theta} - \varepsilon)^2\right]^{0.5} \quad \text{for} \quad \varepsilon_{p\theta} < \varepsilon < \varepsilon_{y,\theta} \quad (2.6)$$

$$\sigma = f_{y,\theta} \quad \text{for} \quad \varepsilon_{y\theta} < \varepsilon < \varepsilon_{t,\theta} \quad (2.7)$$

$$\sigma = f_{y,\theta} \cdot \left[1 - \frac{\varepsilon - \varepsilon_{t,\theta}}{\varepsilon_{u,\theta} - \varepsilon_{t,\theta}}\right] \quad \text{for} \quad \varepsilon_{t\theta} < \varepsilon < \varepsilon_{u,\theta} \quad (2.9)$$

$$\sigma = 0.0 \quad \text{for} \quad \varepsilon = \varepsilon_{u,\theta} \quad (2.9)$$

with the parameters are calculated as follows:

$$\varepsilon_{p,\theta} = \frac{f_{p,\theta}}{E_{a,\theta}} \quad \varepsilon_{y,\theta} = 0.02 \quad \varepsilon_{t,\theta} = 0.15 \quad \varepsilon_{u,\theta} = 0.20$$

and:

$$a^2 = (\varepsilon_{y,\theta} - \varepsilon_{p,\theta}) \cdot \left(\varepsilon_{y,\theta} - \varepsilon_{p,\theta} + \frac{c}{E_{a,\theta}}\right) \quad (2.10)$$

$$b^2 = c \cdot (\varepsilon_{y,\theta} - \varepsilon_{p,\theta}) \cdot E_{a,\theta} + c^2 \quad (2.11)$$

$$c = \frac{(f_{y,\theta} - f_{p,\theta})^2}{(\varepsilon_{y,\theta} - \varepsilon_{p,\theta}) \cdot E_{a,\theta} - 2 \cdot (f_{y,\theta} - f_{p,\theta})} \quad (2.12)$$

Thermal properties

The thermal strain, ε_{th} , is dependent on the temperature of the steel, θ , and can be calculated using the following equations given in Eurocode 1993-1-2:

$$\varepsilon_{\theta} = 1.2 \cdot 10^{-5} \cdot \theta + 0.4 \cdot \theta^{-8} \cdot \theta^2 - 2.416 \cdot 10^{-4} \quad \text{for} \quad 20^\circ\text{C} < \theta < 600^\circ\text{C} \quad (2.13)$$

$$\varepsilon_{\theta} = 1.1 \cdot 10^{-2} \quad \text{for} \quad 600^\circ\text{C} < \theta < 735^\circ\text{C} \quad (2.14)$$

$$\varepsilon_{\theta} = 2 \cdot 10^{-5} \cdot \theta - 6.2 \cdot 10^{-3} \quad \text{for} \quad 735^\circ\text{C} < \theta < 1200^\circ\text{C} \quad (2.15)$$

The thermal strain of steel is illustrated in Figure 2.6. Between 750°C and 860°C , the thermal strain of steel remains constant due to phase change that the steel undergoes.

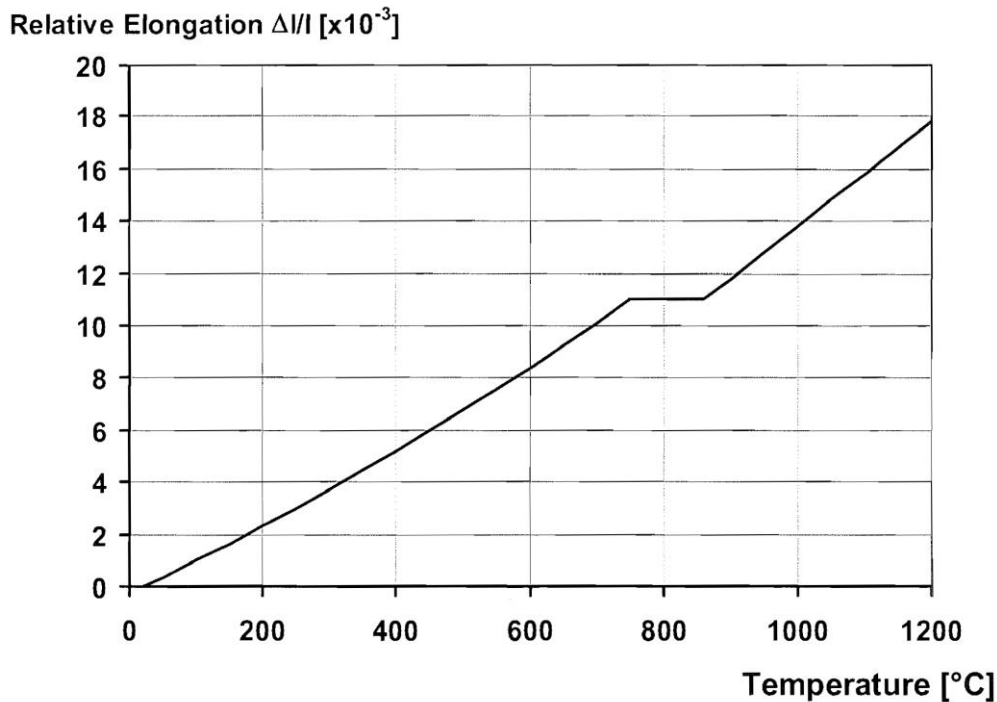


Figure 2.6: Relative elongation of steel at elevated temperature according to EN 1993-1-2 (BSI, 2005)

2.3.2 Concrete

Concrete is known to have a good fire resistance. This is due to the low thermal conductivity of concrete, and when coupled with the larger typical cross-sectional size of members, ensures that concrete elements heat up much more slowly than steel. Furthermore, the evaporation of the water, the dehydration of the CSH and the decomposition of portlandite that occurs at 500°C – 550°C (Mróz, Hager and Korniejeko, 2016) absorbs heat and reduces the increase in the temperatures in the concrete.

However, concrete, especially high-performance concrete, is prone to spalling due to the evaporation of water. The spalling can influence the performance of the structure, expose reinforcement steel directly to the fire and pose a safety risk for occupants. Possible solutions to prevent spalling includes the use of alkali activated binders instead of Portland cement and the use of polypropylene fibres in the concrete (Mróz, Hager and Korniejeko, 2016).

The behaviour of concrete in fire is more complex than that of steel, as concrete consists of a matrix of materials and the properties of concrete is dependent on these materials. Therefore, the Eurocode (BSI, 2004a) provides mechanical and thermal properties for siliceous and calcareous aggregates concrete at elevated temperatures.

Mechanical properties

The stress-strain curve for concrete at an elevated temperatures, provided by Eurocode 1992-1-2, are defined by the following parameters: the compressive strength, $f_{c,\theta}$, of the concrete with the corresponding strain, $\varepsilon_{c1,\theta}$, and the ultimate strain, $\varepsilon_{cu1,\theta}$. The compressive strength of concrete at an elevated temperature is calculated by

multiplying a reduction factor, $f_{c,\theta}/f_{ck}$, by the compressive strength of the concrete at ambient temperature.

The values of the parameters for siliceous and calcareous aggregates are given in Table 2.1.

Table 2.1: Reduction factors for normal weight concrete with Siliceous and Calcareous aggregates according to EN 1992-1-2 (BSI, 2004a)

Concrete temp. θ	Siliceous aggregates			Calcareous aggregates		
	$f_{c,\theta}/f_{ck}$	$\varepsilon_{c1,\theta}$	$\varepsilon_{cu1,\theta}$	$f_{c,\theta}/f_{ck}$	$\varepsilon_{c1,\theta}$	$\varepsilon_{cu1,\theta}$
[°C]	[-]	[-]	[-]	[-]	[-]	[-]
1	2	3	4	5	6	7
20	1,00	0,0025	0,0200	1,00	0,0025	0,0200
100	1,00	0,0040	0,0225	1,00	0,0040	0,0225
200	0,95	0,0055	0,0250	0,97	0,0055	0,0250
300	0,85	0,0070	0,0275	0,91	0,0070	0,0275
400	0,75	0,0100	0,0300	0,85	0,0100	0,0300
500	0,60	0,0150	0,0325	0,74	0,0150	0,0325
600	0,45	0,0250	0,0350	0,60	0,0250	0,0350
700	0,30	0,0250	0,0375	0,43	0,0250	0,0375
800	0,15	0,0250	0,0400	0,27	0,0250	0,0400
900	0,08	0,0250	0,0425	0,15	0,0250	0,0425
1000	0,04	0,0250	0,0450	0,06	0,0250	0,0450
1100	0,01	0,0250	0,0475	0,02	0,0250	0,0475
1200	0,00	-	-	0,00	-	-

The stress-strain relation for strains up to $\varepsilon_{c1,\theta}$ is defined by:

$$\sigma = \frac{3 \cdot \varepsilon \cdot f_{c,\theta}}{\varepsilon_{c1,\theta} \cdot \left(2 + \left(\frac{\varepsilon}{\varepsilon_{c1,\theta}} \right)^3 \right)} \quad (2.16)$$

For strains larger than $\varepsilon_{c1,\theta}$, the Eurocode allows a descending branch to be linear or non-linear. Figure 2.7 shows the stress-strain curve for concrete at elevated temperatures.

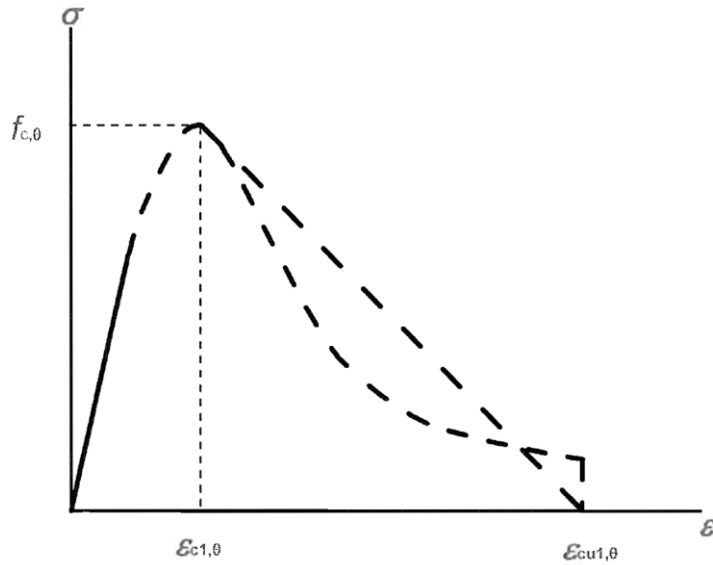


Figure 2.7: Stress strain-curve for concrete at elevated temperature according to the EN 1992-1-2 (BSI, 2004a)

Tension stiffening

Tension stiffening is the effect where concrete gradually, rather than immediately, loses its stiffness after cracking has occurred. This is caused by the reinforcement within the concrete which impacts the cracking behaviour of concrete. Without reinforcement, concrete will lose all of its strength as soon as it has cracked. However, with reinforcement, the stress is able to be transferred across the cracked concrete to the uncracked concrete which leads to an increased stiffness of the concrete section around the reinforcement.

In her research regarding membrane action of reinforced slabs, Deeny (2010) included tensioning stiffness by adjusting the stress-strain curve by including a linear descending branch as shown in Figure 2.8. Deeny found that a suitable value for the tension stiffening factor, TS , is 10.

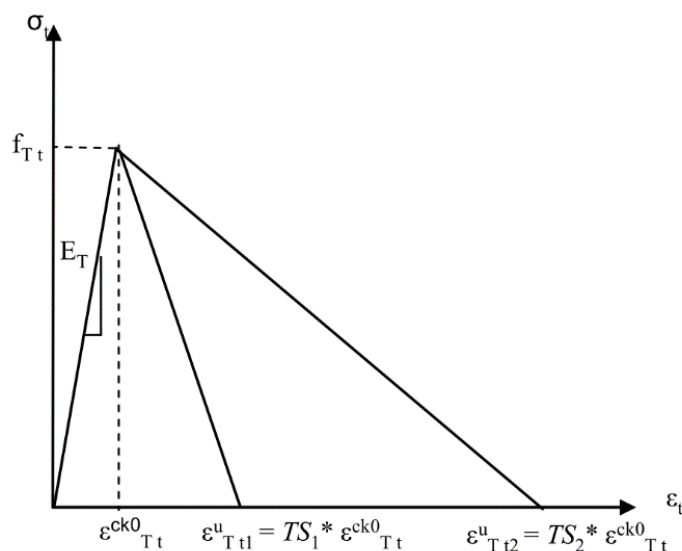


Figure 2.8: The inclusion of a descending branch to account for tension stiffening after the concrete has cracked (Deeny, 2010)

The advantage of including the tensions stiffness in the stress strain curve is that it helps avoid numerical instability when the concrete starts to crack, as the concrete does not abruptly lose its strength. The aforementioned model by Deeny will be adopted in this work.

Thermal properties

The thermal strain, ε_{th} , for siliceous and calcareous aggregate can be calculated with the following equations that are provided in Eurocode 1992-1-2:

Siliceous aggregate:

$$\varepsilon_{th} = -1.8 \cdot 10^{-4} + 9 \cdot 10^{-6} \cdot \theta + 2.3 \cdot 10^{-11} \cdot \theta^3 \quad \text{for} \quad 20^\circ\text{C} < \theta < 700^\circ\text{C} \quad (2.17)$$

$$\varepsilon_{th} = 14 \cdot 10^{-3} \quad \text{for} \quad 700^\circ\text{C} < \theta < 1200^\circ\text{C} \quad (2.18)$$

Calcareous aggregate:

$$\varepsilon_{\theta} = -1.2 \cdot 10^{-4} + 6 \cdot 10^{-6} \cdot \theta + 1.4 \cdot 10^{-11} \cdot \theta^3 \quad \text{for} \quad 20^\circ\text{C} < \theta < 805^\circ\text{C} \quad (2.19)$$

$$\varepsilon_{\theta} = 12 \cdot 10^{-3} \quad \text{for} \quad 805^\circ\text{C} < \theta < 1200^\circ\text{C} \quad (2.20)$$

The thermal strain for siliceous and calcareous aggregate concreted is illustrated in Figure 2.9.

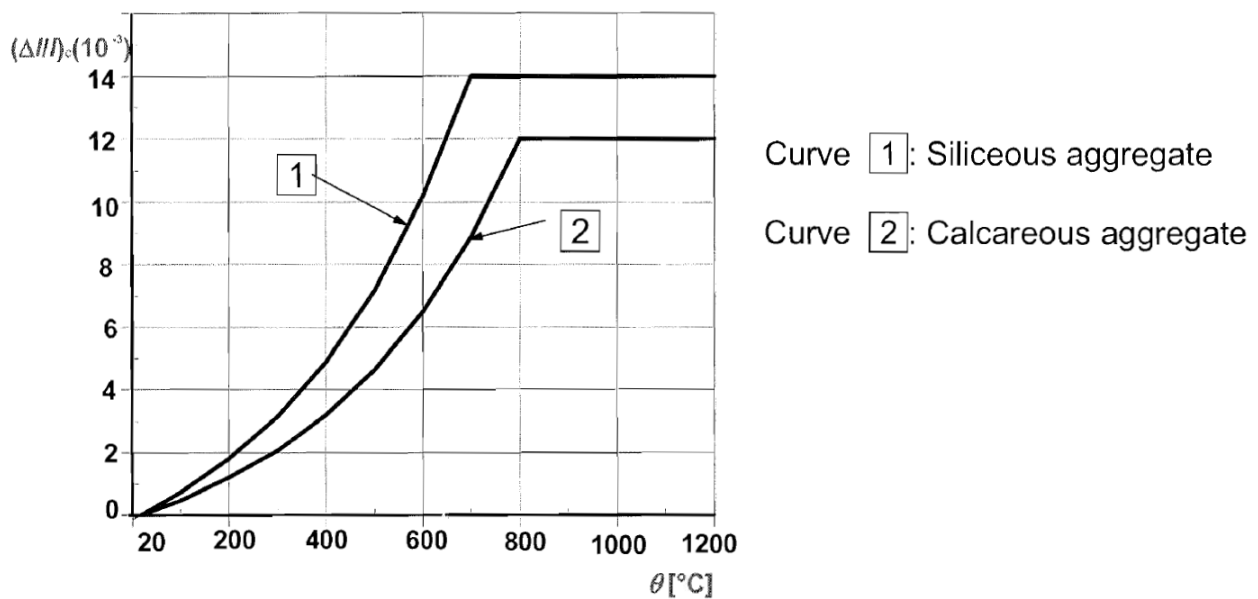


Figure 2.9: Thermal elongation of concrete consisting of (1) Siliceous aggregate and (2) Calcareous aggregate according to EN 1993-1-2 (BSI, 2004a)

2.4 Composite structures in fire

2.4.1 *Behaviour of a structure in fire compared to ambient temperature*

When a structure is designed for fire conditions, it is important that the designer has a good understanding of the behaviour of the structure in a fire, as the underlying assumptions for structural design at ambient temperatures may be violated at elevated temperatures. Gillie (2009) states that for ambient design geometric non-linearity can be neglected, due to the deflections being small, and the material response can be simplified as either linear-elastic or rigid-plastic. However, these simplification cannot be applied at elevated temperature when high temperature structural response is considered.

Firstly, during a fire, high axial loads can be introduced into the beams and columns if the beams are constrained by the rest of the structure, especially when the rest of the structures not affected by the fire. Furthermore, the material strength reduces significantly at elevated temperature.

Secondly, large deformations are likely to occur in a structure subjected to a fire, due to the loss of stiffness and thermal bowing. The reduction in stiffness and large deformations cause the load paths to change and loads will be resisted by different mechanisms than for ambient conditions. An example of this is the Tensile Membrane Action (TMA) (which is discussed further below), which is able to resist loads due to the large deformations of a slab. At ambient temperature the deflections and the effect of the TMA is insignificant. However, as large deflection occur during a fire, the effect of the TMA can become significant.

2.4.2 *Behaviour of a composite slab in a fire*

The Broadgate fire and Cardington Tests introduced in Chapter 1 showed that a composite floor may still have capacity even after the unprotected secondary beams have lost their strength. Figure 2.10 illustrates the behaviour of a rectangular slab panel that is vertically supported around its edge, as described by Bailey and Moore (2000a), where the secondary beam loses their strength and stiffness during the fire. The first behaviour mode of the slab panel is at ambient temperature, where the slab acts as a one way span and the loads are transferred from the slab to the secondary beams and from the secondary beams to the primary beams. In the second behaviour mode, a plastic hinge forms at the centre of the supporting beam and a fan yield pattern forms in the slab panel as the loads are transferred away from the hinge to the edge of the beam. As the secondary beam further loses its strength, a ‘cross’ yieldline pattern forms. The hinge will then ‘travel’ as the yieldline continually changes until the secondary beam has lost all of its strength and stiffness resulting in a ‘back-of-an-envelope’ yieldline pattern. At this stage, the fourth behaviour mode, the slab panel acts as two-way spanning slab and the loads are transferred directly to the edge supports of the slab.

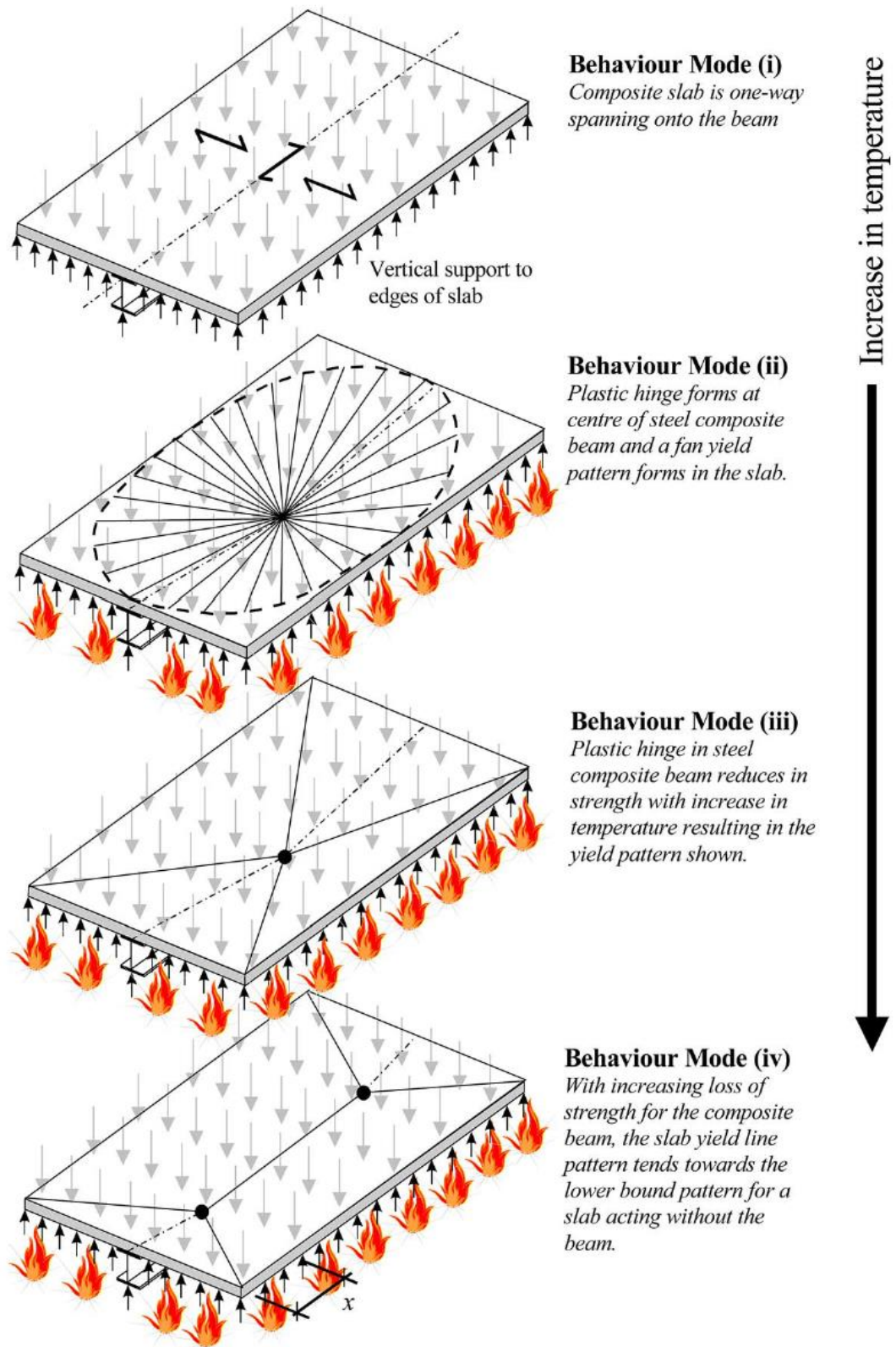


Figure 2.10: The progressive behaviour modes of a slab panel with increasing temperatures during a fire (Bailey and Moore, 2000a)

2.4.3 Collapse mechanisms of a slab panel

In the discussion above regarding the behaviour of a slab subjected to fire, the assumption was made that the edge of the slab are rigidly vertically supported. However, the edge support beams also undergo deflection and if the edge support beams undergo large deformations it will influence the collapse mechanism of the slab. Abu and Burgess (2010) have proposed different collapse mechanisms that can occur based on plastic hinges that occur in the support edge beams. These collapse mechanisms are illustrated in Figure 2.11. Note that these mechanisms are folding mechanism, which will not allow membrane forces to develop without horizontal restraint and therefore TMA cannot occur in these collapse mechanisms.

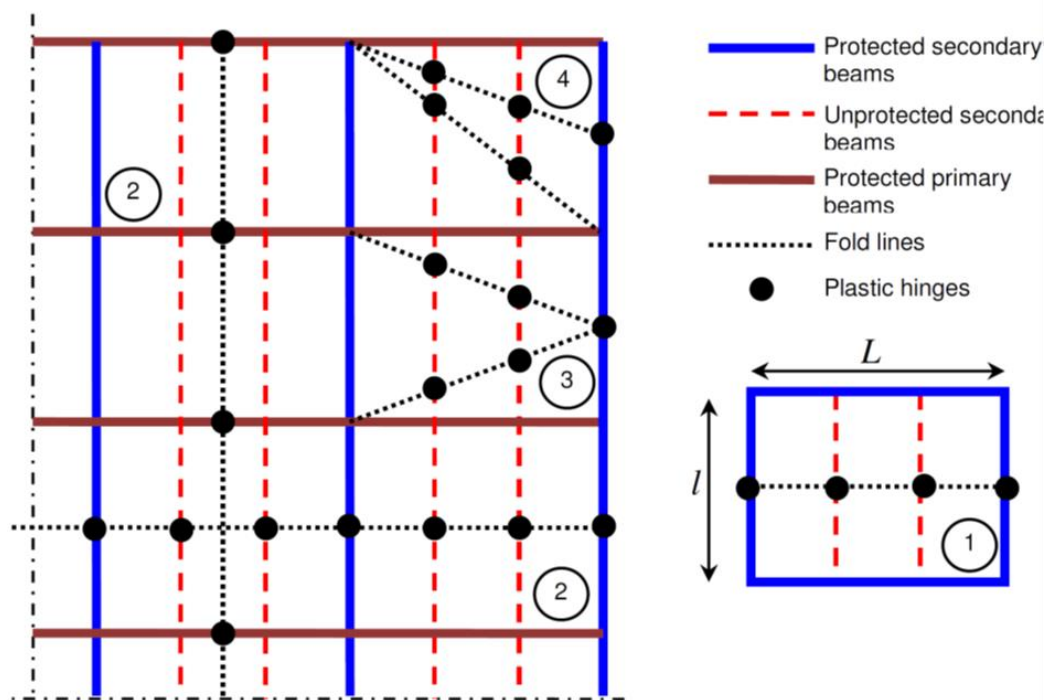


Figure 2.11: The different failing mechanism that can occur for a rectangular slab panel when plastic hinges form in the support beams (Abu & Burgess, 2010)

2.4.4 Tensile Membrane Action (TMA)

When thin slabs undergo large displacements, the load-carrying capacity of the slab increases due to TMA. TMA is a mechanism where the load-carrying capacity of the slab is increased due to the development of radial tension at the centre of the slab and a compression ring on the boundary of the slab (Abu, 2008), as illustrated in Figure 2.12. TMA is analogous to the catenary action that develop in beams with large displacements. However, unlike catenary action, TMA does not require horizontal restraint, as the compression ring resists the horizontal inward movement of the slab panel.

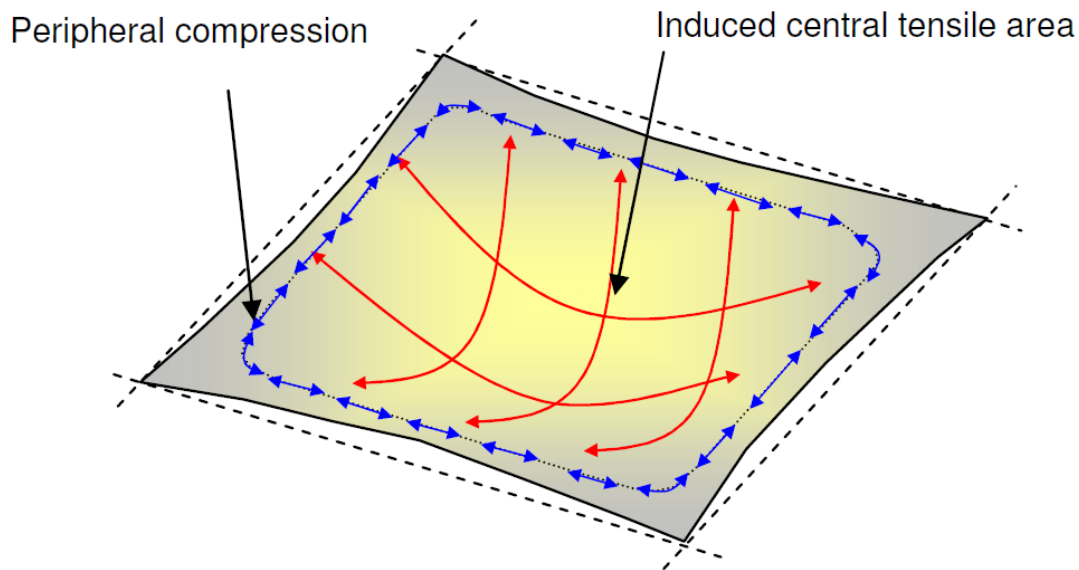


Figure 2.12: The development of tensile stresses at the centre of the slab panel and a compression ring at the perimeter of the slab panel due to large deformations of the slab panel (Abu, 2008)

When a slab panel is lightly reinforced, the capacity of the slab panel will be governed by the yieldline capacity of the slab panel, in which the slab panel fails due to a full depth crack that develops over the short span of the slab (Bailey, 2001). However, if a slab panel is highly reinforced, the capacity will be governed by the crushing of the concrete at the edge of the slab panel.

2.5 Analysis of structures in fire

2.5.1 Coupled and decoupled analysis

The term coupled analysis and decoupled analyses refers to whether the thermal analysis and the structural analysis are able to influence each other. With a coupled analysis, the fire and structural analysis are performed simultaneously, while with a decoupled analysis the thermal analysis are first performed and the structural analysis thereafter (Jiang *et al*, 2020).

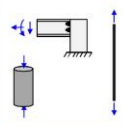
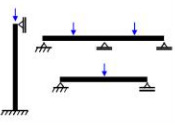
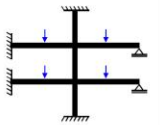
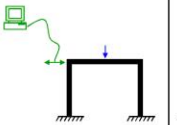
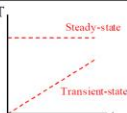

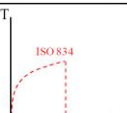

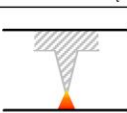
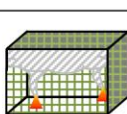
In a decoupled analysis the thermal analysis is performed first to determine the temperatures within the structural members. Thereafter, the temperatures are transferred to the structural model and the structural analysis is performed (Jiang *et al*, 2020). Therefore, the mechanical behaviour of the structure will have no impact on the thermal model.

When a thermal analysis and a structural analysis are coupled, the analysis is much more complex than a decoupled analysis and requires a significant amount of computational time. Due to the complexity of the coupled analysis, it is not practice to use for general structures. Therefore, decoupled analyses are most commonly used and implemented for structural fire analysis.

2.5.2 “Consistent level of crudeness” of an analysis

The “crudeness” of an analysis refers to complexity and ability of a model to capture the behaviour of the structure of fire accurately. The level of crudeness during the design process of a structure in fire should be consistent. Yet, detailed structural analyses are often performed on a full-scale model whilst using standard fires or an equivalent standard fire severity, and these systems represent different levels of model complexity. In a study on the level of detail/crudeness of the fire rating system, O’Loughlin and Lay (2015) reasoned that the crudeness of the whole design procedures will be governed by the crudest part. Therefore, the credibility of such models are constrained by the simplistic fire models, and detailed results from complex models cannot be produced from models utilising with simple inputs.

Figure 2.13 is presented by Gales et al (2012) demonstrating the range of fire models and structural models and credibility of combining the different models. The fire models are shown on the left and range from a simplistic standard fire curve to advanced fire models and real fires. The structural models are shown at the top and range from a single element to a full scale structure. The letters O/R indicate that the combination of the fire and structural model is suitable for occasional research and the letters M/C indicate that the combination of the fire and structural model have marginal credibility. On the top left of the diagram, a design procedure combining a standard fire with a single member are shown. This is typically done for prescriptive based designs based on the fire rating system. On the bottom right, a design procedure combining a real fire with a full-scale structure are shown. These designs are typically only performed for research due the complexity of the analysis. In practice, the most practical and reasonable design procedure would be those that combine fire models such as the parametric fire curve to zone models to models of subframes of restrained assemblies.

<div>Structural Model</div> <div>Fire Model</div>	Materials & Partial Elements	Single Elements	Sub-Frame Assemblies	Transiently Simulated Restrained Assemblies	Full-Scale Structures
					
Elevated Temperature Exposures (transient or steady-state)		Generate design/model input data [T]	O/R	M/C	M/C [E.1-2]
Standard Fires		Generate design input data [T]	Obtain fire resistance ratings (STANDARD) [O]	M/C [W]	M/C [A]
Equivalent Fire Severity to a Standard Fire		Validation of fire severity concept [Q]	Obtain fire resistance ratings (using alternative metric for fire severity) [Q]	O/R	M/C [B];[G];[N]
Parametrically Defined Model Fires		Generate design input data (highly dependant time-temperature phenomenon)	O/R [K];[M];[R];[S]	O/R	O/R [E.3-5]; [H];[J];[L];[U];[V]
Localised Model Fires		Generate design input data (highly dependant time-temperature phenomenon)	O/R	O/R	O/R
Zone Model Fires		Research (highly dependant time-temperature phenomenon)	M/C	O/R	O/R [I]
Field Model Fires		Research (highly dependant time-temperature phenomenon)	M/C	M/C	O/R
Real Fires		Research (highly dependant time-temperature phenomenon) [P]	M/C [C];[D];[F]	O/R	Research REAL behaviour in a REAL fire [E.6]

M/C— of Marginal Credibility; O/R— used for Occasional Research

* Reference Table 1

Figure 2.13: The level of credibility for the combination of fire models with structural model according to Gales et al (2012)

2.5.3 Available software for the analysis of composite structures in fire

Various software packages are available that can be used to analyse composite structures in fire. Finite Element software that has been developed for analysing a structure in fire includes Vulcan, SAFIR and OpenSees, amongst others. A brief overview will be given of each of these finite element software.

SAFIR

SAFIR is a software developed for the modelling of structures subjected to a fire, which was developed at the University of Liege in Belgium (Franssen, 2005). The main objective of SAFIR is to determine the mechanical

behaviour of a structure during a fire and is able to perform a decoupled thermal and mechanical analysis. The software was developed such that temperature could be automatically transferred from the thermal analysis to the mechanical model. The temperature over a 2D or 3D beam-element is able to vary across the cross-section, but is constant along the length of a beam element, while the temperature is only able to vary over the height of a 3D shell element.

Vulcan

Vulcan is a software for the modelling of composite structures subjected to fire, developed at the University of Sheffield. Concrete slabs are modelled using a layered shell element, with each layer able to have different temperatures and material properties. The reinforcement within the slab is modelled with a smeared steel layer which only has stiffness in the direction of the reinforcement. The steel beams are modelled with a three nodes beam element, which is modelled about the centre of the slab. The slab and the steel beam are connected with a zero-length shear connection that is able to model full, partial or zero interaction between the slab and the steel beam (Huang, Burgess and Plank, 1999). The modelling setup used in Vulcan is illustrated in Figure 2.14.

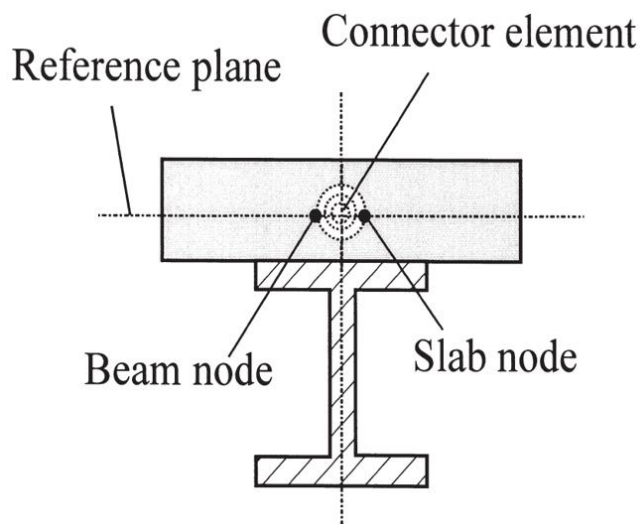


Figure 2.14: Modelling of composite beam in Vulcan connecting the beam element to the shell elements with a shear connector (Huang, Burgess and Plank, 1999)

OpenSees for fire

OpenSees is an opensource finite elements software, OpenSees was originally developed for earthquake analyses by the University of California, Berkeley (McKenna, Scott and Fenves, 2010), but has been developed to include the analysis structures in a fire by the University of Edinburgh (Jiang, Usmani and Li, 2014). *OpenSees for fire* will be discussed further in Chapter 4.

Composite beams can be modelled with a four-noded isoparametric shell element and two-noded 3D beam elements. The uniform thickness of the slab is modelled with shell elements, while concrete ribs and steel beams can be modelled with beam elements. These elements are connected using a rigid link that provides both

translational and rotational constraint. The modelling setup for a composite beam modelled in OpenSees is illustrated in Figure 2.15.

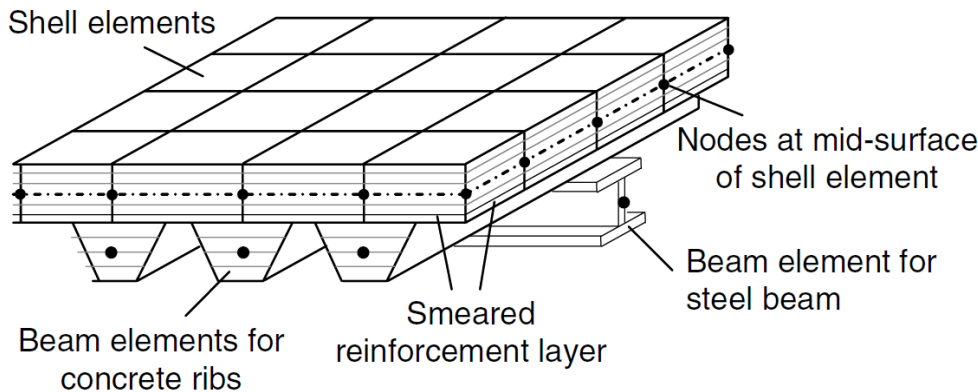


Figure 2.15: Modelling of a composite beam in OpenSees using shell elements and beam elements (Jiang, Usmani and Li, 2014)

2.6 Conclusion

In this chapter an overview has been given on literature regarding the design of composite structure in fire. First, an overview was provided regarding structural fire design, in which the strengths and weaknesses of prescriptive based design and performance design were discussed. Thereafter, the behaviour of compartment fires were discussed as well as fire models to estimate the compartment temperatures during a fire. These fire models range from simplistic temperature-time curves to a full CFD models of compartments. The two different approaches, active and passive, to protect a structure were discussed.

An overview of the material models of concrete and steel were given as provided by the Eurocode, with regard to mechanical properties and the thermal properties. Tension stiffening, as modelled by Deeny (2010) was also discussed, and will be utilised in forthcoming chapters. Thereafter, the difference in behaviour of a structure in fire relative to a structure at ambient conditions was highlighted. The behaviour of a composite slab during a fire was discussed, as well as possible collapse mechanisms. Tensile Membrane Action that occurs at large deformations was introduced.

Lastly, the analysis of structure in fire were discussed in terms of the different analysis consideration, which includes coupled and decoupled analysis, crudeness of the analysis and available software for the analysis of composite structures in fire. Lastly, the available software that were discussed were SAFIR, Vulcan and OpenSees. In the following chapter the Fire Beam Element will be developed within OpenSees to conduct decoupled analyses of structures.

3 Development of the Fire Beam Element for the analysis of three-dimensional skeletal structures

3.1 Introduction

The FBE methodology developed by Walls (2016) and implemented by Volkmann (2018) in OpenSees, is introduced in this chapter. The previous development of the FBE methodology will be briefly discussed and the fundamental theory of the FBE will be extended for a three-dimensional (3D) beam element. The focus of this chapter will be on (1) calculating the thermal effects caused by temperature increases during fire, through the use of a “pseudo-force”, called the Resultant Thermal Strain Load (RTSL) or Moment (RTSM), (2) the calculation of the strains within the beam, as well as the calculation of position of the Neutral Axes (NA). Neutral Axes refers to the axes at which moments cause zero axial strain and are determined independently for the moments about the strong and the weak axes. The Reference Axes (RA) are the axes at which the cross-section is modelled about (i.e. the RA will be the location of a beam's nodes in a FE model). Thereafter, (3) the finite element matrices will be developed for a 3D FBE. This will include a derivation of a modified stiffness matrix of a 3D beam element with an eccentric neutral axis based on an Euler-Bernoulli beam element. Lastly, (4) the implementation of the FBE in the design methodology will be discussed. Unless noted otherwise, the work in this chapter is based on the aforementioned FBE literature. The novel contribution of this chapter is the extension of the FBE stiffness matrices to account for 3D behaviour, along with the proposed methodology of how to model the influence of floor slabs considering lateral restraint.

The FBE formulation has significant similarities with the work by Bresler and his colleagues at Berkeley in the 1970s for concrete structures in fire (Bresler, Iding and Nizamuddin, 1977). From discussions by Franssen (2005) it appears that shortly after Bresler's work was developed the USA moved away from structural fire engineering modelling and so the work was not extensively used or validated. Similarities and differences between this work and the FBE formulation are discussed in Walls et al (2018).

3.2 Previous development and implementation of the FBE

As introduced in Chapter 1, the FBE methodology was developed with the goal of providing a simplified analysis tool that will accurately determine the behaviour of a structure subjected to a fire. The formulation is based upon a corotational finite beam element, which considers nonlinear behaviour and a NA position that can change during the analysis.

The FBE methodology was implemented by Volkmann (2018) in the open source finite element analysis (FEA) software named OpenSees, as will be discussed in Chapter 4. This enabled the FBE methodology to be applied to global analyses where the effect of the boundary constraints and structural continuity could be considered. However, only single axis bending was considered and therefore, the FBE methodology could only be applied to 2D structures.

In order to implement the FBE into the design methodology proposed in this work, the FBE methodology had to be developed for a 3D beam element. Therefore, in this section, the FBE will be extended by applying the fundamental theory of the FBE to bending about the strong and the weak axes, and by developing finite element matrices for 3D FBEs.

3.3 Fundamental theory of the Fire Beam Element

The fundamental theory of the FBE is extended for a three-dimensional beam element in this section. The fundamental theory of the FBE has some similarities with the `dispBeamColumnThermal`-element developed by Jiang (2012) in `OpenSees`. The similarities between these two formulations includes the use of (1) a corotational beam element, (2) Euler-Bernoulli assumptions and (3) the fibre section approach to calculate the section properties. However, the FBE and the `dispBeamColumnThermal`-element have fundamentally different approaches to account for the nonlinearity of the beam element. The FBE determines the stiffness matrix of the beam element at the NA, which is being updated at each step, and then transforms the stiffness matrix to the RA of the beam element. Whereas, the stiffness properties used for the `dispBeamColumnThermal`-element appear to be determined at the geometric neutral axis of the section. The stiffness matrix of the `dispBeamColumnThermal`-element are then determined through integrating over the beam element using Gauss-Lobatto quadrature (Jiang, 2012).

3.3.1 Fibre section

The FBE methodology uses a fibre section approach to calculate the section stiffness, section forces and the neutral axis of the cross-section. In a FEA, the fibres section approach can be implemented with subroutines to calculate the section properties of the FBE and therefore, the fibre section approach does not require any additional degrees of freedom. The fibre section approach consists of discretising the cross-section into fibres, with each fibre representing a small area, with a material model assigned to it. Therefore, a cross-section that consists of multiple material, can be modelled with fibres. However, the fibre section approach is limited in the sense that only full composite interaction between the materials can be modelled and that local buckling cannot be accounted for with the fibre section approach. Hence, for a concrete-steel composite beam, slippage between the concrete slab and the steel beam and lateral buckling behaviour of the steel beam cannot be considered with the fibre section approach.

The cross-sectional properties are calculated based upon all the fibres acting together. Furthermore, when the cross-section is subject to a temperature profile, the reduced stiffness, as well as the thermal elongation for each fibre can be calculated based on the temperature at the location of the fibre. In the case where the FBE is utilised for strong axis bending, only the elements over the height of a cross-section are required (i.e. each fibre can be the full width of the section). However, when bending about the weak axis is also considered, the cross-section requires small elements across its width as well, as shown in Figure 3.1.

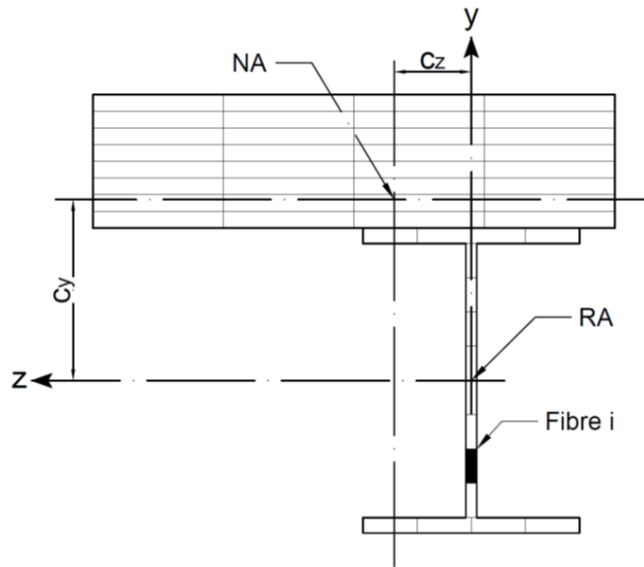


Figure 3.1: Example of a cross-section of a 3D beam-element with an eccentric NA from the RA, discretised into fibres

Note that in this work, the axis convention that is used in OpenSees is adopted, where the x-axis is along the axis of the beam-element and the z-axis and y-axis refer to the strong and weak axes of the cross-section. Figure 3.1 also indicates the NA and the RA system of the cross-section. The RA defines the position of the cross-section within the FEM model and does not change, whereas the NA is the axis about which the beam element is bending and due to the changing stiffness, the position of the NA will change during an analysis.

3.3.2 Loading on the Fire Beam Element

The FBE methodology makes provision for two types of loads: an applied mechanical load and a thermal load. The applied mechanical loads include applied loads such as distributed loads, as well as loads that develop due to cross-sectional restraint. The thermal loads include the increase in temperatures that cause beams to both elongate and experience curvature.

The FBE methodology has adopted the approach of representing thermal effects with a “pseudo-force”. This “pseudo-force” is the result of an Equivalent Thermal Stress (ETS) and causes the same deformation that the increase in temperature in the section would cause to a small area. By integrating the ETSs over a section a Resultant Thermal Strain Load (RTSL) and Moment (RTSM) are calculated, and is adopted in this work. The RTSL is a force that would cause the same axial elongation as the temperature profile in a cross-section, whilst the RTSM causes the equivalent curvature to the temperature gradient. Figure 3.2 illustrates the temperature profile over a cross-section, with the corresponding thermal strains, ETS and RTSL and RTSM.

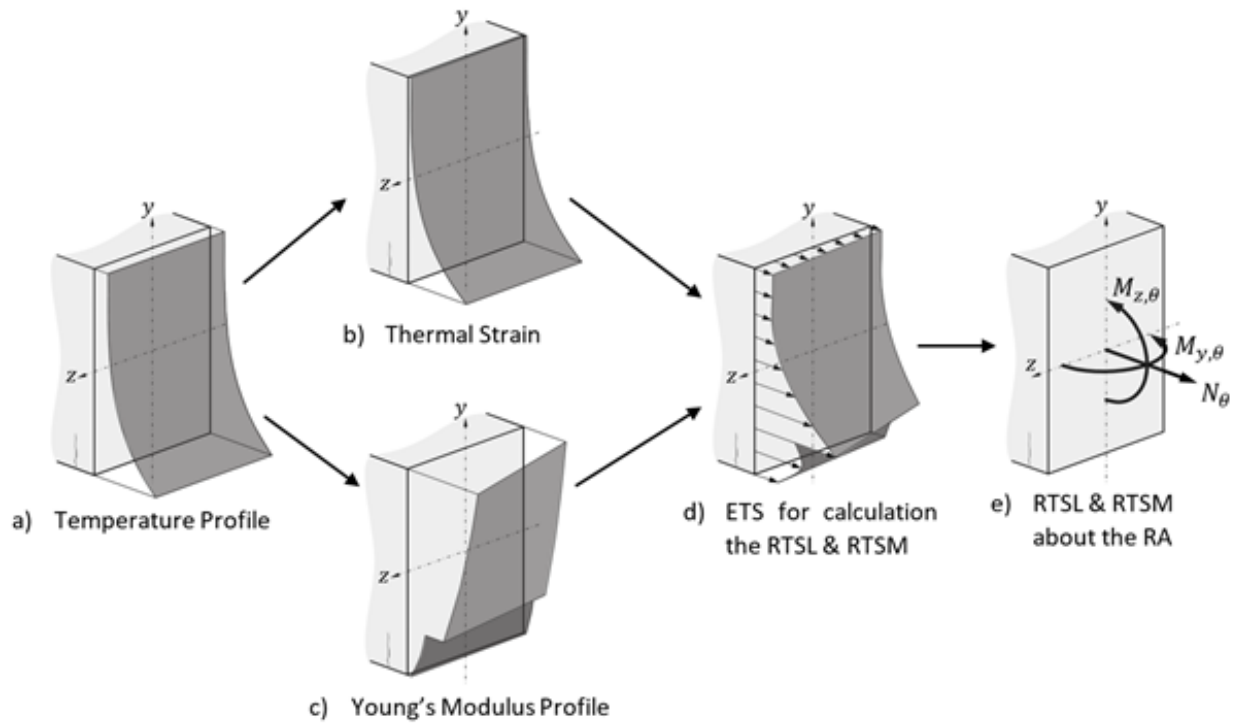


Figure 3.2: A cross-section subjected to a non-uniform temperature profile with the corresponding thermal strains, equivalent thermal strain (ETS) and resultant thermal strain load (RTSL) and moments (RTSM)

The thermal load vector of a cross-section, F_θ , contains the RTSL and RTSM. In the 2D FBE only the RTSM about the strong axis, $M_{z,\theta}$, is included in the thermal load vector. However, for a 3D FBE analysis the beam can be thermally and/or geometrically asymmetric in the direction of the strong axis, as well as in the direction of the weak axis. Therefore, the thermal load vector should also include the RTSM about the weak axis, $M_{y,\theta}$. Hence, the thermal load vector of the cross-section is given by Equation 3.1 and is illustrated in Figure 3.2 (e).

$$F_\theta = \begin{Bmatrix} N_\theta \\ M_{z,\theta} \\ M_{y,\theta} \end{Bmatrix} \quad (3.1)$$

With the fibre section Approach, the RTSL for a section can be calculated by summing the contribution of each fibre to the axial force, N_θ , moment about the strong axis, $M_{z,\theta}$, and the weak axis, $M_{y,\theta}$:

$$N_\theta = \sum_{i=1}^n E_{s,i,\theta} \cdot A_i \cdot \varepsilon_{i,\theta} \quad (3.2)$$

$$M_{y,\theta} = - \sum_{i=1}^n E_{s,i,\theta} \cdot A_i \cdot \varepsilon_{i,\theta} \cdot y_i \quad (3.3)$$

$$M_{z,\theta} = \sum_{i=1}^n E_{s,i,\theta} \cdot A_i \cdot \varepsilon_{i,\theta} \cdot z_i \quad (3.4)$$

where y_i and z_i are the position in the RA, A_i the area and $E_{s,i,\theta}$, the secant stiffness of fibre i . Note that the moments are calculated about the reference axis of the section. However, in order to calculate the total strain from the applied mechanical load and the RTSL, the moments about the NA are required. Equation 3.5 and 3.6 can be used to transform the moments about the reference axis to the moments about the NA.

$$M_{z,NA} = M_{z,RA} + c_y N \quad (3.5)$$

$$M_{y,NA} = M_{y,RA} - c_z N \quad (3.6)$$

where c_y is the eccentricity of the NA along the y -axis and c_z is the eccentricity of the NA along the z -axis.

3.3.3 Axial strains in a fire

The total strain in material consists of the mechanical strain, ε_σ , thermal strain, ε_θ , creep and the transient strain. However, in the Eurocode (BSI, 2004a), the creep and transient strain is implicitly incorporated in the material models by means of the stress-strain curve and the reduction factors. Such an approach is adopted in this work. Therefore, the total strain is the sum of the mechanical strain and the thermal strain, as given by:

$$\varepsilon_T = \varepsilon_\sigma + \varepsilon_\theta \quad (3.7)$$

The stress in a material is calculated from the mechanical strain. However, the mechanical strain cannot be determined directly from the deformation, and therefore the mechanical strain needs to be calculated indirectly from the total and thermal strain. The thermal strain, conversely, can be directly calculated from the material model for a given material and the specified temperature. In this work the thermal strain, or elongation, is calculated using EN 1993-1-2 (BSI, 2005) for steel and EN 1992-1-2 (BSI, 2004a) for concrete as discussed in Section 2.3

3.3.4 Calculation of the total strain

The total axial force and moments that act upon a section are due to the applied mechanical loads and the equivalent thermal loads, and these are used to determine the total strain across the section. The axial force will cause an axial elongation and the moments will cause a curvature about the strong axis, κ_z , and the weak axis, κ_y . Figure 3.3 illustrates the strain that will develop over a cross-section of a 3D beam element that is subjected to an axial force, $N_{T,x}$, and moments about the strong, $M_{T,z}$, and the weak axis, $M_{T,y}$.

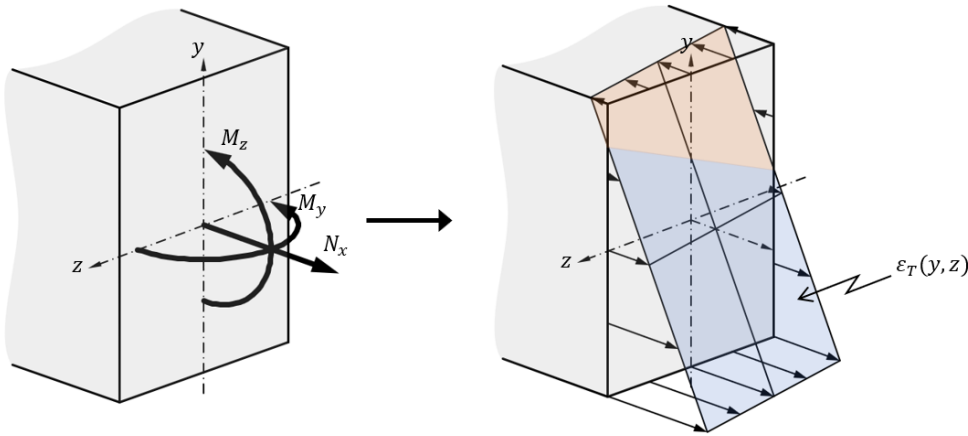


Figure 3.3: The total strain over a section that are subjected to an axial force and moments about the strong and the weak axis

The total strain at any location of the section can be calculated using Equation 3.8. However, this equation is only applicable when the moments are applied about the principle axis of section. The principle axis of a section is defined as the orientation of the axis where the product moments of inertia, EI_{yz} , are zero, which means that a moment about the z-axis can only cause a deflection in the y-direction of beam-element and vice versa. In this work, the product moment of inertia were assumed to be zero, as the beams are laterally supported by the slab and thus the moment about z-axis can only cause a deflection in the y-direction of the beam.

$$\varepsilon_T(y, z) = \varepsilon_{axial} - \kappa_z \cdot y + \kappa_y \cdot z = \frac{N + N_\theta}{E_s A_\theta} - \frac{M_z + M_{z,\theta}}{E_s I_{z,\theta}} \cdot y + \frac{M_y + M_{y,\theta}}{E_s I_{y,\theta}} \cdot z \quad (3.8)$$

Calculation of the mechanical strain

Following the assumption that plane sections remain plane, the total strain for a cross-section of a beam is linear. Thus, a non-linear thermal strain across the section will induce a mechanical strain in the material. This occurs especially in concrete and composite structures, where the temperatures in the bottom are significantly higher than at the top. Figure 3.4 show the mechanical strain that will develop in response to the thermal strain over a cross-section.

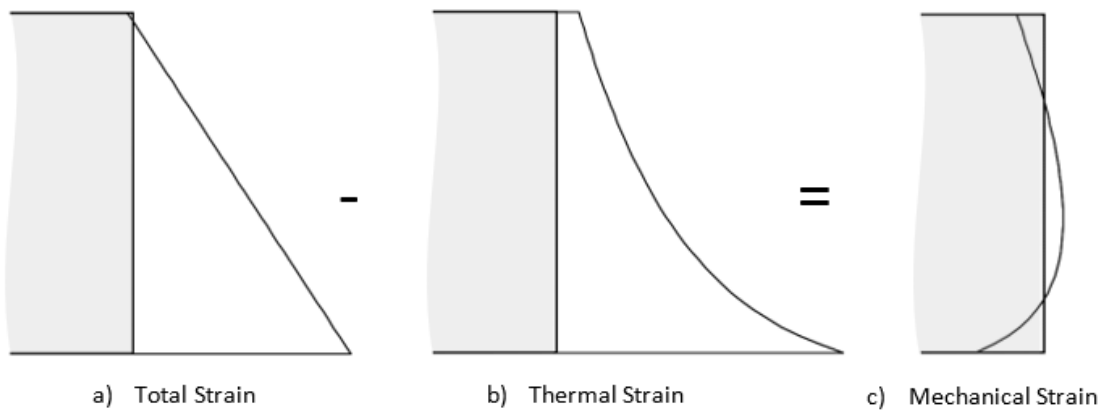


Figure 3.4: The mechanical strain that develops in a section in response to a non-linear thermal strain over a section

Figure 3.4 illustrates that compression can develop at the bottom and tension at the middle of the section during a fire, and not at the bottom of the beam as it would be during ambient conditions. However, if the moment is increased, the compression in the bottom of the beam will reduce and may become tension.

To calculate the mechanical strain, Equation 3.7 can be rewritten so that the mechanical strain will be in terms of the total strain and the thermal strain:

$$\varepsilon_{\sigma} = \varepsilon_T - \varepsilon_{\theta} \quad (3.9)$$

After the mechanical strain is calculated, the stiffness of the material and the stress in the material can be determined from the mechanical strain via the stress-strain curve of the material as illustrated in Figure 3.5.

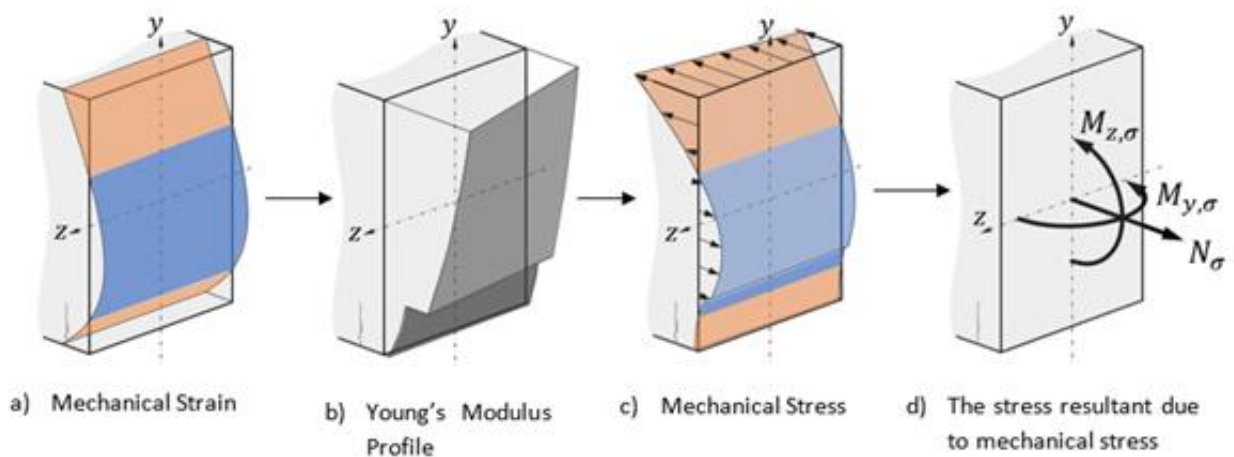


Figure 3.5: The stiffness profile, stress profile and stress resultant for a given mechanical strain profile over a cross-section

Figure 3.5 (e) illustrates the stress resultant, F_{σ} , defined in Equation 3.10, which are obtained by integrating the mechanical stress over the cross-section.

$$F_{\sigma} = \begin{Bmatrix} N_{\sigma} \\ M_{z,\sigma} \\ M_{y,\sigma} \end{Bmatrix} \quad (3.10)$$

3.4 Method for updating of the Neutral Axis and the stiffness of a section

When implementing the FBE methodology for a 3D beam element, the overall method to calculate the position of the NA is similar for the case of a 2D beam element. However, when applying the method additional calculations have to be done to calculate the bending stiffness about the weak axis of the section, $E_s I_{y,\theta}$, as well as the RTSM about the weak axis, $M_{y,\theta}$.

Figure 3.6 shows the method to calculate the position of the neutral axis and the section stiffness. The method consist of three phases: the input phase, the initial phase and the iterative phase.

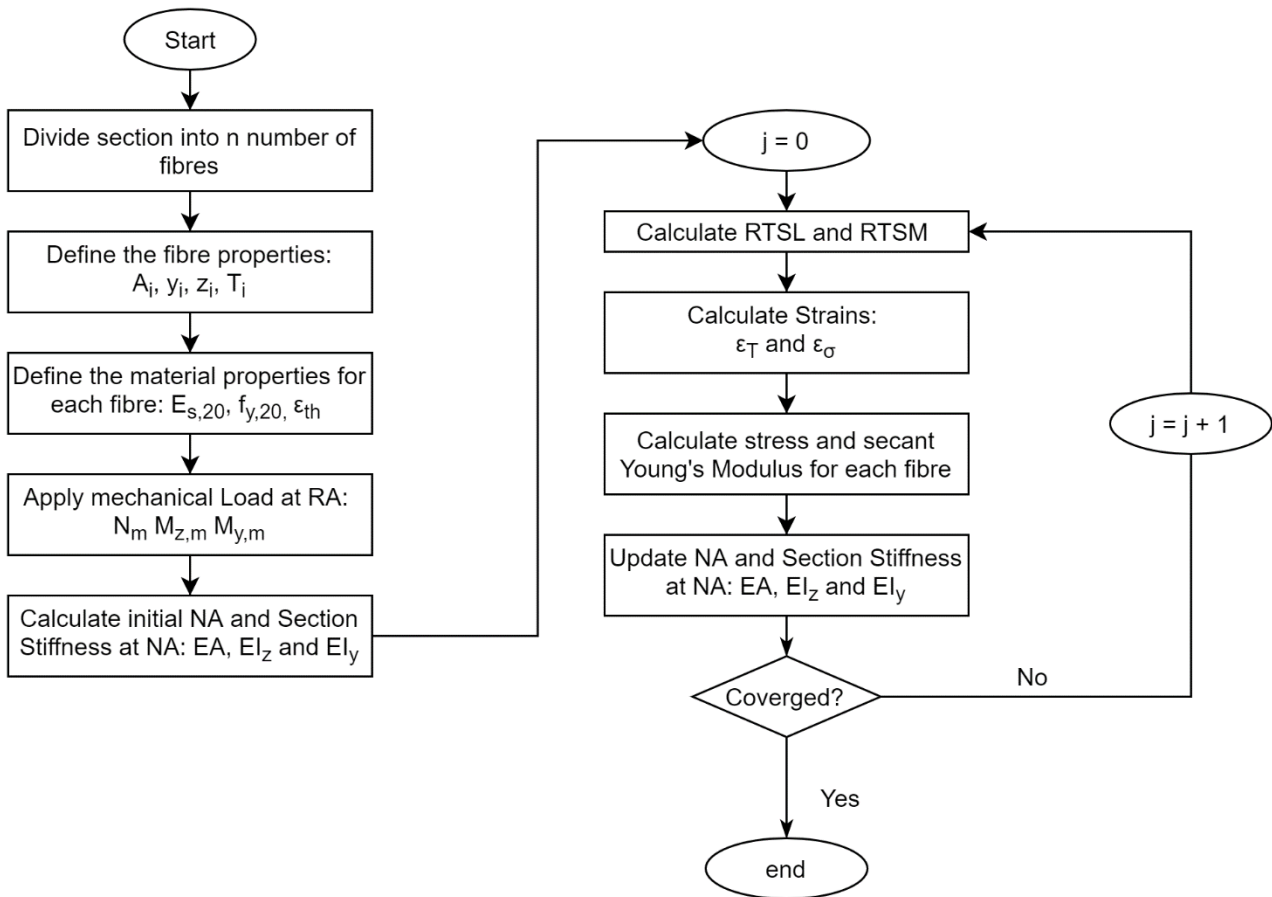


Figure 3.6: Flow chart illustrating the iterative method to calculate the neutral axis and section stiffness (adopted from Volkmann (2018))

3.4.1 Input required to calculate the neutral axis and section stiffness

The first phase in calculating the neutral axis and the section stiffness is to provide the section properties. As discussed in Section 3.3.1, a fibre section approach is followed. Thus, the section properties will be determined from the fibres. The input that is required for each fibre are the area, A_i , the location of the fibre in terms of its

height, y , and width, z , from the reference axis, the temperature of the fibre, T_i , and the material model of the fibre. The material of the fibre, the secant stiffness at ambient temperature, $E_{s,20}$, and the yield strength at ambient temperature, $f_{y,20}$, are also required, as well as the material response to an increase in temperature and its stress-strain curve. Lastly, the applied axial force, N_m , and the applied moments about the strong axis, $M_{z,m}$, and the weak axis, $M_{y,m}$, need to be provided.

3.4.2 Initial phase

In the initial phase, the location of the neutral axes and the section stiffness are calculated for the section, assuming the stress in the section to be zero. In other words, initial cross-sectional properties are calculated before the effect of the applied loads and thermal loads are considered.

In order to calculate the location of the neutral axis and the section stiffness, the effect of the temperature on the material is determined, which will result in a reduced secant stiffness, $E_{s,\theta}$, and a thermal strain, ε_θ . Note that the thermal strain will only be considered during the iterative phase once temperatures are applied. After the reduced secant stiffness of each fibre is determined the location of the NA about each axis is defined. For a 3D element, the components of the location of the NA from the reference axis are defined as the eccentricity of the NA along the strong axis, c_y , and the eccentricity of the NA along the weak axis, c_z , as shown in Figure 3.1. Equation 3.11 and 3.12 can be used to calculate the location of the neutral axes from the reference axis.

$$c_y = \frac{\sum_{i=1}^n E_{s,i,\theta} \cdot A_i \cdot y_i}{\sum_{i=1}^n E_{s,i,\theta} \cdot A_i} \quad (3.11)$$

$$c_z = \frac{\sum_{i=1}^n E_{s,i,\theta} \cdot A_i \cdot z_i}{\sum_{i=1}^n E_{s,i,\theta} \cdot A_i} \quad (3.12)$$

When the position of the NA is calculated, the secant stiffness is used in the equations, because the position of the NA is influenced by the total loading at the load step, as well as the history of the loading. Thereafter, the section stiffness about the neutral axis can be determined.

The section stiffness for a 3D element consists of the axial stiffness, EA_θ , the bending stiffness about the strong axis, $EL_{z,\theta}$, and the weak axis, $EL_{y,\theta}$, as well as the product moment of inertia, $EL_{yz,\theta}$. Equation 3.13 to Equation 3.16 can be used to calculate the section stiffness.

$$EA_\theta = \sum_{i=1}^n E_{i,\theta} \cdot A_i \quad (3.13)$$

$$EL_{z,\theta} = \sum_{i=1}^n E_{i,\theta} \cdot A_i \cdot y_i^2 - c_y^2 EA_\theta \quad (3.14)$$

$$EI_{y,\theta} = \sum_{i=1}^n E_{i,\theta} \cdot A_i \cdot z_i^2 - c_z^2 EA_\theta \quad (3.15)$$

$$EI_{yz,\theta} = \sum_{i=1}^n E_{i,\theta} \cdot A_i \cdot y_i \cdot z_i - c_y c_z EA_\theta \quad (3.16)$$

Depending on the iterative process used for analyses, either the tangent or secant Young's modulus will be used to calculate the section stiffness for determining changes in deformation from in a specific load step. In the case where load increments are used, for example the Newton-Raphson method, the tangent Young's modulus will be used to calculate the section stiffness and incremental change in deflection. If the total load is utilised, the secant Young's modulus should be used to calculate the section stiffness as this will predict a total deflection.

3.4.3 Iterative phase

In the initial phase, the location of the neutral axis and section stiffness were calculated for the section without any applied loads or equivalent thermal loads. But in the iterative phase, the neutral axes and section properties are updated to include the effect of the applied loads and equivalent thermal loads. This iterative process is repeated until the NA and section properties converge. In the FBE analysis, this will be done in each load step for each beam element.

The first step in the iterative phase is to calculate the equivalent thermal loads, as discussed in Section 3.3.2, using the thermal strain calculated in the initial phase and the secant stiffness of the material, determined in the previous iteration. Thereafter, the total loads are calculated from the applied loads and equivalent thermal loads.

With the applied loads and equivalent thermal loads, the total strain, ε_T , and mechanical strain, ε_σ , for each fibre are determined with Equation 3.7 and Equation 3.9, as discussed in Section 3.3.3. The mechanical strain is then used to determine stress and the secant stiffness of the material via the stress-strain curve for the material of the fibre. Note that typically these loads will be determined in a Finite Element Model analysis of the structure and then be provided for the section.

The secant stiffness of the material can then be used to calculate the updated location of the neutral axis with Equation 3.11 and 3.12, as in the initial phase. Lastly, the section stiffness can be calculated about the updated neutral axis with Equation 3.13 to Equation 3.16, as in the initial phase.

3.5 Finite element matrices for a Fire Beam Element in a 3D frame model

At the fundamental level, the force-displacement relationship of a structure is represented by the following equation:

$$\{F\} = [K]\{U\} \quad (3.17)$$

where $\{F\}$ is the load vector, $[K]$ is the stiffness matrix and $\{U\}$ is the displacement vector of the global structure. The global stiffness matrix is built up from the contribution of the local stiffness matrix of each individual element. Figure 3.7 illustrates an individual 3D beam-element with twelve degrees of freedom (DOF). In this discussion, only the aspects of Finite Element Analysis (FEA) that is relevant to development of the finite element matrices for the 3D FBE are discussed. For a detailed discussion regarding FEA refer to Bhatti (2006).

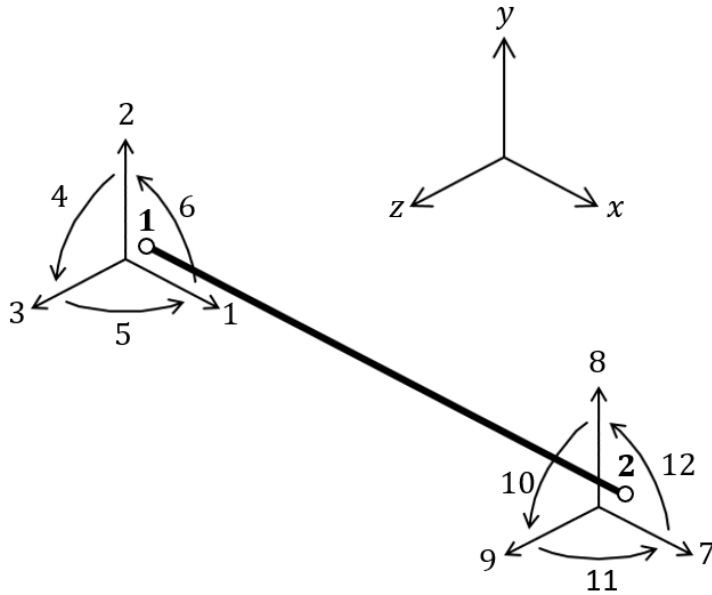


Figure 3.7: Three-dimensional beam element with twelve degrees of freedom

The load vector, $\{f_{12}\}$, and the deformation vector, $\{u_{12}\}$, for an single beam element are given in Equation 3.18 and Equation 3.19, respectively.

$$\{f_{12}\} = [f_{x1} \ f_{y1} \ f_{z1} \ m_{x1} \ m_{y1} \ m_{z1} \ f_{x2} \ f_{y2} \ f_{z2} \ m_{x2} \ m_{y2} \ m_{z2}]^T \quad (3.18)$$

$$\{u_{12}\} = [u_1 \ v_1 \ w_1 \ \phi_{x1} \ \phi_{y1} \ \phi_{z1} \ u_2 \ v_2 \ w_2 \ \phi_{x2} \ \phi_{y2} \ \phi_{z2}]^T \quad (3.19)$$

3.5.1 Finite element matrices for a Euler-Bernoulli beam element

The stiffness of a beam element consists of an elastic stiffness matrix, $[k_{el}]$, and the geometrical stiffness matrix, $[k_g]$. The elastic stiffness matrix represents the stiffness of the beam element with regards to deformation of the beam element. The geometric stiffness matrix takes into account the effect of the internal force on the stiffness of the beam element due to the deformation of the beam element, i.e. internal loads cause member deformations, and an out-of-straight member typically has a lower stiffness, especially as the member approaches the Euler buckling load.

In the previous FBE work the Euler-Bernoulli beam element was used for the elastic stiffness of the 2D FBE. The elastic stiffness matrix for a 3D Euler-Bernoulli beam is given in Equation 3.20, based on the elastic

stiffness matrix developed by Yang et al (1986). The beam stiffness depends on the length of the beam, L , the axial stiffness, EA , the bending stiffness about the strong axis, EI_z , and the bending stiffness of the weak axis, EI_y , of the cross-section of the beam. These properties will be calculated with subroutines, using the fibre section approach, as discussed in Section 3.3. The beam stiffness also depends on the torsional stiffness of the beam section, GJ . However, as the effect of torsion is not investigated in this research, and the torsional stiffness need to be calculated before an analysis, or during the first iteration, and provided as input for the beam element in order to complete the stiffness matrix in OpenSees. This will be discussed further in Section 3.6.

$$k_{el} = \begin{bmatrix} \frac{EA}{L} & 0 & 0 & 0 & 0 & 0 & -\frac{EA}{L} & 0 & 0 & 0 & 0 & 0 \\ \frac{12EI_z}{L^3} & 0 & 0 & 0 & \frac{6EI_z}{L^2} & 0 & -\frac{12EI_z}{L^3} & 0 & 0 & 0 & \frac{6EI_z}{L^2} \\ \frac{12EI_y}{L^3} & 0 & -\frac{6EI_y}{L^2} & 0 & 0 & 0 & 0 & -\frac{12EI_y}{L^3} & 0 & -\frac{6EI_y}{L^2} & 0 \\ \frac{GJ}{L} & 0 & 0 & 0 & 0 & 0 & 0 & 0 & -\frac{GJ}{L} & 0 & 0 \\ 0 & \frac{4EI_y}{L} & 0 & 0 & 0 & 0 & \frac{6EI_y}{L^2} & 0 & \frac{2EI_y}{L} & 0 \\ 0 & \frac{4EI_z}{L} & 0 & 0 & 0 & -\frac{6EI_z}{L^2} & 0 & 0 & 0 & \frac{2EI_z}{L} \\ \frac{EA}{L} & 0 & 0 & 0 & 0 & 0 & 0 & 0 & 0 & 0 \\ \frac{12EI_z}{L^3} & 0 & 0 & 0 & 0 & 0 & 0 & 0 & 0 & -\frac{6EI_z}{L^2} \\ \frac{12EI_y}{L^3} & 0 & \frac{6EI_y}{L^2} & 0 & 0 & 0 & 0 & 0 & 0 & 0 \\ \frac{GJ}{L} & 0 & 0 & 0 & 0 & 0 & 0 & 0 & 0 & 0 \\ 0 & \frac{4EI_y}{L} & 0 & 0 & 0 & 0 & 0 & 0 & 0 & 0 \\ 0 & \frac{4EI_z}{L} & 0 & 0 & 0 & 0 & 0 & 0 & 0 & 0 \end{bmatrix} \quad (3.20)$$

sym

Cai et al (2009) has developed the geometric stiffness matrix, given in Equation 3.21, for a beam element in a corotational framework, which will be used in this research. This geometric stiffness accounts for the effect of the axial force, P , on the stiffness of the beam element due to the transverse displacements and rotations. The axial force is defined as positive for tension and negative for compression. When the element is in compression, the geometric stiffness reduces the stiffness of the element.

$$k_g = \begin{bmatrix}
0 & 0 & 0 & 0 & 0 & 0 & 0 & 0 & 0 & 0 & 0 & 0 \\
& \frac{6P}{5L} & 0 & 0 & 0 & \frac{P}{10} & 0 & -\frac{6P}{5L} & 0 & 0 & 0 & \frac{P}{10} \\
& & \frac{6P}{5L} & 0 & -\frac{P}{10} & 0 & 0 & 0 & -\frac{6P}{5L} & 0 & -\frac{P}{10} & 0 \\
& & & 0 & 0 & 0 & 0 & 0 & 0 & 0 & 0 & 0 \\
& & & & \frac{2PL}{15} & 0 & 0 & 0 & \frac{P}{10} & 0 & -\frac{PL}{30} & 0 \\
& & & & & \frac{2PL}{15} & 0 & -\frac{P}{10} & 0 & 0 & 0 & -\frac{PL}{30} \\
& & & & & & 0 & 0 & 0 & 0 & 0 & 0 \\
& & & & & & & \frac{6P}{5L} & 0 & 0 & 0 & -\frac{P}{10} \\
& & & & & & & & \frac{6P}{5L} & 0 & \frac{P}{10} & 0 \\
& & & & & & & & & 0 & 0 & 0 \\
& & & & & & & & & & \frac{2PL}{15} & 0 \\
& & & & & & & & & & & \frac{2PL}{15}
\end{bmatrix} \quad (3.21)$$

sym

3.5.2 Derivation of the modified stiffness matrix

Walls (2016) derived the stiffness matrix for a 2D element with a NA that is eccentric from the RA. This derivation will be extended for a 3D beam element, following the same approach.

The approach consists of considering a deformed beam, as shown in Figure 3.8, at time t , in a rotated frame, which then deflects further to an updated position at $t + \Delta t$. The relationship between deflection of the node on the NA, Node A, and a node on the RA, Node 1, are then derived, as well as, the relationship between the forces in the NA and the RA. The two relationships are applicable to Node B and Node 2 and are then used to transform the stiffness matrix of a beam from the neutral axis, k_{AB} , to the reference axis of the beam, k_{12} .

An underlying assumption in the derivation is that the angle of the rotations are small, such that $\sin(x) \approx x$. This assumption also allows that the rotation about each plane can be considered to be independent from each other. Hence, the modified stiffness matrix for the 3D beam element can be derived by deriving the relationship between Node A and Node 1 in the local YZ-plane, ZX-plane and XY-plane separately and then to combine it.

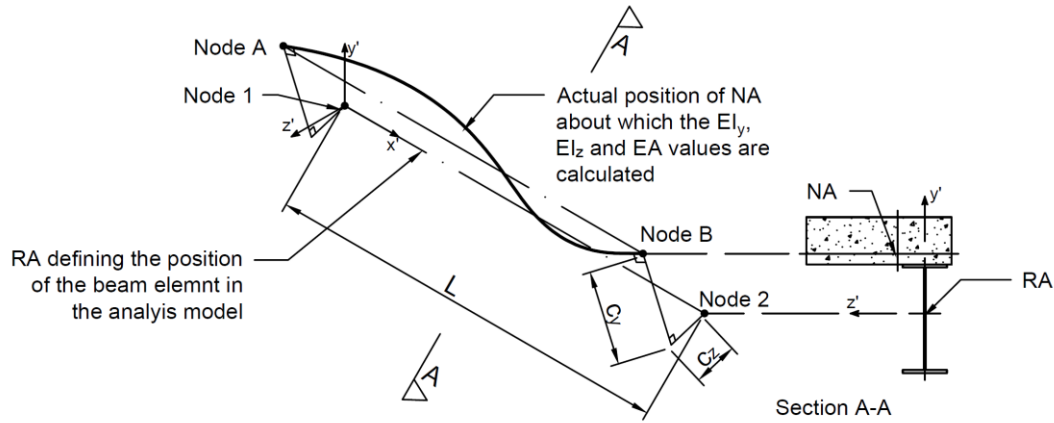


Figure 3.8: Deformed beam between Node 1 and Node 2 at time t with the NA parallel to the RA

Figure 3.9 shows a deflection from timestep t to timestep $t + \Delta t$ of the nodes on the RA and NA in the YZ-plane. The location of the neutral axes are measured along the y-axis, c_y , and the z-axis, c_z , from the reference axis. The relation between the position, in the YZ-plane, of Node A, $x_{A,yz}$, and Node 1, $x_{1,yz}$, are given in Equation 3.22.

$$\begin{aligned} \{x_{A,yz}\} = \begin{Bmatrix} y_A \\ z_A \\ \alpha_{x,A} \end{Bmatrix} &= \begin{bmatrix} 1 & 0 & 0 \\ 0 & 1 & 0 \\ 0 & 0 & 1 \end{bmatrix} \begin{Bmatrix} y_1 \\ z_1 \\ \alpha_{x,1} \end{Bmatrix} + c_y \begin{Bmatrix} \cos(\alpha_{x1}) \\ \sin(\alpha_{x1}) \\ 0 \end{Bmatrix} + c_z \begin{Bmatrix} -\sin(\alpha_{x1}) \\ \cos(\alpha_{x1}) \\ 0 \end{Bmatrix} \\ &\approx \begin{bmatrix} 1 & 0 & -c_z \\ 0 & 1 & c_y \\ 0 & 0 & 1 \end{bmatrix} \begin{Bmatrix} y_1 \\ z_1 \\ \alpha_{x,1} \end{Bmatrix} + \begin{Bmatrix} c_y \\ c_z \\ 0 \end{Bmatrix} = [Q_{yz}] \{x_{1,yz}\} + \begin{Bmatrix} c_y \\ c_z \\ 0 \end{Bmatrix} \end{aligned} \quad (3.22)$$

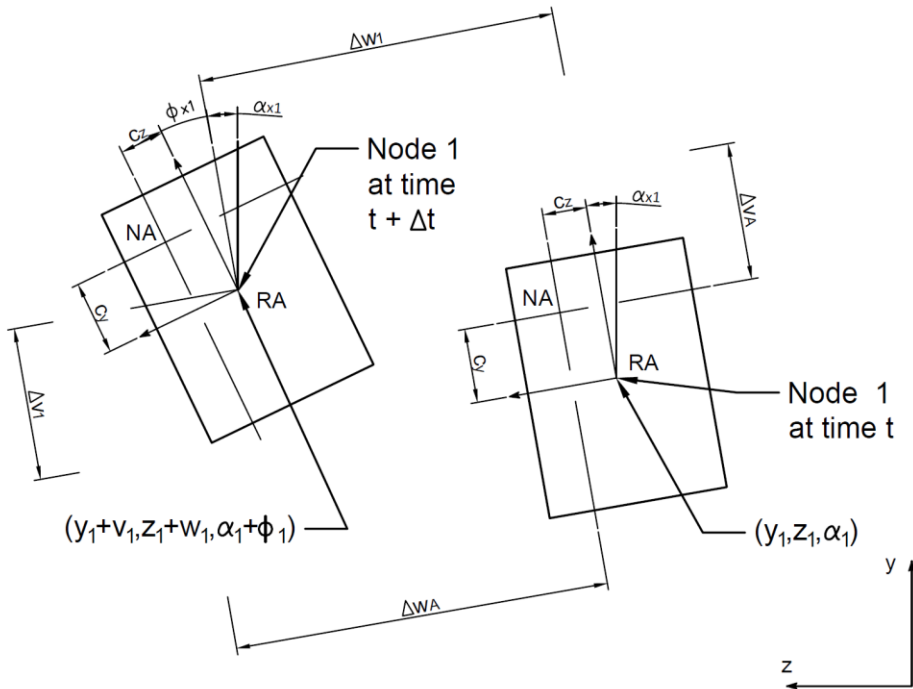


Figure 3.9: The deflection of a node of the beam in the YZ-plane from step t to step $t + \Delta t$, indicating the position of the RA and the NA

Furthermore, the relationship between the deflection, in the YZ-plane, of Node A, $\mathbf{u}_{A,yz}$, and Node 1, $\mathbf{u}_{1,yz}$, are as follows:

$$\begin{aligned} \{u_{A,yz}\} = \begin{Bmatrix} \Delta v_A \\ \Delta w_A \\ \Delta \phi_{x,A} \end{Bmatrix} &= \begin{bmatrix} 1 & 0 & 0 \\ 0 & 1 & 0 \\ 0 & 0 & 1 \end{bmatrix} \begin{Bmatrix} \Delta v_1 \\ \Delta w_1 \\ \Delta \phi_{x,1} \end{Bmatrix} + c_y \begin{Bmatrix} \cos(\alpha_{x1} + \phi_1) - \cos(\alpha_{x1}) \\ \sin(\alpha_{x1} + \phi_1) - \sin(\alpha_{x1}) \\ 0 \end{Bmatrix} \\ &+ c_z \begin{Bmatrix} -\sin(\alpha_1 + \phi_1) + \sin(\alpha_{x1}) \\ \cos(\alpha_{x1} + \phi_1) - \cos(\alpha_{x1}) \\ 0 \end{Bmatrix} \approx \begin{bmatrix} 1 & 0 & -c_z \\ 0 & 1 & c_y \\ 0 & 0 & 1 \end{bmatrix} \begin{Bmatrix} \Delta v_1 \\ \Delta w_1 \\ \Delta \phi_{x,1} \end{Bmatrix} = [Q_{yz}] \{u_{1,yz}\} \end{aligned} \quad (3.23)$$

In a similar way, the relationship between the displacement, in the ZX-plane and the XY-plane, of Node A and Node 1 can be derived and are given in Equation 3.24 and Equation 3.25, respectively.

$$\{u_{A,zx}\} \approx \begin{bmatrix} 1 & 0 & -c_y \\ 0 & 1 & 0 \\ 0 & 0 & 1 \end{bmatrix} \begin{Bmatrix} \Delta u_1 \\ \Delta v_1 \\ \Delta \phi_{z,1} \end{Bmatrix} = [Q_{zx}] \{u_{1,zx}\} \quad (3.24)$$

$$\{u_{A,xy}\} \approx \begin{bmatrix} 1 & 0 & c_z \\ 0 & 1 & 0 \\ 0 & 0 & 1 \end{bmatrix} \begin{Bmatrix} \Delta u_1 \\ \Delta w_1 \\ \Delta \phi_{y,1} \end{Bmatrix} = [Q_{xy}] \{u_{1,xy}\} \quad (3.25)$$

Note that Equation 3.24 describes the relation between the displacement of Node A and Node 1 for a two-dimensional beam element, as a 2D beam element only considers deformation in the local ZX-plane of the beam element.

The relationship between the displacements of the nodes in each plane can then be combined to form the relationship between the three-dimensional displacement of Node A and Node 1:

$$\{u_A\} = \begin{Bmatrix} \Delta u_A \\ \Delta v_A \\ \Delta w_A \\ \Delta \phi_{x,A} \\ \Delta \phi_{y,A} \\ \Delta \phi_{z,A} \end{Bmatrix} = \begin{bmatrix} 1 & 0 & 0 & 0 & c_z & -c_y \\ 0 & 1 & 0 & -c_z & 0 & 0 \\ 0 & 0 & 1 & c_y & 0 & 0 \\ 0 & 0 & 0 & 1 & 0 & 0 \\ 0 & 0 & 0 & 0 & 1 & 0 \\ 0 & 0 & 0 & 0 & 0 & 1 \end{bmatrix} \begin{Bmatrix} \Delta u_1 \\ \Delta v_1 \\ \Delta w_1 \\ \Delta \phi_{x,1} \\ \Delta \phi_{y,1} \\ \Delta \phi_{z,1} \end{Bmatrix} = [Q] \{u_1\} \quad (3.26)$$

The relationship between the forces in the neutral axis and the reference axis are given in Equation 3.27.

$$\{f_A\} = \begin{Bmatrix} f_{x,A} \\ f_{y,A} \\ f_{z,A} \\ m_{x,A} \\ m_{y,A} \\ m_{z,A} \end{Bmatrix} = \begin{bmatrix} 1 & 0 & 0 & 0 & 0 & 0 \\ 0 & 1 & 0 & 0 & 0 & 0 \\ 0 & 0 & 1 & 0 & 0 & 0 \\ 0 & c_z & -c_y & 1 & 0 & 0 \\ -c_z & 0 & 0 & 0 & 1 & 0 \\ c_y & 0 & 0 & 0 & 0 & 1 \end{bmatrix} \begin{Bmatrix} f_{x,1} \\ f_{y,1} \\ f_{z,1} \\ m_{x,1} \\ m_{y,1} \\ m_{z,1} \end{Bmatrix} = [W] \{f_1\} \quad (3.27)$$

For the remainder of this discussion, the derivation of the modified stiffness matrix for a 3D beam element is the same as for a 2D beam element. However, the rest of the derivation is included in order to give the complete view on how the modified stiffness matrices are developed.

The deformation vector, \mathbf{u}_{12} , of a beam was given in Equation 3.19, which consists of the start, Node 1, and end node, Node 2, of the beam. Thus, the deformation vector can be transformed from the RA to the NA, by transforming each node from the reference axis to the neutral axis, with Equation 3.28. The subscript AB refer to the nodes at NA and 12 refer to the nodes at the RA, as shown in Figure 3.8.

$$\{u_{AB}\} = \begin{Bmatrix} u_A \\ u_B \end{Bmatrix} = \begin{bmatrix} Q & 0 \\ 0 & Q \end{bmatrix} \begin{Bmatrix} u_1 \\ u_2 \end{Bmatrix} = [Q_{AB}]\{u_{12}\} \quad (3.28)$$

Similarly the load vector, \mathbf{f}_{12} , of the beam can be transformed from RA to the NA with Equation 3.29. As well as from the neutral axis to the reference axis with Equation 3.30.

$$\{f_{AB}\} = \begin{Bmatrix} f_A \\ f_B \end{Bmatrix} = \begin{bmatrix} W & 0 \\ 0 & W \end{bmatrix} \begin{Bmatrix} f_1 \\ f_2 \end{Bmatrix} = [W_{AB}]\{f_{12}\} \quad (3.29)$$

$$\{f_{12}\} = \begin{Bmatrix} f_1 \\ f_2 \end{Bmatrix} = \begin{bmatrix} W & 0 \\ 0 & W \end{bmatrix}^{-1} \begin{Bmatrix} f_A \\ f_B \end{Bmatrix} = [W_{AB}]^{-1}\{f_{AB}\} \quad (3.30)$$

The force-displacement behaviour of the beam element at the neutral axis are as follows:

$$\{f_{AB}\} = [k_{AB}]\{u_{AB}\} \quad (3.31)$$

where, k_{AB} , is the stiffness matrix about the neutral axis of the beam element, as discussed in Section 3.5.1. Substituting Equation 3.28 in Equation 3.31 and then into Equation 3.30, the following equation can be obtained:

$$\{f_{12}\} = [W_{AB}]^{-1}[k_{AB}][Q_{AB}]\{u_{12}\} \quad (3.32)$$

However:

$$[W_{AB}]^{-1} = [Q_{AB}]^T \quad (3.33)$$

Thus, the force-displacement behaviour of the beam element at the reference axis can be expressed as follows:

$$\{f_{12}\} = [Q_{AB}]^T[k_{AB}][Q_{AB}]\{u_{12}\} \quad (3.34)$$

From Equation 3.34, the relationship between the stiffness matrix of a beam at the NA and at the RA can be expressed as follows:

$$[k_{12}] = [Q_{AB}]^T[k_{AB}][Q_{AB}] \quad (3.35)$$

Hence, Equation 3.35 derived above for a 3D element can be used to relate the stiffness of the nodal positions in an elegant manner.

3.6 Applying the Fire Beam Element into the design methodology

When analysing a skeletal structure of a composite steel structure, the structure consists of supporting beams and columns. The cross-sectional properties of the column can be determined with the fibre section approach. Further research is required regarding the effect of fire on the torsional stiffness of a section, but in this work the columns and the beams will be modelled such that they are torsionally constrained, based on the geometry of structures modelled. However, a torsional stiffness is still required for the finite element matrix of the FBE. Hence, for the 3D FBE, the torsional stiffness can be estimated at ambient temperature based on the geometry

of the section and applied. The nature of the case studies considered in Chapter 6 highlights that the structures considered experienced negligible torsional effects and so the assumption is justified, although for unusual geometries this may not necessarily be the case.

The supporting beams modelled as part of skeletal frames consist of the steel beam that act compositely with an effective width of the slab. The use of the fibre section to model the section of the FBE allows that multiple materials can be used to model a section. Therefore, the concrete slab and the steel section can be modelled as one section for a FBE. However, this means that the effect of slippage between the slab and the steel beam will be ignored, for the FBE in its current formulation.

When considering the supporting structure and slab as two separate systems, the lateral restraint that the slab provides for the support beams is not provided in the analysis of the skeletal structures, i.e. no floor slab is modelled and the floor slab prevents beams from moving laterally. To account for this, an assumption is made that the slab will provide sufficient lateral support to the support beams and that the support beams will be rigid about their horizontal axis. Figure 3.10 illustrates the cross-section of the composite beam that is laterally supported by the slab panel. The supports allows for vertical displacement of the cross-section, but constrain the cross-section against lateral movement and rotation. Therefore, the support beam will be laterally and torsionally rigid.

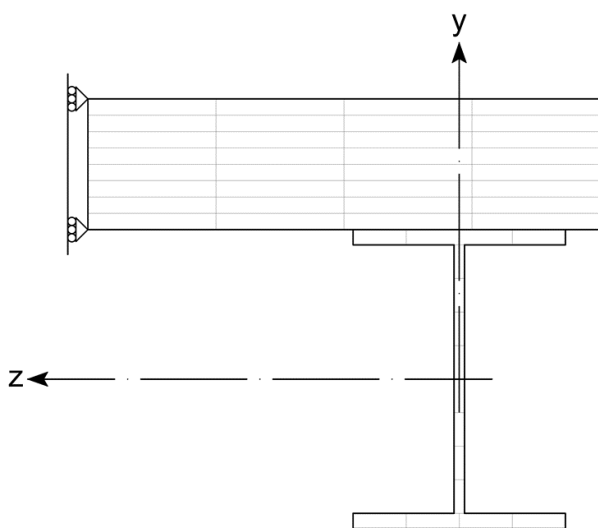


Figure 3.10: Modelled cross-section in the FBE analysis for the support beams accounting for the laterally support provided by the slab panel

To model this cross-section in the FBE analysis, a cross-section with an arbitrary high bending stiffness about the horizontal axis and torsional stiffness is assigned to the support beams in order to simulate the rigidity of the support about their horizontal axis. The implementation of the FBE with this laterally supported cross-section is discussed in Section 4.4.3.

Note that this restriction to the analysis to only be able to be used for predicting the horizontal deformation of the support beams, which is the aim of the FBE analysis. Therefore, the FBE analysis can be applied as long as the support beams are not directly subjected to a lateral load that may cause significant lateral deformation of the support beams.

3.7 Conclusion

In this chapter the FBE methodology was expanded for the analysis of 3D skeletal structures, extending the work of Walls (2016) and Volkmann (2018). The finite element matrices for the 3D beam element were developed by deriving a modified stiffness matrix based on Euler-Bernoulli assumptions that account for the eccentricity of the NA. The section properties of the beam-element were calculated with the fibre section approach. Each fibre represented a small area and different temperatures and material properties can be assigned to each fibre. For a 3D beam-element, the cross-section had to be discretised over the height and the width of the cross-section.

As with for a 2D FBE, the fibre section approach was used to determine the RTSL and RTSM (i.e. forces simulating elongation and curvature), the axial strains within the beams and the position of the NA. For a 3D beam the calculation had to be extended to include the RTSM about the weak axis, $M_{y,\theta}$, and to include the curvature about the weak axis in the calculation of the total strain. The overall method for updating the position of the NA remained similar as for a 2D beam. However, the calculations of the section stiffness had to be extended to include the bending stiffness about the weak axis, $E_S I_{y,\theta}$, and the position of the NA had to be calculated for the strong axis, c_y , as well as the weak axis, c_z .

Lastly, the application of the 3D FBE in an analysis of a skeletal structure was discussed. When beams and columns are modelled with the 3D FBE torsion is considered by an approximation of the torsional stiffness at ambient temperature, but since the structures considered are typically not torsionally sensitive this is considered suitable. Furthermore, the support beams can be assumed to be laterally supported by the slab. This can be accounted for by increasing the bending stiffness about the horizontal axis to prevent lateral-torsional buckling of the support beams.

4 Implementation of a three-dimensional FBE into OpenSees

4.1 Introduction

This section discusses the implementation of the FBE formulation for three-dimensional (3D) skeletal structures in the finite element software OpenSees. The implementation of the 3D FBE builds on the previous work where the FBE formulation was implemented for a 2D FBE (Volkman, 2018). In order to implement the 3D FBE, classes have been developed in OpenSees to incorporate the FBE formulation in the thermo-mechanical analysis. These classes were based on existing classes in OpenSees that were developed by Jiang (2012).

In this section, a brief overview will be given of OpenSees and the 2D FBE that was previously implemented in OpenSees. Thereafter, the process of the thermo-mechanical analysis that is being used in OpenSees will be discussed to show where the FBE formulation will be incorporated in the analysis. The functions of the classes that are required for the thermo-mechanical analysis, and had to be modified to incorporate calculate the eccentricity of the NA, will be discussed.

The novel contribution of this chapter is the implementation of a 3D element with a movable NA, based on the formulation developed in Chapter 3, that is updated during the thermo-mechanical analysis in a finite element software. This will enable the FBE formulation to be used to analyse a 3D skeletal structure and to be applied in the design methodology to design a full 3D structure.

4.2 Finite element software: OpenSees

4.2.1 Background of OpenSees

OpenSees is an open source Finite Element Software developed for academic use and research, along with commercial design. OpenSees was originally developed to analyse non-linear structural response, primarily for seismic actions (McKenna, Scott and Fenves, 2010). Since OpenSees is able to analyse non-linear structures subjected to dynamic loads it is suited for the analysis of structures at elevated temperature with transient heating conditions, which allowed *OpenSees for fire* to be developed (Jiang, Usmani and Li, 2014). *OpenSees for fire* contains classes for elements to which thermal actions can be applied to, cross-sections that are able to calculate the thermal deformations and temperature dependent material models for concrete and steel based on EN 2-1-2 (BSI, 2004a) and EN 3-1-2 (BSI, 2005).

4.2.2 Previous implementation of the FBE in OpenSees

The FBE for a 2D analysis was implemented by Volkman in OpenSees (Volkman, 2018). The classes *FireFiberSection* and *FireEl* were developed to implement the FBE formulation. A *FireFiberSection* object was designed to be able to calculate the position of the NA and the *FireEl* class was designed to calculate the tangent stiffness matrix about the RA for a 2D FBE.

The reasons that OpenSees was used to develop the FBE within is that OpenSees is an open source, research-based software which made it easier to implement new routines. Secondly, OpenSees is able to perform non-linear analyses and includes the fibre section and corotational approaches which are used in the FBE formulation. OpenSees provides classes for temperature based materials, thermo-mechanical analysis procedures and thermal-load classes (Volkman, 2018). Furthermore, OpenSees is able to perform thermo-mechanical analysis of 3D structures which makes it ideal to implement the 3D FBE. Therefore, the 3D FBE will also be implemented in OpenSees, building on the work of Volkman.

4.3 Thermo-mechanical analysis in OpenSees

In OpenSees, iterative methods such as the Newton-Raphson or Modified Newton method are available to perform non-linear analyses. These methods are also known as load-control methods, where the analysis consists of loads steps where a constant load is applied at each load step. An iterative process within each load step is followed to obtain equilibrium (McGuire, Gallagher and Ziemian, 2014). For a thermo-mechanical analysis, the deformation caused by the increase in temperature is simulated by including the thermal load in the unbalanced force during the predictor phase (Jiang, 2012).

The iterative process followed for a thermo-mechanical analysis is shown in Figure 4.1. The subscript i of a force or deformation refers to the loadstep, while the subscript j refers to the iteration step during the corrector phase. The functions of an *Element*-object that are called by the analysis to perform the steps are indicated on the left of the diagram. These functions will be discussed in Section 4.4.2. On the right of the diagram the predictor phase and corrector phase are indicated.

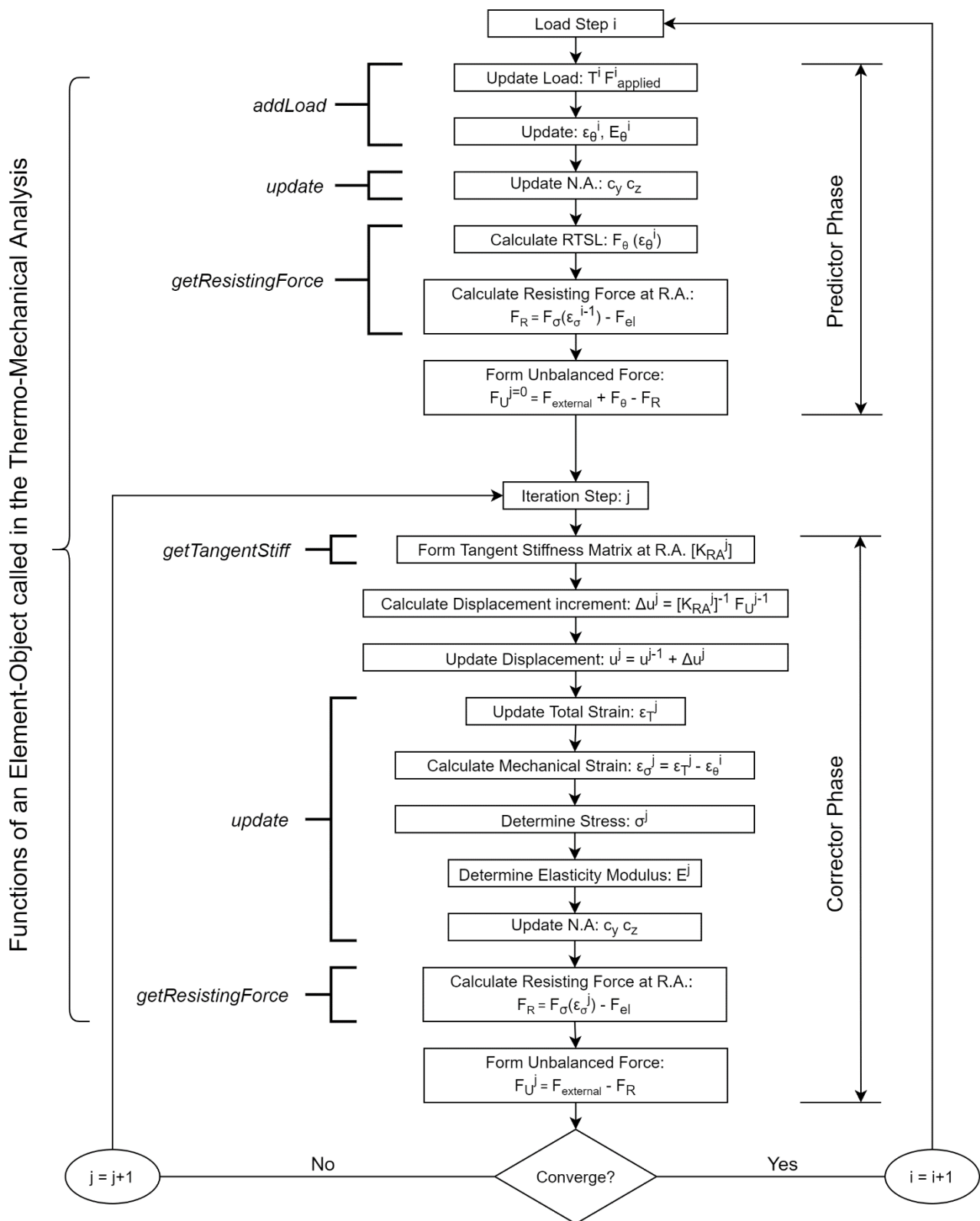


Figure 4.1: A flow diagram illustrating the steps in a thermo-mechanical analysis. The classes required for the thermo-mechanical analysis are shown on the left (adopted from Jiang and Usmani (2013))

Each load step consists of a predictor phase, a corrector phase and a convergence check. The predictor phase determines the initial unbalanced force vector. The unbalanced force vector is the difference between the

external forces applied to the structure and the internal resisting force. The corrector phase is an iterative process, where equilibrium is obtained by incrementing the displacement until equilibrium is reached. After each iteration, the equilibrium of the structure is checked in the convergence check. An overview of these steps is presented below. For more detail regarding the thermo-mechanical analysis refer to Jiang et al (2015).

4.3.1 Predictor phase

In the predictor phase, the applied load, $F_{applied}^i$ and temperatures, T^i , are updated for load step i . The applied loads consist of loads applied to the nodes, $F_{external}$, and the loads applied to the element, F_{el} . The element loads and temperatures are applied to the elements through the *addLoad*-function of each Element-object. Additionally for the FBE, the location of the NA is updated, to account for the change in material stiffness that occurs for the temperature-dependent materials.

Thereafter, the resisting force for each element is calculated by the *getResistance*-function of the Element-object and compiled into the global resisting force of the structure and the unbalanced force, F_U , is calculated for the structure. As introduced above, in the predictor phase, the thermal forces are included in the unbalanced force in order to simulate the deflections caused by the temperature and temperature gradients.

4.3.2 Corrector phase

The corrector-phase is an iterative process, where the total displacements are updated until the external force and resisting force are in equilibrium for the load step, i.e. the unbalanced force tends to zero. In each iteration step, the unbalanced force is used to calculate the amount by which the total displacement should be incremented. The displacement increment is calculated with the global tangent stiffness matrix of the structure, based on the stiffness calculated in the previous iteration step.

After the total displacements are updated, the mechanical strain and stress are calculated for individual cross-sections and used to update the stiffness. For a FBE, an additional step is required to update the location of the NA based on the updated stiffness. The unbalanced force is then calculated, which will be used in the next iteration. Note that for the corrector phase, the thermal force is not included in the unbalanced force, as the displacement increment in the iteration step only depends on the mechanical strain.

4.4 Classes developed in OpenSees for implementing the FBE

OpenSees makes use of a hierarchy structure where the subclasses extend the abstract base classes. Examples of base classes in OpenSees are *Load*, *Element*, *SectionForceDeformation* and *Material*. These base classes define the required attributes and functions which all the subclasses of the function need to implement. This ensures that new subclasses can be implemented and develop the functions in a unique way, without having to change the structure of OpenSees.

OpenSees for fire has subclasses used to analyse structures in a fire. Examples of these are the classes to apply thermal loads (*Beam3dThermalAction*) and temperature dependent material models, (*ConcreteECThermal* and

SteelECThermal classes), where the latter material models are implemented according EN 1993-1-2 (BSI, 2005) and EN 1992-1-2 (BSI, 2004a), respectively. For more detail regarding the classes developed in *OpenSees for fire* refer to Jiang (2012).

The hierarchy of classes implemented in OpenSees to perform thermo-mechanical analyses is illustrated in Figure 4.2. The highlighted classes are the classes that were developed to implement the FBE formulation. For the 3D FBE, the following classes were developed: *FireFiberSectionGJ*, *FireEl3d* and *FireEl3dUni*. The *FireFiberSectionGJ* class represents the cross-section of the element and is used to calculate the section properties, section forces and the position of the NA, while the *FireEl3d* and *FireEl3dUni* classes represent the 3D beam-element. The *FireEl3dUni*-class was developed specifically for the composite beams where only vertical deflection needs to be considered due to the lateral restraint being provided by floor systems, as discussed in Section 3.6.

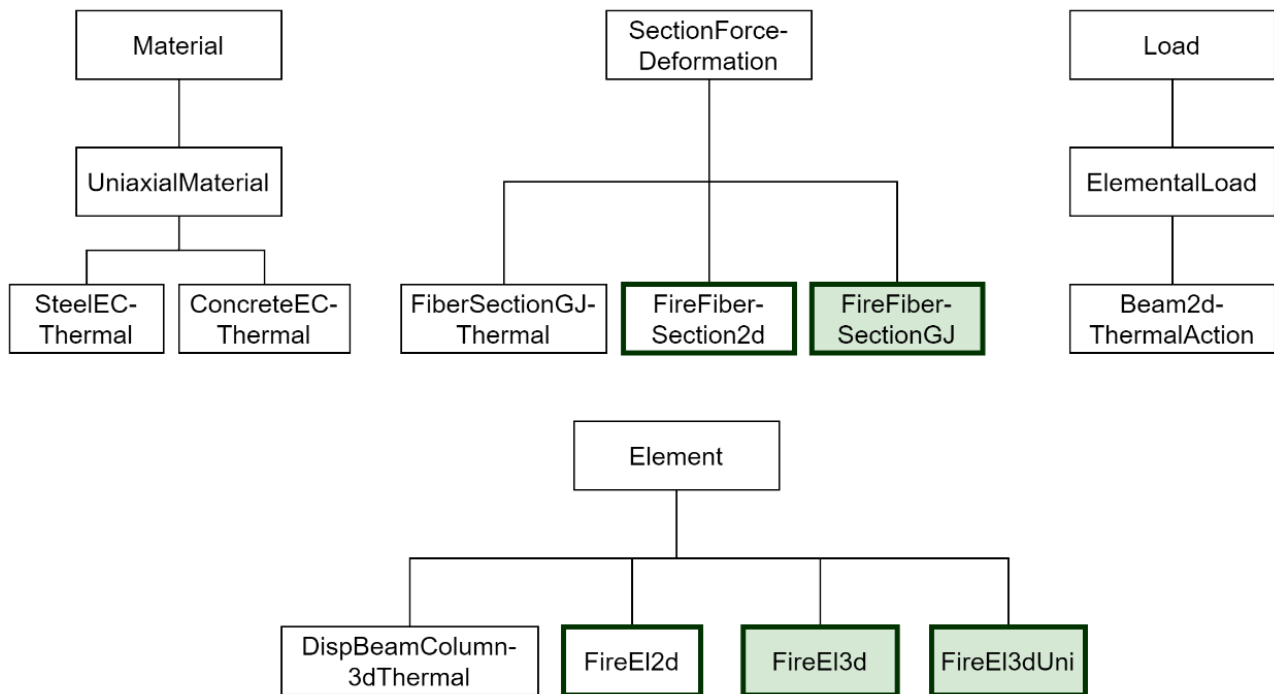


Figure 4.2: Hierarchy of classes implemented in OpenSees for thermo-mechanical analysis (Jiang, 2015) including the class developed for the FBE methodology

4.4.1 *FireFiberSectionGJ*

The *FireFiberSectionGJ*-class was developed to represent the section of a FBE and is a subclass of the abstract class *SectionForceDeformation*. The *FireFiberSectionGJ*-class is based on the *FiberSectionGJ*-class developed by Jiang and Usmani (2013), which uses the fibre section approach to calculate the section properties and forces. The class is able to calculate the following section properties and forces, which were discussed in Chapter 3:

- tangent axial stiffness: EA_T
- the tangent bending stiffnesses: $EI_{z,T}$, $EI_{y,T}$, $EI_{yz,T}$

- the stress resultant: F_σ
- and the thermal load vector: F_θ

Note that currently the *FireFiberSectionGJ*-class does not calculate the torsional stiffness of the section, GJ , in each iteration, but rather a user-defined value is provided. As discussed in Section 3.6 the structures that are considered is not governed by torsion and the torsion effects within the members are negligible.

Another difference between the *FireFiberSectionGJ*-class and the *FiberSectionGJ*-class, is that the *FiberSectionGJ* originally calculates the neutral axes geometrically, thus excluding the stiffness of the materials. Therefore the section properties and forces are calculated about the geometric neutral axes of the section. In the *FireFiberSectionGJ*-class developed in this work, all the section properties and forces are calculated about the RA of the section using the methodologies discussed in Chapter 3. The position of the NA is calculated with a subroutine, as discussed in Section 3.4, by *FireFiberSectionGJ*-class with the additional function, *calculateC*. The stiffness matrix is then updated to account for the NA shift.

Determining the temperature of each fibre: determineFiberTemperature-function

The temperature profile is applied to the beam through the *Beam2dThermal* class, which stores the temperatures at temperature points across the section of the beam element. As shown in Figure 4.2, *Beam2dThermal* is a subclass of *Load* and is applied to an element through the *addLoad*-function of an *Element* class. The temperature points are then passed onto the *FireFiberSectionGJ*-class and the temperature of each fibre is determined with the *determineFiberTemperature*-function.

OpenSees makes provision that either two, five or nine temperature points can be specified over the height of the section. However, Volkmann (2018) identified that 9 temperature points were not sufficient to capture a temperature profile across a composite beam and had to increase the amount of temperature points to 25 over the height in order to achieve sufficient accuracy with the analysis. Therefore, the *FireFiberSectionGJ*-class was also developed to receive 25 temperature points over the height of the section.

The *Beam3dThermalAction*-class in OpenSees has limited capability to specify the temperature profile over the section of a 3D element and can only be applied to an I-beam. Therefore, in this work the *FireFiberSectionGJ*-class was developed only to receive the temperature profile across the height of the section, assuming the temperature to be constant across its width as in the case of a 2D element. This will not have a significant effect on the accuracy of the analysis as the temperature distribution over the width of a concrete slab does not vary significantly. The *determineFiberTemperature*-function can be extended to receive the temperature profile over the height and the width of the cross-section. However, an additional *Beam3DThermalAction*-class would also need to be developed that provides the temperature profile over the height and the width of the whole cross-section, and this would likely require heat transfer analyses.

Calculating the position of the Neutral Axes of the section: *calculateC*-function

The *calculateC*-function calculates and returns the position of the NA with respect to the RA and is called by a *FireEl3d*-object when the NA of the element is being updated. The code for the *calculateC*-function is given in Appendix B.1.1 and is based on the *calculateC*-function for the 2D FBE developed by Volkmann (2018). In order to calculate the position of the NA, the temperature across the height and the number of fibres, *numFibers*, is required, as well as the position and material of each fibre. The temperature across the height of the of the section is obtained through the temperature points that are passed on to the function when it is called, while the number of fibres and their position and material is stored in the *FireFiberSectionGJ*-object. The position of the NA of each cross-section is calculated based on the theory discussed in Section 3.4. The *calculateC*-function is represented by the diagram in Figure 4.3. The overall method to calculate the position of the NA of the 3D FBE is similar to the 2D FBE. However, the section properties for the weak-axis of the section have to be calculated as well.

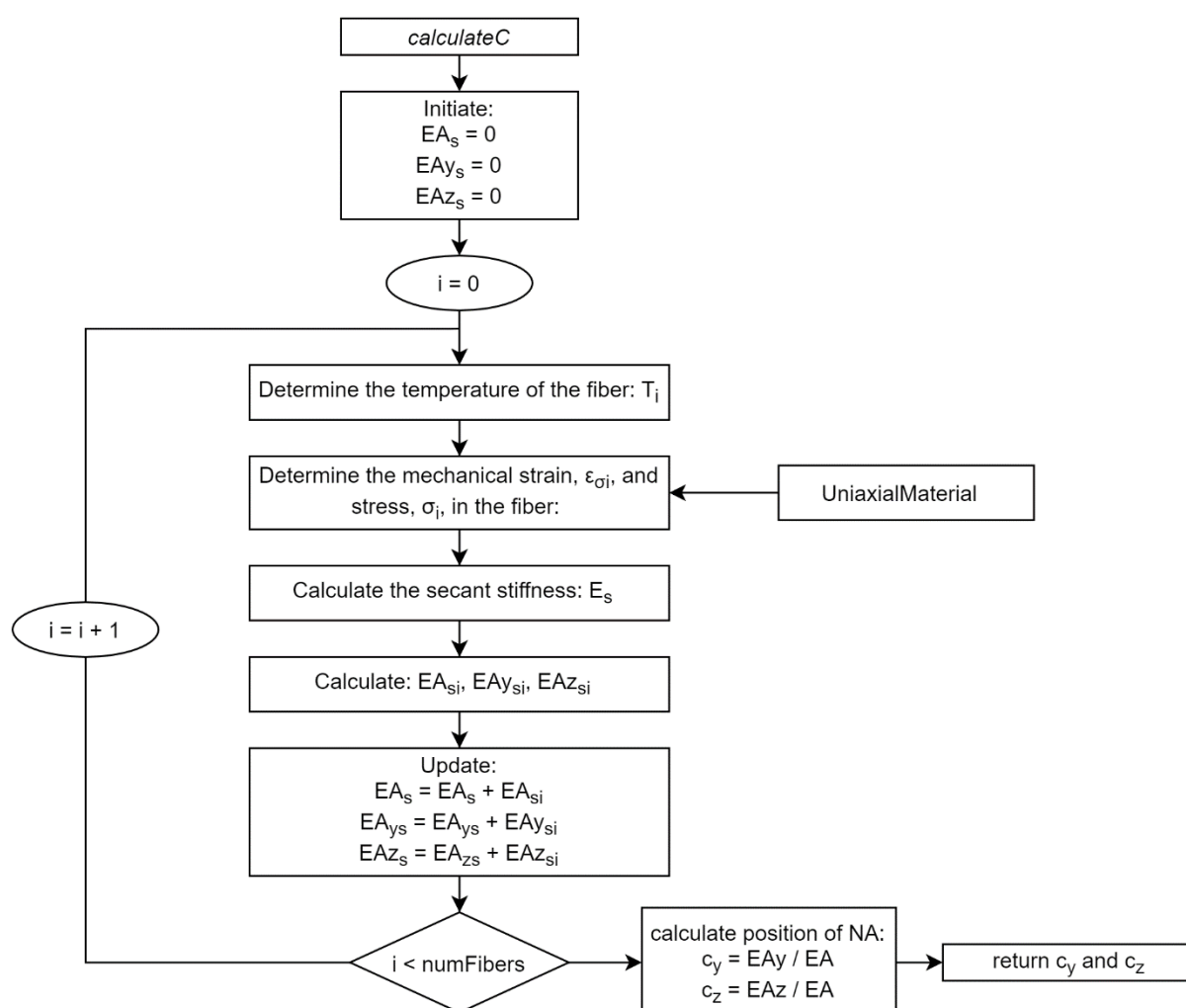


Figure 4.3: The steps followed to calculate the position of the NA in the *calculateC*-function (adopted from Volkmann (2018))

The function iterates through the fibres and sums each fibre secant stiffness, EA_{si} , EAY_{si} and EAZ_{si} , to obtain the total lumped secant stiffness of the section, EA_s , EAY_s and EAZ_s . To obtain the stiffness of each fibre i , the temperature of the fibre, T_i , is determined through interpolating linearly between the temperature points. The mechanical strain and stress of the fibre are determined using the material model of the fibre and a secant stiffness is calculated. After the total lumped stiffness of a section is determined, the position of the NAs are calculated. Note that the secant Young's modulus is used to calculate the position of each NA, as discussed in Section 3.4. The location of each NA is returned by the function as a vector containing the y-component, c_y , and z-component, c_z , of the location of each NA.

4.4.2 FireEl3d

The *FireEl3d*-class has been developed to represent the FBE in a 3D analysis in OpenSees and is a subclass of the abstract class *Element*. *FireEl3d* is based on the *dispBeamColumn3dThermal*-class developed by Jiang and Usmani (2013), which has been modified to include the effect of the eccentric neutral axes. A *FireEl3d*-object is linked to two objects, a *FireFiberSection*-object and a *CorotCrdTransf*-object. In the *FireEl3d*, three basic type of loads are used: the stress resultant, q_σ , the thermal load vector, q_θ and the element load vector, q_0 .

The use of a basic system in OpenSees for beam elements.

OpenSees uses a basic system to calculate the element forces, stiffness matrices and deformation of the beam. A basic system refers to a system in which the rigid body displacement of a beam element is removed by using a local reference frame that rotates with the displaced beam-element. This reference frame is referred to as the basic reference frame. The basic deformation vector, $\{u_b\}$, contains the deformation of the beam element of the element in the basic reference frame. The basic load vector, $\{q\}$, contains the equivalent nodal loads that will cause the deformation of the beam, if the beam were simply supported, as shown in Figure 4.4.

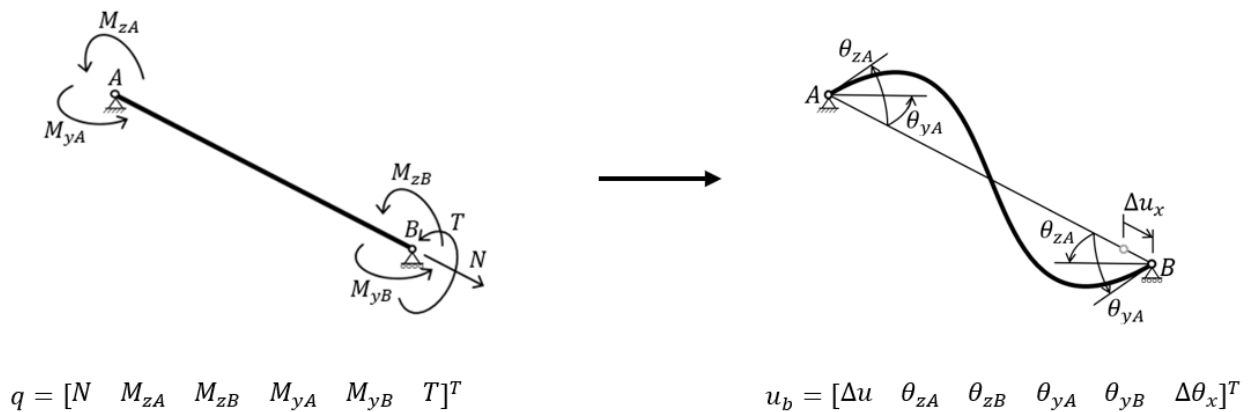


Figure 4.4: The loads (left) and deformation (right) of a beam element in the basic system

The advantage of the basic system for a beam element is that the forces, stiffness matrices and deformation are more compact. For example, the stiffness matrix for a 3D beam element is represented by a 6x6 matrix, instead of a 12x12 matrix. Furthermore, the use of the basic system allows that the material nonlinearity and geometric

nonlinearity be separated. This ensures that OpenSees remains flexible and that different approaches to account for the geometric nonlinearity can be developed and implemented in OpenSees separately from developing the different elements (Scott *et al*, 2008).

OpenSees contains an abstract class *CrdTranf* which is responsible for transforming the load vectors and stiffness matrix of the beam element from the basic coordinate system to the global coordinate system, as well as taking into account the geometric nonlinearity of the element. OpenSees currently provides three types of transformations: *Linear*, *PDelta* and *Corotational*. As discussed in Section 3.5, the corotational approach will be used with the FBE.

Adding a load to the FBE: addLoad-function

The *addLoad*-function is responsible for receiving a load applied to the beam-element and converting it to an equivalent nodal load. The code for the *addLoad*-function is given in Appendix B.2.1. The *addLoad*-function can either receive a mechanical load, such as a uniformly distributed load (UDL) or a point load, or it can receive a thermal beam action. No changes were made to the original code, from Jiang (2012), with regards to the converting of the mechanical loads to equivalent nodal loads. However, the code to convert the thermal beam action had to be adjusted to receive 25 temperature points across the height. Figure 4.5 illustrates the mechanical load and the thermal beam action with their equivalent nodal loads. The methodology converting thermal loads to equivalent forces is discussed in Section 3.3.

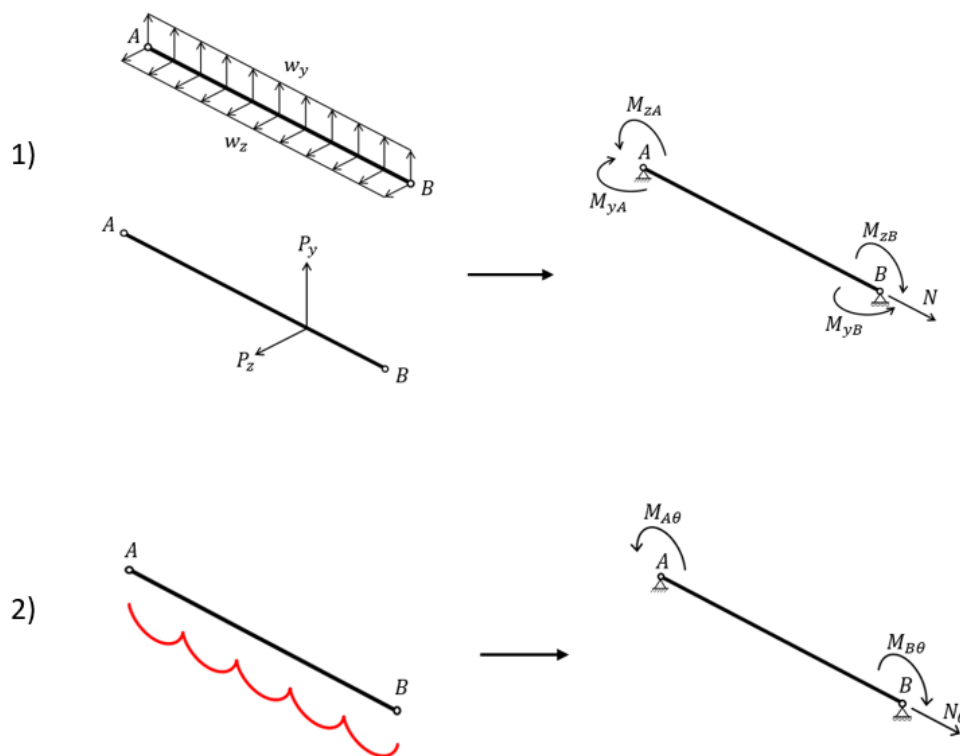


Figure 4.5: The equivalent nodal loads in a basic system representing an UDL, point load or thermal action on the beam element

The mechanical loads are converted to an equivalent nodal load at the NA by calculating the equivalent fixed-end forces for the load in the basic system. The basic load vector representing the applied mechanical loads are given in Equation 4.1 and will be referred to as the element load vector, q_0 . As the position of the NA may vary during the iteration-process in a load step, the element load vector will not be transformed to the RA in the *addLoad*-function, but rather in the *getResistingForce*-function where it is being used. Therefore, the *getResistingForce*-function, which calculates and returns the resisting force at the RA of a beam element, were modified in this work in order to calculate the element load vector about the RA. The basic mechanical load vector is given by:

$$q_0 = [N \quad M_{zA} \quad M_{zB} \quad M_{yA} \quad M_{yB} \quad 0]^T \quad (4.1)$$

The thermal beam actions are given to the beam-element as 25 temperature points across the height of the beam. These temperature points are then provided to the *FireFiberSectionGJ*-object to calculate the Resultant Thermal Strain Load (RTSL) and Moment (RTSM). In the *FireFiberSectionGJ*, the temperature profile over a section is converted to Equivalent Thermal Stresses (ETS) and from the ETS the RTSL and RTSM at the RA of the section is calculated and returned to the beam element. The RTSL, , and RTSM, , is then used to calculate the equivalent nodal loads, as shown in Figure 4.5. The thermal beam action are represented by a basic load vector in Equation 4.2 which is referred to as the thermal load vector, q_θ . These values are calculated as discussed in Section 3.3.

$$q_\theta = [N_\theta \quad M_{A\theta} \quad M_{B\theta} \quad 0 \quad 0 \quad 0]^T \quad (4.2)$$

Updating the deformation of the FBE: update-function

The update-function is responsible for retrieving the deformation of the element from the *CorotCrdTransf*-object and calculating and updating the deformation of the cross-section. The code for the *update*-function is given in Appendix B.2.2. The *CorotCrdTransf*-object returns the basic deformation vector, \mathbf{u}_b , of the beam-element at the RA and the total deformation of the section, $\mathbf{\epsilon}_T$, needs to be updated at the RA. However, the deformations of the section are calculated from the basic deformation vector at the NA. Figure 4.6 shows the steps followed in the update-function required to update the deformation of the section. The highlighted steps indicate the additional steps to account for the eccentric NA. Lastly, the new position of the neutral axis is calculated based on the updated deformation of the section.

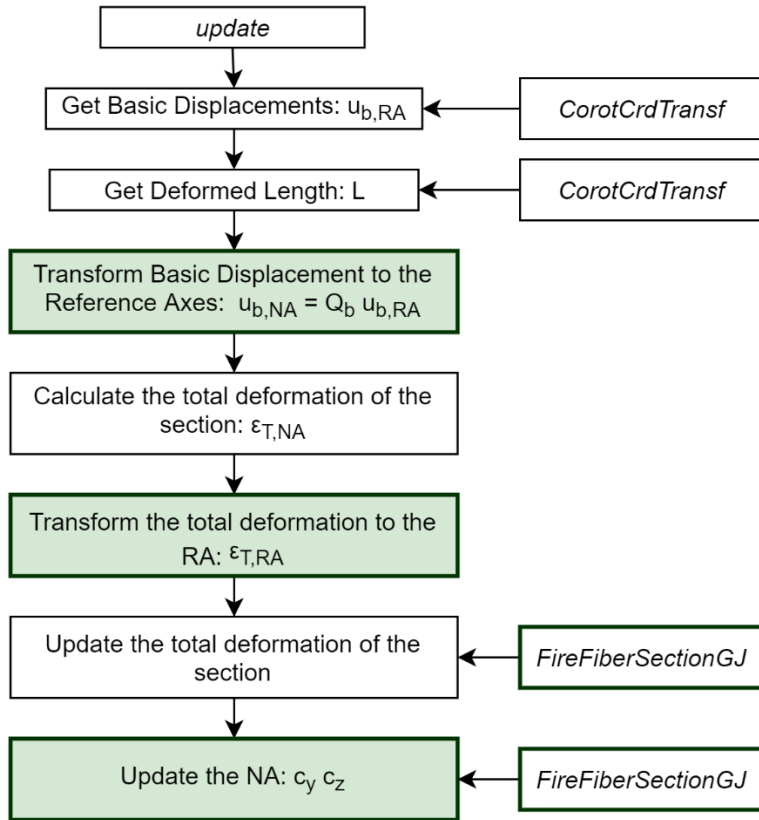


Figure 4.6: A flow diagram illustrating the steps taken to update the deformation of the cross-section of the beam

Compiling the stiffness matrix of the FBE: *getTangentStiff*-function

The purpose of the *getTangentStiff*-function is to compile and return the global stiffness matrix of the FBE. The code for the *getTangentStiff*-function is given in Appendix B.2.3. In Section 3.5, the modified stiffness matrix has been derived for the FBE. However, the transformation of the FBE from the NA to the RA needs to be applied in the basic reference frame. The basic stiffness matrix for a beam-element is defined as follows in OpenSees:

$$k_{el,b,NA} = \frac{1}{L} \begin{bmatrix} EA & 0 & 0 & 0 & 0 & 0 \\ & 4EI_z & 2EI_z & -4EI_{yz} & -2EI_{yz} & 0 \\ & & 4EI_z & -2EI_{yz} & -4EI_{yz} & 0 \\ & & & 4EI_y & 2EI_y & 0 \\ & sym. & & & 4EI_y & 0 \\ & & & & & GJ \end{bmatrix} \quad (4.3)$$

The matrix, \mathbf{Q}_{AB} , has to be adjusted for the basic system. This resulted in the matrix, \mathbf{Q}_b , which is defined in Equation 4.4.

$$Q_b = \begin{bmatrix} 1 & c_y & -c_y & -c_z & c_z & 0 \\ 0 & 1 & 0 & 0 & 0 & \frac{c_z}{L} \\ 0 & 0 & 1 & 0 & 0 & \frac{c_z}{L} \\ 0 & 0 & 0 & 1 & 0 & \frac{c_y}{L} \\ 0 & 0 & 0 & 0 & 1 & \frac{c_y}{L} \\ 0 & 0 & 0 & 0 & 0 & 1 \end{bmatrix} \quad (4.4)$$

Thus, to transform the stiffness matrix of the beam-element from the NA to RA, Equation 3.35 in Section 3.6 can be rewritten in the basic system as follows:

$$[k_{b,RA}] = [Q_b]^T [k_{b,NA}] [Q_{AB}] \quad (4.5)$$

After the elastic stiffness matrix is calculated at the RA, it is passed onto the *corotCrdTransf*-object along with the internal force of the beam element. As mentioned above, the *CorotCrdTransf*-class is responsible for calculating the geometric stiffness matrix and transforming the element stiffness matrix from the basic reference frame to the global reference frame. The process of compiling the stiffness matrix of the FBE is illustrated in Figure 4.7. The highlighted steps indicate the additional steps to account for the eccentric NA of the beam element.

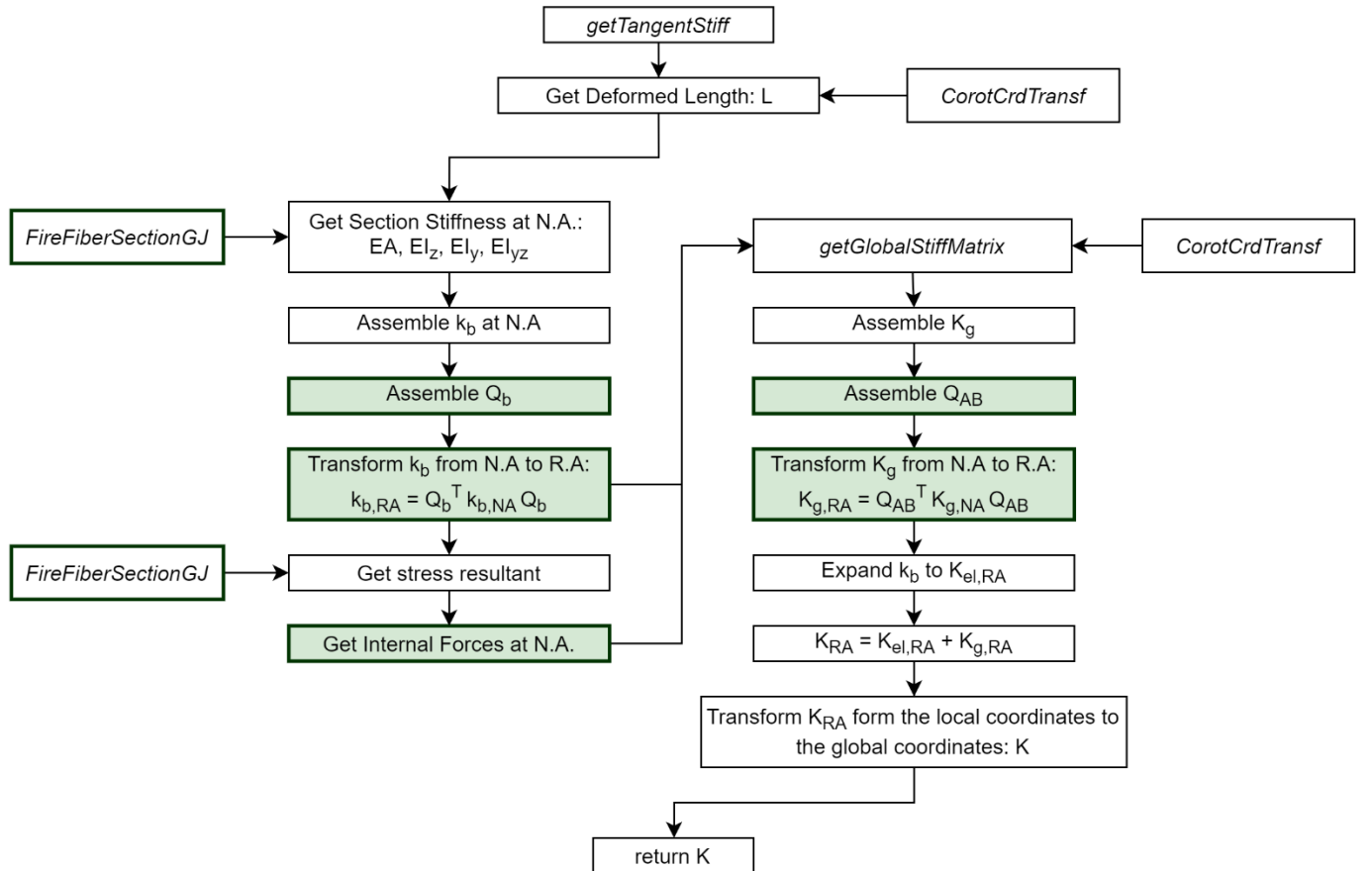


Figure 4.7: A flow diagram illustrating the step followed in order to calculate the global tangent stiffness matrix of the FBE

The *getTangentStiff*-function starts by retrieving the deformed length, from the *CorotTransf*-object, and the section stiffness of the FBE at the NA, from the *FireFiberSectionGJ*-object. Thereafter the basic elastic stiffness matrix is compiled at the NA and then transformed to the RA with Equation 4.5. The *FireFiberSectionGJ*-object is used to calculate the stress resultant, q_σ to calculate the internal forces in the beam element and at the NA.

The basic elastic stiffness matrix and the internal force are given to the *getGlobalStiffMatrix*-function of the *CorotCrdTransf*-object to calculate the global stiffness matrix. In Figure 4.7, the steps followed in the *getGlobalStiffMatrix*-function for calculating the geometric stiffness matrix are included in the diagram. Note that the geometric stiffness matrix is not calculated in the basic system and therefore, the matrix, Q_{AB} , is used to transform the geometric stiffness matrix to the RA.

4.4.3 *FireEl3dUni*

In Section 3.6, it was discussed that the slab will provide lateral support to the composite beams and to account for this in the skeletal model of the structure, a beam element that is rigid about the horizontal axis should be used. Therefore, the *FireEl3dUni*-class has been developed, representing a beam-element that is laterally supported and which can only deflects about its y-axis (i.e. uniaxial bending). The lateral support will be simulated by providing an high stiffness about the z-axis of the beam to prevent the beam from buckling laterally.

The functions in the *FireEl3dUni*-class are the same as the *FireEl3d*-class except that in the *getTangentStiff*-function, a large stiffness about the y-axis is provided, to prevent the beam element from either deforming laterally or from lateral-torsional buckling. In the case studies considered in Chapter 6, the behaviour of the structures considered were not influenced by the magnitude of the stiffness about the weak axis, as long as the beam element did not buckle laterally. Therefore, to ensure that the stiffness about the y-axis is always higher than the stiffness about the z-axis, the stiffness about the y-axis is obtained by multiplying the stiffness about the z-axis at ambient temperature by a factor of ten. This will ensure that the support beams do not buckle laterally. Further research is required to apply this modelling technique to structures with complex geometries.

4.5 The TCL commands in order to call the FBE classes in OpenSees

OpenSees uses a Tool Command Language (TCL) script to provide the input for the analysis. OpenSees contains commands in order to specify the model space, the position of the nodes, the material model, the cross-section, elements types, the boundary conditions and loads, as well as analysis parameters for the non-linear analysis.

Therefore, TCL commands had to be specified so that a user can call the 3D FBE classes when creating a model. The same TCL commands that were developed for the 2D FBE classes by Volkmann (2018) were used for the 3D FBE classes, because the 3D FBE classes can only be accessed in the 3D model space, while the 2D FBE can only be accessed in the 2D model space.

A fibre section can be built up from individual fibres (*fiber*) or a patch of fibres (*patch rect*). The following commands are provided for the *FireFiberSectionGJ* class:

```
section FireFiberSection $secTag -GJ $GJ {
    fiber    $yLoc $zLoc $A $matTag
    patch rect $matTag $numSubdivY $numSubdivZ $yI $zI $yJ $zJ
}
```

where:

\$secTag an - unique number identifying the section
 \$GJ - torsional stiffness of the section
 \$yLoc, \$zLoc - location of the fibre on the y-axis and z-axis
 \$A - area of the fibre
 \$matTag - the unique number of material of the fibre or patch of fibres
 \$numSubdivY - number of fibres of the patch in the Y direction
 \$numSubdivZ - number of fibres of the patch in the Z direction
 \$yI, \$zI - location of the bottom left corner of the patch on the y-axis and z-axis
 \$yJ, \$zJ - location of the top right corner of the patch on the y-axis and z-axis

The following commands were provided for the *FireEl3d* classes:

```
element FireEl      $eleTag $iNode $jNode $numIntegrPts $secTag $transfTa
element FireElUni    $eleTag $iNode $jNode $numIntegrPts $secTag $transfTag
```

where:

\$eleTag a - unique number identifying the element
 \$iNode - number of the first node of the element
 \$jNode - number of the second node of the element
 \$numIntegrPts - number of integration points over the element
 \$secTag - the unique number of the FireFiberSectionGJ of the element
 \$trasfTag - the unique number of the CrdTranf of the element

Note that the number of integration points over the element, *\$numIntegrPts*, is not applicable to the *FireEl3d* classes as the *FireEl3d* classes does not carry out an integration over the element to obtain the stiffness matrices and resisting force. The *FireEl3d* classes only uses the section properties, determined with the *FireFiberSectionGJ*-class, at the start and end of the beam element to calculate the resisting force and tangent stiffness matrices. For the sections stiffness and the axial force of the element, an average of the section properties, at the star and the end nodes, are used.

The remainder of the TCL commands for the thermal classes that are used in *OpenSees for fire* are provided in the *Command manual for OpenSees Thermal* by Jiang (2017).

4.6 Conclusion

In this section the implementation of the FBE formulation for a 3D analysis in OpenSees has been discussed. This implementation builds on the work done implementing the FBE formulation for a 2D analysis in OpenSees. OpenSees was used to implement the FBE formulation as it is an open source software, which made it easier to implement new formulations.

In order to implement the FBE formulation, the *FireFiberSectionGJ*, *FireEl3d* and *FireEl3dUni* classes had to be developed to account for the eccentric NA. These classes were based on the *FiberSectionGJThermal* and *DispBeamColumn3dThermal* classes developed by Jiang and Usmani (2013). An additional method had to implemented in the *FireFiberSectionGJ*-class to calculate the location of the NA. Furthermore, the *FireFiberSectionGJ*-class was developed so that a thermal action could be applied to the section as 25 temperature points over the height of the section. Two classes were developed that represent the element: *FireEl3d* and *FireEl3dUni*. The *FireEl3d*-class represents an element that is able to deflect in both directions, whereas the *FireEl3dUni*-class represent an element that is only able to deflect in one direction (uniaxial bending).

Lastly, the TCL commands were provided to call the classes that were developed for the FBE formulation. These commands for the 3D FBE are the same as for the 2D FBE as the 3D FBE can only be called in the 3D model space, while the 2D FBE can only be called in the 2D model space.

5 Interaction between the FBE analysis and Slab Panel Method

5.1 Introduction

In this chapter, the interaction between the FBE analysis and the Slab Panel Method (SPM) will be discussed. The focus of this chapter is to provide an introduction to the SPM that has been developed in New Zealand by Clifton (2006) for designing steel-concrete composite floors at elevated temperatures. A brief overview of the development of the SPM will be given. Thereafter, the effect that the deflection of the edge support beams have on the SPM will be discussed and an overview of the calculation procedures will be provided.

Lastly, the interaction between the FBE analysis and SPM will be discussed, which includes showing how (a) loads are transferred from the slab panel to the FBE analysis, and (b) the predicted displacements from the FBE analysis are used to update the limiting and maximum deflections required for SPM calculations. Hence, a novel iterative procedure linking the two methods is introduced which will be applied in the next chapter.

5.2 Slab Panel Method

The first edition of the Slab Panel Method was published in 2001 (Clifton, 2001) based on the Bailey-BRE method (Bailey and Moore, 2000a, 2000b). In 2003, the second edition of the SPM was published which incorporated the results of a series of furnace tests on six slab panels. Thereafter, the influence of the deformation of the edge support beams on the behaviour of the slab panel was investigated using models created of the six slab panels of the furnace tests. In 2004, the SPM was also applied to a real floor system and the results were compared to a detailed FE model of the floor system (Clifton, 2011). The third edition of the SPM was published in 2006, which included consideration of the deflection of the support beams based on the fire design time (Clifton, 2006). For a more details regarding the development of the SPM refer to Clifton (2011).

As with the Bailey-BRE method, the SPM divides the floor into slab panels, as indicated in Figure 5.1, and for each slab panel the yieldline load-carrying capacity is determined. Thereafter, tensile membrane action (TMA) is included through an enhancement factor that is multiplied by the yieldline load-carrying capacity to obtain the design load-carrying capacity. However, the SPM has also been extended to account for slab continuity, unprotected secondary beams, additional reinforcement (such as deck trough bars) and incorporates results from additional furnace tests and FEM analyses (Clifton, 2011) in calculating the yieldline capacity and load-carrying capacity of the slab panel. Furthermore, the SPM provides calculations to check that the slab panel provides sufficient shear resistance, that the slab does not fail in compression around the edges and that reinforced steel in the slab is sufficient so that slab panel complies with integrity criteria. Lastly, the SPM provides guidance in designing the support beams of the slab panel.

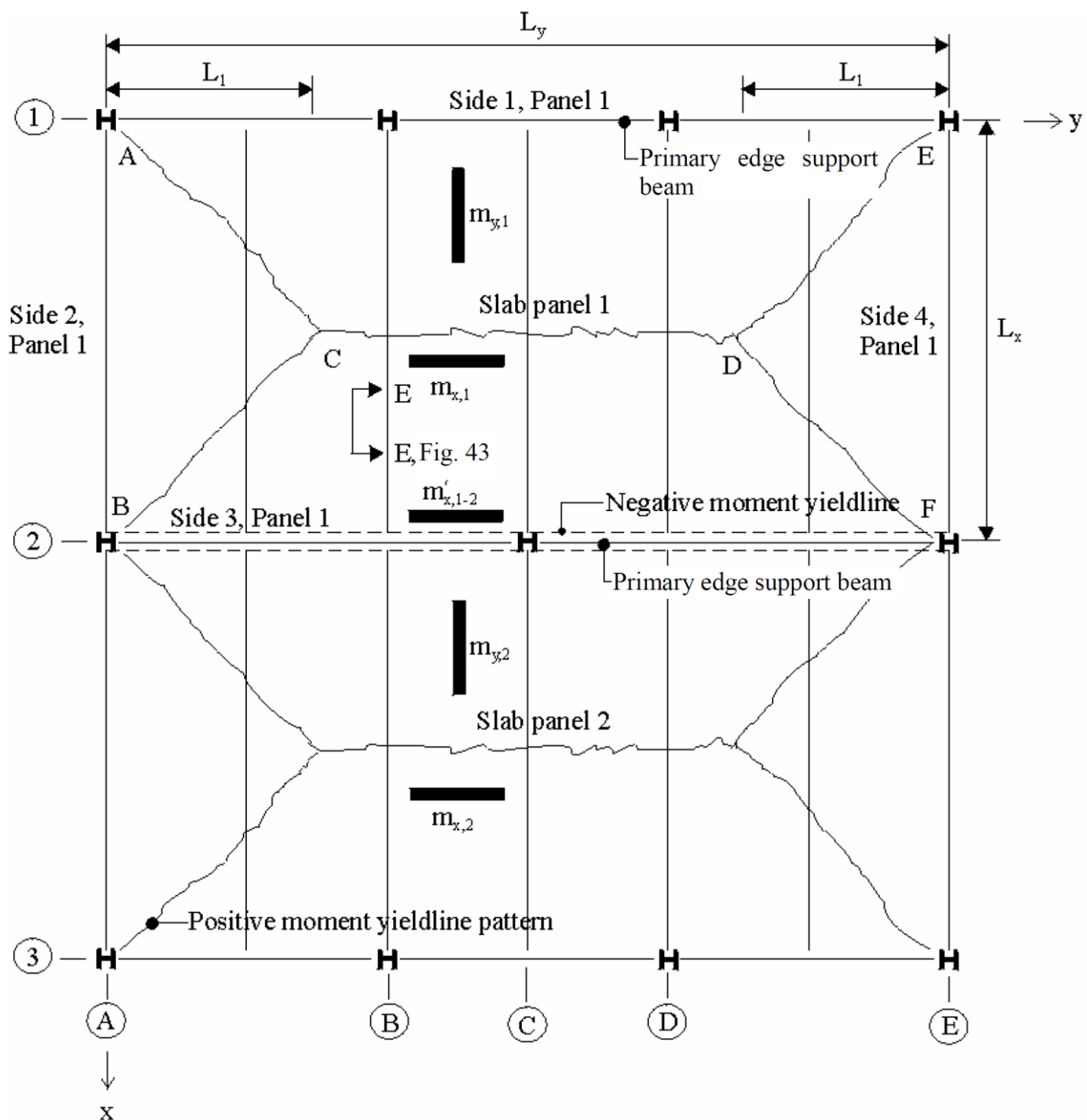


Figure 5.1: Plan view of a composite floor divided into rectangular slab panels (Clifton, 2006)

5.2.1 Effect of edge support beams deflection on the load capacity of the slab panel

The Bailey-BRE method, and consequently the first edition of the SPM, assumed that the slab panels were continuously vertical supported when calculating the design load-carrying capacity of the slab panel. However, studies by Abu and Burgess (2010) and Gu (2016) showed that deflection of the edge supports beams have an impact on the load-carrying capacity of the slab panel.

In the third revision of the SPM, the deflection of the support edge beams were included in the calculation of the maximum deflection of the slab panel. The methodology to calculate the limiting deflection of the slab panel, which is used to determine the enhancement factor due to membrane action, was also modified to account

for the deflection of the edge support beams. The limiting deflection and maximum deflection are given in Equation 5.1 and Equation 5.2 (Clifton, 2006). The limiting deflection refers to the maximum allowable vertical deflection along the yieldline of the slab panel that causes an increase in load-carrying capacity of the slab panel (Clifton, 2006), whereas the maximum deflection is the total vertical midspan deflection due to the deflection of the slab panel and of the support beams.

$$\Delta_{limit} = \left[\min(\Delta_1; \Delta_2) - 0.5 \left(\frac{L_{xb}}{100} + \frac{L_{yb}}{100} \right) \right] C_{ISO} \leq \frac{L_x}{15} \quad (5.1)$$

$$\Delta_{max} = \min(\Delta_1; \Delta_2) C_{ISO} + \min\left(\frac{L_{xb}}{100}; \frac{L_{yb}}{100}\right) \quad (5.2)$$

where $\min(\Delta_1; \Delta_2)$ is the deflection of the slab panel due to the mechanical loads and thermal bowing

L_{xb} is the maximum span in the x-direction

L_{yb} is the minimum span in the y-direction

C_{ISO} is an modification factor accounting for the fire severity

The predicted deflection of the edge support beams was based on results from FEM analyses of the Cardington tests that showed an approximate vertical deflection of span/75 for the edge support beams is realistic. Furthermore, only about 60% to 70% of the deflection of the edge support beams affected the limiting and maximum deflection. Therefore, the effect of the edge support beams was approximated as span/100. The aim of the design methodology presented in this work is to update the deflections that are used in Equation 5.1 and Equation 5.2. This will be discussed further in Section 5.3.2

Large deflections of the edge support beams will also influence the yieldline pattern of the slab panel up to the point where, at the extreme case, plastic hinges in the edge support beams may lead to different failure mechanisms, as shown by Abu and Burgess (2010). These failure mechanisms are discussed in Section 2.4.3. However, the effect of the deflection of the edge support beams is not fully included in the third edition of the SPM, as further research is required to determine the effect on the yieldline patterns of the slab panel. Furthermore, for general deflection magnitudes encountered, the yieldline pattern predicted by the SPM is sufficient as shown in Chapter 6.

5.2.2 Design procedures of the Slab Panel Method

The SPM starts by calculating the fire severity as an equivalent time in relation to the standard fire curve. Thereafter, the design procedures of the SPM can be divided into three main phases: the calculation of the yieldline load-carrying capacity of the slab panel, the calculation of the limiting and maximum deflection of the slab panel and the calculation of the enhancement factor due to the tensile membrane action. A brief overview will be given of each phase. For more detail regarding to the SPM design procedures refer to Clifton and Abu (2006, 2011; 2014) and Lim et al (2012).

Yieldline load-carrying capacity of the slab panel

In order to calculate the load-carrying capacity of the slab panel, the temperature of the reinforcement, concrete and the secondary beams are determined. The calculations to determine these temperatures is based on the standard fire curve. The temperatures are then used to determine the reduced strength of the steel with which the positive moment capacity per unit length is calculated in the x-direction, m_x , and y-direction, m_y , as well as the negative moment capacity, m'_x and m'_y , over the edge support of the slab panel method. The moment capacities are used to calculate the yieldline load-carrying capacity, $w_{yl,\theta}$, of the slab panel.

Limiting and maximum deflection of the slab panel

The limiting deflection, Δ_{lim} , is used in the calculation for the enhancement factor of the slab panel and takes into account the deflection of the slab panel due to the mechanical loads and thermal bowing, as well as the deflection of the edge support beams. The limiting deflection is calculated using Equation 5.1 in Section 5.2.2, while the maximum deflection, Δ_{max} , is calculated using Equation 5.2. These equations will be modified to receive deflections of the edge support from the FBE analysis and will be discussed in Section 5.3.2. The deflections of the slab panel are calculated with Equation 5.3 and 5.4, which are based on the equations proposed by Bailey and Moore (2000b).

$$\Delta_1 = \frac{4.27 \times 10^{-4} L_x^2}{t_0 - \frac{h_{rc}}{2}} + \sqrt{\left(\frac{0.9 f_{yr20,reoL1}}{E_{20,reoL1}} \right) \frac{3 L_y^2}{8}} \quad (5.3)$$

$$\Delta_2 = \frac{4.27 \times 10^{-4} L_x^2}{t_0 - \frac{h_{rc}}{2}} + \frac{L_x}{30} \quad (5.4)$$

where t_0 is the total thickness of the slab
 h_{rc} is the rib height
 $f_{yr20,reoL1}$ is the yield stress of the reinforcement mesh at ambient temperature
 $E_{20,reoL1}$ is the Young's modulus of the reinforcement at ambient temperature

The first term in Equation 5.3 and 5.4 accounts for the deflection of the slab panel due to the thermal bowing. It is based on the peak temperature difference between the exposed and unexposed face of 770°C , which is based on a thermal analysis with natural fire conditions (Clifton, 2001). The second term in Equation 5.3 and 5.4 accounts for the deflection of the slab panel due to the mechanical loads and is based on the maximum deflection that would occur for the average strain in the reinforcement when the slab fails (Bailey, 2001). Therefore, it is important to keep in mind that these equations are not meant to predict the behaviour of the slab panel throughout an analysis, but to predict the deflection of the slab panel at failure as plasticity and large deformations are accounted for.

Enhancement factor due to tensile membrane action

The enhancement factor accounts for the increase in the load-carrying capacity of the slab panel. The first step in calculating the enhancement factor is to determine the yieldline pattern with Equation 5.5. The yieldline pattern is also used to determine the loads on the edge support beams which are applied in the analysis.

$$L_1 = \frac{L_x}{2} \left[\sqrt{\left(\frac{L_x m_y}{L_y m_x} \right)^2 + \frac{3 m_y}{m_x}} - \frac{L_x m_y}{L_y m_x} \right] \leq 0.5 L_y \quad (5.5)$$

The remainder of the calculations for the enhancement factor consist of a series of equations that are relatively easy to apply in a spreadsheet. The calculations are based on initially determining a stress pattern about the yieldline where the steel is assumed to not have yielded. However, the equations have been updated to include the stress pattern where the steel does yield at the corner of the yieldline (Lim et al, 2012).

After the enhancement factor has been determined, it is multiplied by the load-carrying capacity, w_{yld} , of the slab panel to determine the design fire load-carrying capacity, w_u , of the slab panel.

5.2.3 Design guidance for design of the support beams of the slab panel

Additional to the design of the slab panel, the SPM provides simplified design calculations to ensure that the support beams do not distort significantly during the fire. These calculations will be substituted with the FBE analysis which will not only be used to design the support beams, but also provide the support beam deflections which will be used in the design of the slab panel. However, design considerations such as the loads on the support beams and the effective width as prescribed by the SPM will be followed in the FBE/SPM design methodology. The loading of the support beams will be discussed in Section 5.3.1 with regards to the interaction between the SPM and the FBE analysis.

It is recommended by the SPM guidelines that only 60% of the effective width at ambient design is used for the effective width of the concrete slab. This is to account for the effects of the compression ring, that develops due to the Tensile Membrane Action (TMA), which could reduce the contribution of the concrete slab to the strength of the support beam. However, it is noted by Clifton (2006) that there is no clear evidence that the compression ring has a significant impact.

SANS 10162-1 (SABS, 2011a) provided simplified rules for calculating the effective width at ambient temperatures, which are used in this research. The effective width for the edge beams considered are calculated as the sum of the flange width of the steel beam and the minimum of half the clear distance to the next steel beam and span/10. The effective width for an interior beam was calculated as the minimum of the average transverse beam spacing and span/4. The EN 4-1-1 (BSI, 2004b), which provided more detailed calculations for the effective width of the concrete slab, can be used as well. However, the two methods generally yield similar results.

5.3 Interaction between the SPM and FBE analysis

The aim of the design methodology proposed in this work for a full composite structures requires that the SPM and the FBE analyses interact with each other. The FBE analysis requires the loads that will be transferred from the slab panel, which is based on the yieldline pattern determined in the SPM, whereas the deflections determined in the FBE analysis will be used to update the deflection of the support edge beams in order to calculate a more accurate limiting deflection.

5.3.1 Load transfer from the slab to the supporting beams

In the SPM, the loads are directly transferred from the slab panel to the support edge beams. According to the design procedures of the SPM, the loads that are applied to the support edge beams are determined from the loads applied over the tributary area according to the yieldline pattern (Clifton, 2006). Therefore, the loads from the slab panel will be applied to the support beams as illustrated in Figure 5.2.

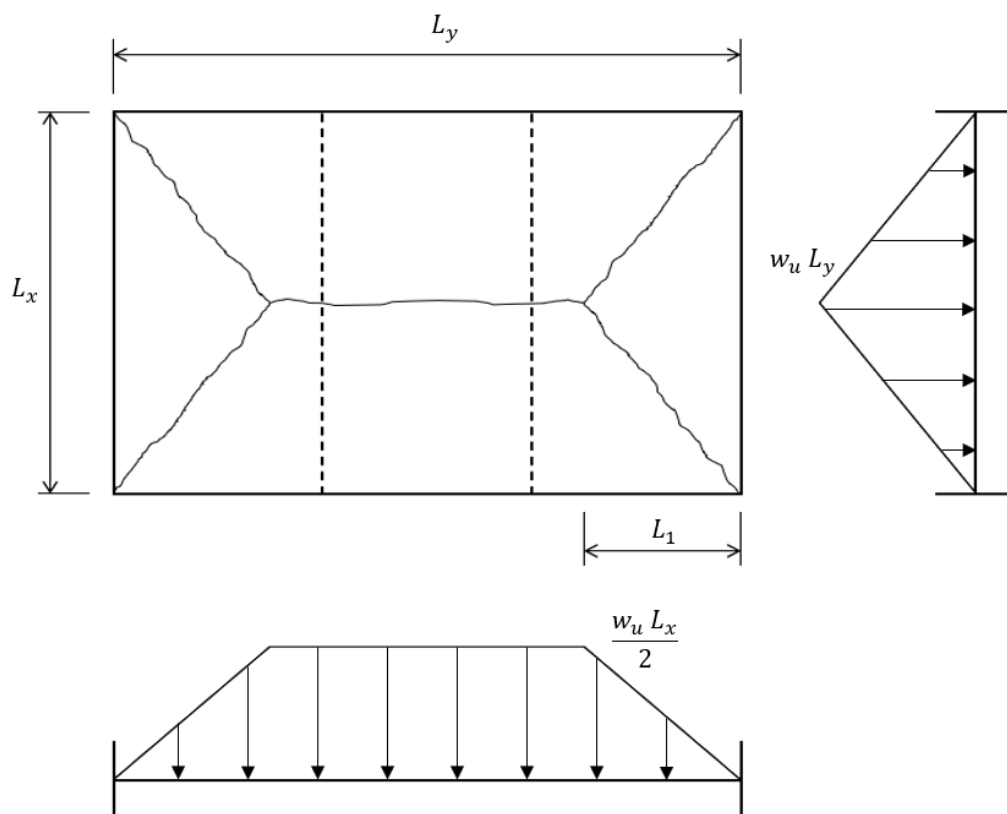


Figure 5.2: Distributed loads transferred from the slab panel to the support edge beams

Thus, the loads on the supporting beams consists of the distributed loads transferred from the slab panels that are adjacent to the support beams and the own weight of the support beams.

5.3.2 Updating of the deflection of the edge support of the slab panel

After the skeletal structure is analysed for the specified fire severity, the maximum deflection for the support beams in the x-direction, $\Delta_{x,spsb}$, and in the y-direction, $\Delta_{y,spsb}$, are determined relative to the displacement of the column as indicated in Figure 5.3.

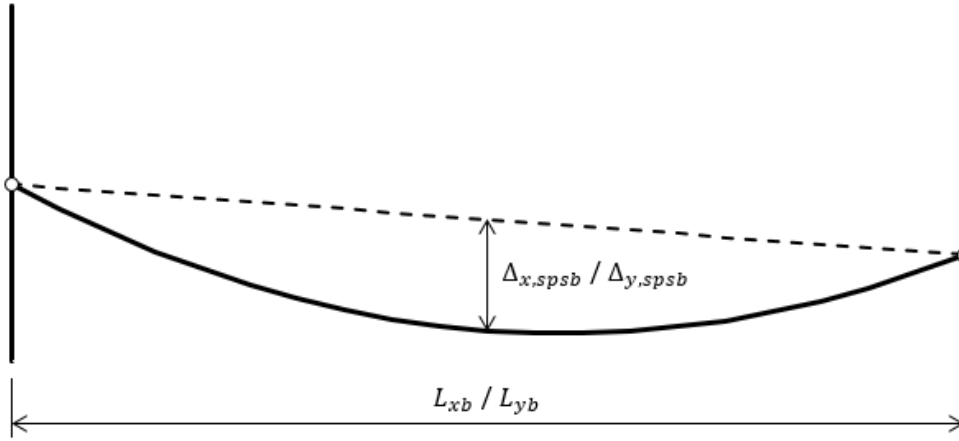


Figure 5.3: Maximum deflection of the support beams relative to the displacement of their supports

In order to link the analysis of the skeletal structure and to update the deflections of the support beams the equation for the limiting and maximum deflection, given in Section 5.2.2, had to be modified for the design methodology proposed here. Thus, the two terms $\frac{L_{xb}}{100}$ and $\frac{L_{yb}}{100}$ were replaced with the maximum deflections calculated by the FBE methodology of the support beams multiplied by a factor of 0.7 which resulted that Equation 5.1 and Equation 5.2 were modified to become Equation 5.6 and Equation 5.7 for the design methodology.

$$\Delta_{limit} = [\min(\Delta_1; \Delta_2) - 0.5 \times 0.7 (\Delta_{x,spsb} + \Delta_{y,spsb})] C_{ISO} \leq \frac{L_x}{15} \quad (5.6)$$

$$\Delta_{max} = \min(\Delta_1; \Delta_2) C_{ISO} + 0.7 \min(\Delta_{x,spsb}; \Delta_{y,spsb}) \quad (5.7)$$

As mentioned in Section 5.2.1, the deflection of the support beams is approximated as span/75 and about 60%-70% contributes to the limiting and maximum deflection, which is subsequently taken as span/100 in Equation 5.1 and 5.2 (i.e. $\frac{span}{75} \times 70\% \approx \frac{span}{100}$). Therefore, in Equation 5.6 and Equation 5.7 the span/100 deflection is replaced with the deflections determined by the FBE analysis multiplied by a factor of 0.7. This is the primary manner in which the FBE updates the SPM predictions.

5.4 Conclusion

In this short chapter the SPM has been introduced and the interaction between the FBE analysis and SPM discussed. The SPM was developed from 2001 onwards based on the Bailey-BRE method. The basis of the SPM is that the yieldline load-carrying capacity is calculated for the slab panel and thereafter the enhancement factor is calculated based on the limiting deflection to account for the increase in load-carrying capacity due to the tensile membrane action. The limiting deflection is based on the deflection of the slab panel and the deflection of the support edge beams. However, the deflection of the support edge beams has been assumed to be $\text{span}/75$ in the SPM, modified by a factor of 70% to account for this contribution to maximum slab deformations.

In this work the SPM is used to determine the yieldline pattern of the slab panel, which is then utilised to determine the loads that will be transferred to each support beam. This load is applied in the FBE analysis to the support beams, along with the own weight of the beams. After the analysis is performed the maximum deflection in the x-direction and y-direction of the support beams is used to update the deflection of $\text{span}/75$ in the calculation of the limiting and maximum deflection. This methodology will now be applied to case studies in the following chapter.

6 Validation

6.1 Introduction

The purpose of this chapter is primarily to validate the FBE analysis and design methodology, but also to highlight the limitations of the methodology. The main focus of the validations is utilising FBE analyses for 3D skeletal structures and comparing the results obtained to experimental and numerical results from different case studies. The SPM is used to determine the loading on the structure in each analysis. In the following chapter the SPM capacity predictions are updated based upon predicted FBE deflections.

Three case studies have been chosen that vary in complexity from: (1) the analysis of a simply supported composite slab panel, to (2) a composite deck with two panels, and finally (3) a sub-structure in a full scale fire test. These case studies were chosen to verify the design methodology in various conditions, as well as to highlight the limitations of the design methodology.

The first case study consists of a benchmark study of composite slab with four columns at its corners which has been developed by University of Sheffield and modelled in Vulcan (COST, 2014). This case study is the simplest case from the three case studies, as it consists of only one slab and therefore no continuity is considered. Only numerical models of the structural system are available. However, it does allow the consideration of full 3D beam-column-panel interactions to be studied and investigate to what extent a simplified skeletal frame can capture the more complex structural behaviour captured by a detailed model in Vulcan.

The second case study is based upon an experiment on a composite slab, referred to as the Second Munich Test, which was conducted by Mensinger et al (2011) and analysed by Stadler (2012). The complexity increases for this case study as continuity of the composite slab has to be considered. Furthermore, temperatures vary throughout the beams and the slab. This slab system has previously been analysed using the FBE methodology by Walls (2016), but only using 2D elements through considering one beam at a time. Hence, this work investigates the extent to which a 2D prediction of a beam may differ from a 3D prediction of behaviour of the full structure.

The last case study is the BRE Corner Compartment Test, which is a full scale test performed on a section of an 8-storey composite structure. The complexity of the structural behaviour considered for the Corner Compartment Test increases significantly as the structure was subjected to a real fire. The slab panels are supported by both unprotected and protected primary beams and the compartment is restrained by the rest of the structure. The corner compartment which were subjected to the fire were modelled as a sub-structure in the FBE analysis and compared to the measured displacement. This case study highlights the extent to which the FBE methodology can capture complex phenomena for some beams, but also scenarios where predictions become less accurate.

6.2 Case Study 1: Composite slab with four columns

Three benchmark studies were performed by Burgess and Alexandrou (COST, 2014) of which two of the studies consisting of a composite slab without columns and the third study consisted of a composite slab with columns at the corner of the slab. The focus of the studies was on the mechanical behaviour of the composite structure. These studies were performed in the software, Vulcan, which was discussed in Section 2.5.3. The beams and the columns are modelled with 3-noded beam elements and the composite slab is modelled with layered shell elements, which are connected to the beam elements with a shear connection.

6.2.1 Model details and modelling considerations

Structure layout

The $6\text{ m} \times 8\text{ m}$ composite slab considered in this case study is supported by four primary beams on its edges, and has one secondary beam along the y-direction at mid-span. The columns, to which the primary beams are connected, have a height of 2 m below the slab and extended 2 m above the slab. The dimensions and layout of the composite slab is given in Figure 6.1.

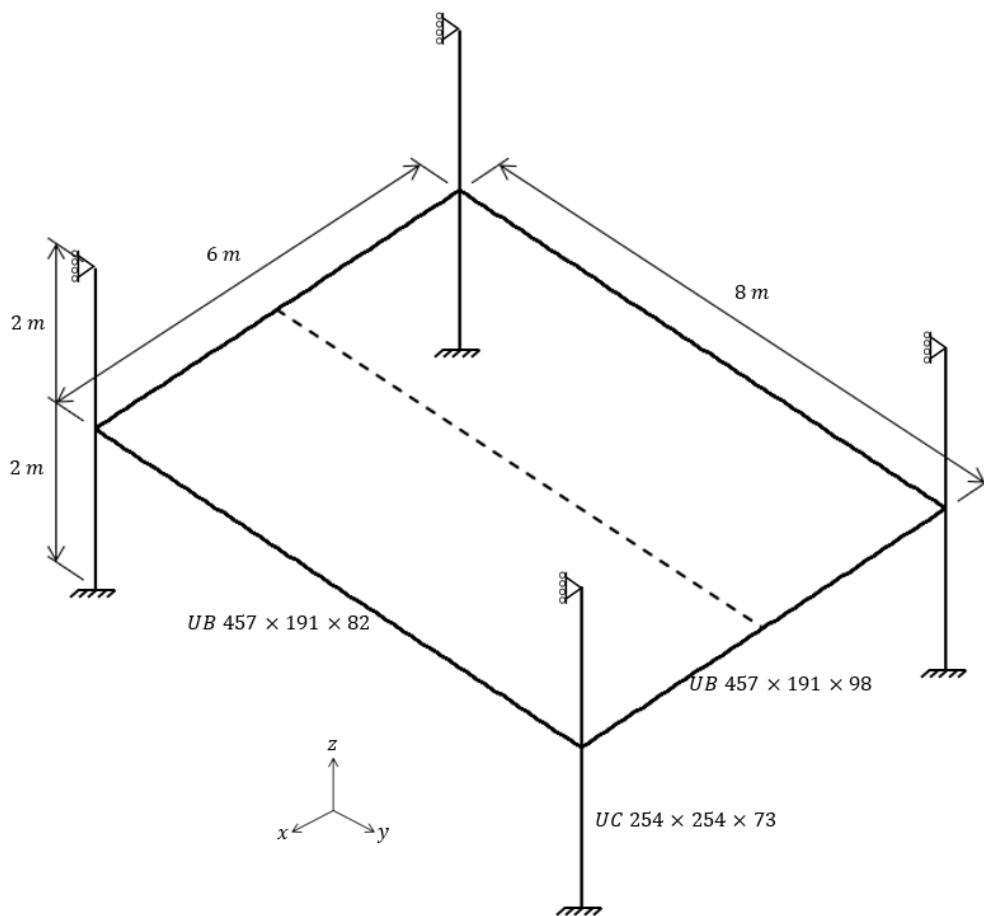


Figure 6.1: Dimensions of the composite slab with columns at its corners (COST, 2014)

Concrete slab details

The composite slab consists of normal weight concrete cast as a flat slab with a total depth, t_0 , of 130 mm. The compressive strength of the concrete is 35 MPa. No information is given with regard to the tensile strength and the elastic modulus of the concrete. Therefore, the tensile strength, f_{ct} , was assumed to be 2.2 MPa and the elastic modulus as 34 GPa, based on Grade 35 concrete from EN 2-1-1 (BSI, 2004a). The slab is reinforced with a mesh of 193 mm²/m area of steel in each direction (i.e. 7 mm bars at 200 mm centres). The position of the reinforcement is not specified and has been assumed to be placed at 45.5 mm from the bottom of the slab. This is based on an assumption of 35 mm cover and the centre of the upper bar layer being considered.

The effective widths of the concrete slab acting with the steel beams at ambient temperature were calculated according to SANS 10162-1 (SABS, 2011a) and multiplied by 0.6 as discussed in Section 5.2.3. The effective width of the support beams in the x-direction and y-direction are 476 mm and 596 mm, respectively.

Steel beam details

The section sizes of the beams in the y-direction and x-direction of the slab are UB 457 × 191 × 82 and UB 457 × 191 × 98, respectively. The columns are UC 254 × 254 × 73 members. The beams and the columns are made from S355 steel which has a yield stress and elastic modulus of 355 MPa and 210 GPa respectively. The connection between the beams and the columns is assumed to be pinned, as it is a simply supported slab panel and no continuity is provided by the concrete. The columns are fully fixed at the base and pinned at the top, allowing the columns to be vertically displaced.

For the FBE analysis, the beams in the x-direction and in the y-direction was discretised into 8 elements and 6 elements, respectively. The columns were discretised into 2 elements each. Therefore, the FBE analysis consisted of total of 36 elements with 44 nodes. In Vulcan, the model consisted of approximately 48 quadrilateral isoparametric elements and 52 quadratic beam elements with 257 nodes. This highlights the significant decrease in computational effort required using the FBE approach.

The cross sections of members were modelled with a fibre section and the slab, the top flange, the web and the bottom flange were discretised into 40 fibres, 4 fibres, 10 fibres and 4 fibres, respectively. As explained in Section 3.3.1, fibres are only considered in subroutines considering cross-sections, and are not present as degrees of freedom in global analyses.

Thermal loading

The temperatures of the slab and the beams were based on the standard fire curve. A simplified temperature profile was assigned to the slab and the beams by the original authors, specifying the temperatures as a fraction of the standard fire curve. The temperature of the bottom flange and web of the protected edge beams are set at 70% of the standard fire temperature and the top flange is at 60%. The temperature of the columns is 70% of the standard fire curve. The temperature within the slab varied linearly from 100% of the standard fire

temperature to 60% at 39 mm from the bottom and 20% at the top of the concrete. The temperature profile used for the composite beams in the analysis is shown in Figure 6.2.

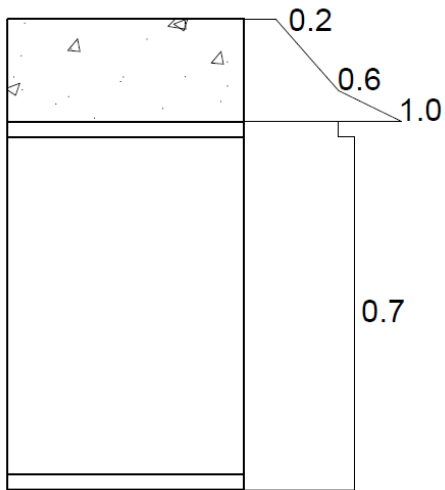


Figure 6.2: Temperature profile, as a factor of the ISO 834 temperatures, of the composite support beams

The temperatures-time curves for each fraction of the Standard Fire Curve is given in Figure 6.3.

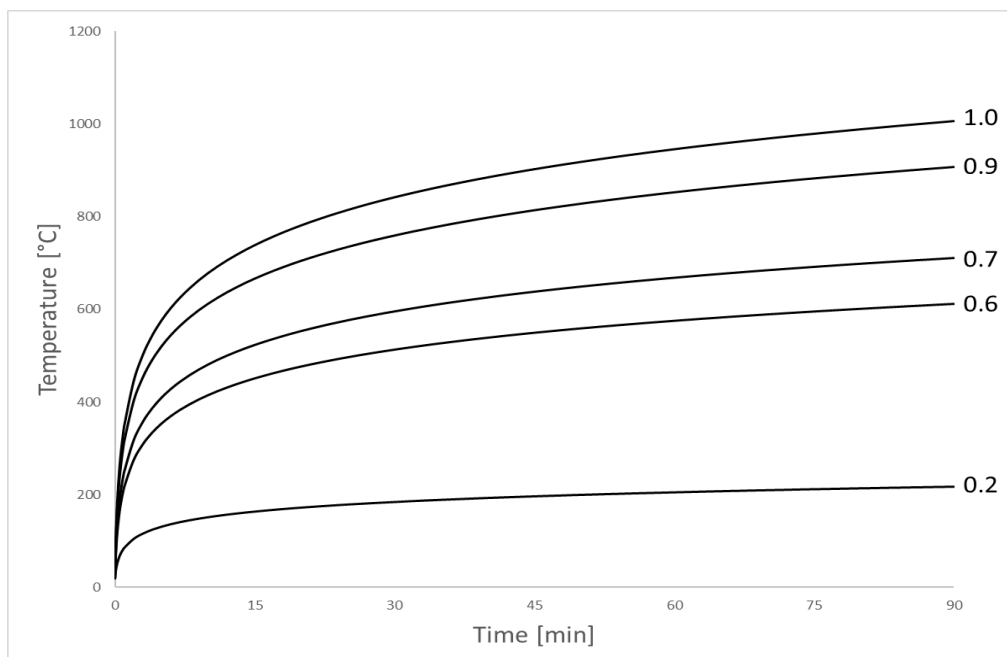


Figure 6.3: Time-temperature curves that would be applied to the steel beams and the concrete slab calculated as a fraction of the Standard Fire Curve (COST, 2014)

Mechanical loading

A uniformly distributed load, w , of 5 kN/m^2 is applied to the slab. This load is transferred to the support beams according to the yieldline pattern determined with the SPM, as discussed in Chapter 5. Figure 6.4 shows the

yieldline pattern for the slab panel determined with the SPM. The maximum load on the support beams in the y-direction is 15 kN/m and in the x-direction is 20 kN/m .

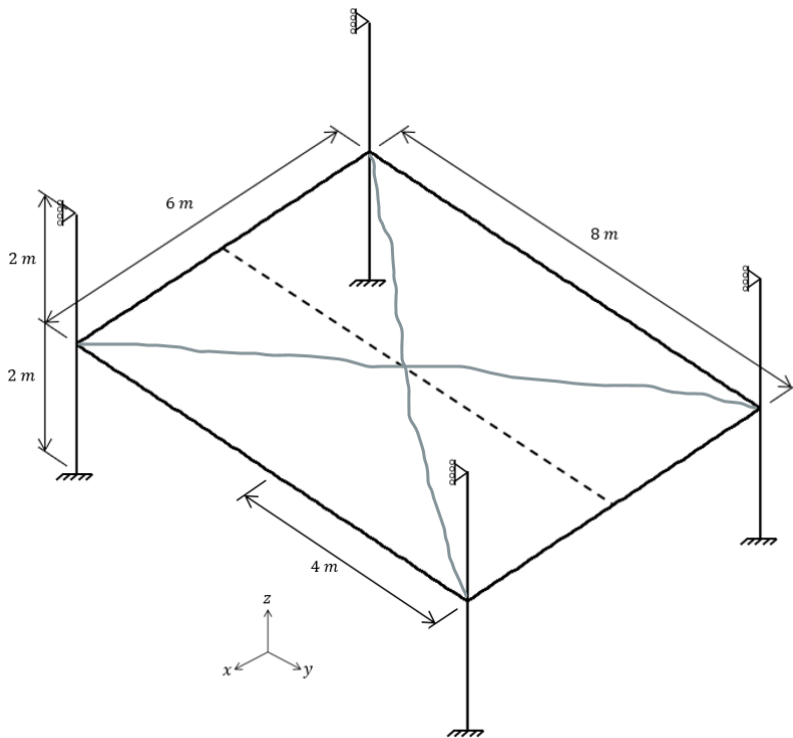


Figure 6.4: Yieldline pattern of the simply supported slab panel determined with the SPM

6.2.2 Results and discussion

The maximum calculated vertical displacements of the edge beams and vertical displacements of the columns obtained using the FBE methodology will now be compared to the results of the Vulcan model, as given in Figure 6.5. The vertical displacements of the beams were measured relative to the displacement of the column. The displacement predicted by the FBE methodology for the columns differs with the Vulcan prediction by 7.8% on average, whereas the displacement of the beams differs by 8.7% and 3.2% on average in the x-direction and the y-direction, respectively. The displacement of the column and the edge beam in the x-direction have a similar behaviour to the Vulcan model, with the FBE approach mostly predicting slightly lower deflections.

As introduced in Section 5.2.1, SPM calculations for determining the capacity of slabs experiencing tensile membrane behaviour are based upon the assumption the primary beams have a deflection of $L_x/75$. Hence, this estimated deflection is also provided in the figure for comparative purposes to show that in the earlier parts of the simulation calculated deflections are significantly lower than this value. At 60 minutes there is approximately a 50% difference in these values. This would lead to less accurate predictions for the SPM procedure for this specific structure, as will be addressed further in the following chapter.

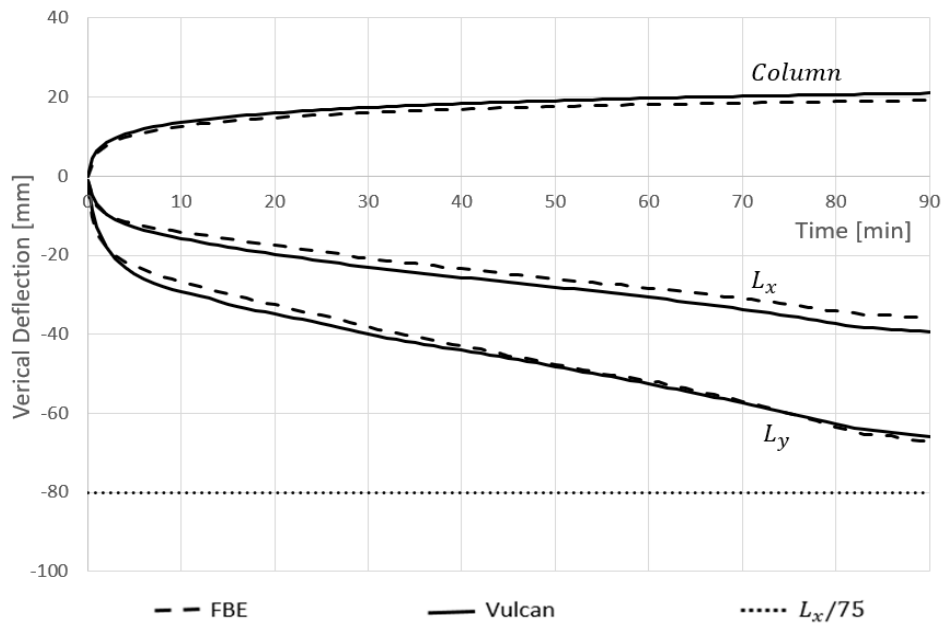


Figure 6.5: Deflection against time for the edge beams and columns, comparing the results of the FBE against Vulcan results (COST, 2014)

Figure 6.6 illustrates the eccentricity of the Neutral Axes (NA) relative to the Reference Axes (RA) at the middle of the edge beam in the y-direction. The RA is modelled at the position of the mid-height of the steel beam. The initial, sudden drop in the eccentricity of the NA is due to the cracking of the concrete which results in the NA migrating downward immediately after the load and fire are applied. Thereafter, the NA begins to migrate upward, as the stiffness of the steel reduces and the top of the concrete provides a higher proportion of the stiffness to the beam.

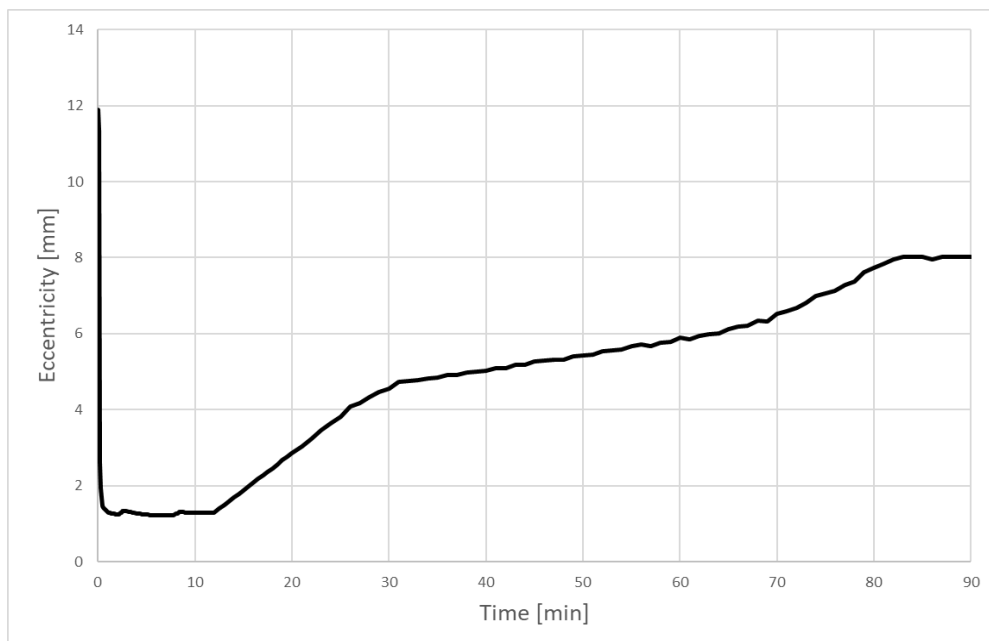


Figure 6.6: Eccentricity of the Neutral Axis relative to the Reference Axis over time for the edge beam in the y-direction

Based on the comparisons above, the ability of the FBE design method to determine the displacement of the edge beams for a simple composite structure is shown with this case study. The displacements determined are typically in good agreement, especially above 60 min, with the Vulcan model and this indicates that the design method is able to capture the behaviour of the edge beams of a simply supported slab by linking the SPM to the FBE analysis. Reasons for the FBE methodology predicting lower deflections may include differing material models employed, tensile membrane behaviour of the floor slab changing load distribution patterns in the Vulcan model slightly, model discretisation and similar factors.

6.3 Case Study 2: Munich Second Test

The Munich fire tests consisted of two full scale tests that were performed within a DAST research project in Germany by Mensinger et al (2011). The purpose of the tests was to investigate the membrane action within the slab panel and a focus of the experiments was the behaviour of the intermediate support beam between two slab panels. The two tests consisted of different flooring systems, secondary beam orientations and fire protection systems. A detailed description of the test are given by Mensinger (2011).

In this research the second test is considered, which is compared to the previous FBE analysis by Walls (2016) and models developed by Stadler (2012). Stadler used a simplified analysis model developed in Abaqus, which employed shell elements to model the slab and beams, which were coupled together with rigid links. A methodology was proposed by Stadler that considered thermal effects through the application of equivalent forces requiring the use of subroutines in Abaqus.

6.3.1 Test setup and modelling considerations

Concrete slab layout and details

The second Munich Test consisted of a composite slab with a Holorib HR51 profile and 0.75 mm thick galvanized sheeting (which will be ignored in analyses due to it rapidly heating up). At the top a Q188 grade S500(A) mesh was provided with 25 mm cover from the top of the slab. At the edge of the slab, $L 120 \times 80 \times 8$ angles were welded to the edge beams to provide formwork to the slab. The composite slab consists of two slab panels that are continuous over the intermediate protected IPE 160 beam: a $7.5\text{ m} \times 5\text{ m}$ panel (left) and a $5\text{ m} \times 5\text{ m}$ panel (right). The layout and details of the composite slab are shown in Figure 6.7. The concrete that was used for the slab was specified as a class C25/30. However, the measured strength of the concrete was 39.4 MPa in compression and 3.59 MPa in tension. The measured modulus of elasticity of the concrete was 36.8 GPa.

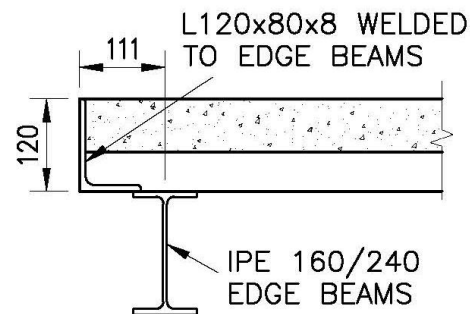
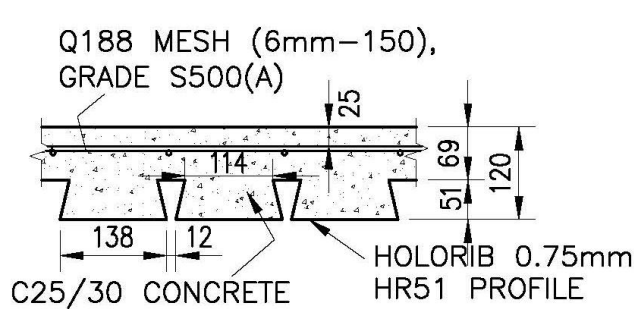
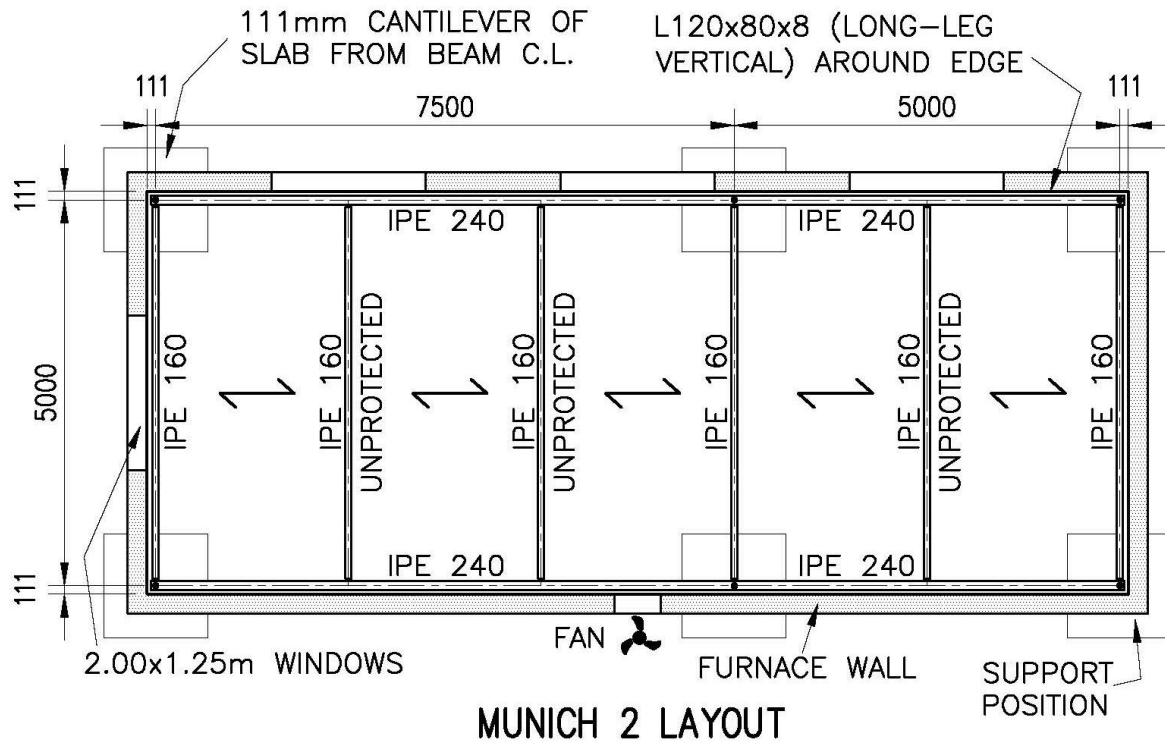


Figure 6.7: The Second Munich Test layout and the details of the composite slab and edge (Walls, 2016)

In the FBE analysis a rectangular concrete slab with an effective thickness was used for including the concrete, as also done by Stadler. The effective thickness for the beams parallel with the span of the slab is 111.8 mm, which was calculated as the effective thickness of an equivalent rectangular area of the concrete slab. The effective thickness for the beams perpendicular to the span of the slab is 69 mm, which is the thickness of the top of the flute of the slab that is continuous throughout the beam. The effective widths of the concrete slab acting compositely with beams were calculated as 60% of the effective width calculated according to SANS 10162-1 (SABS, 2011a) as discussed in Section 5.2.3. The edge beams with a span of the 7.5 m had the effective width of 522 mm, the 5 m span beams had an effective width of 349 mm and the 5 m intermediate beam had an effective width of 750 mm.

The $L\ 120 \times 80 \times 8$ angles that were used as formwork were included in the analysis for the edge beams. It was assumed that the temperature of the concrete is equal to the temperature of the steel at the same depth above

the soffit of the slab, as the temperature profile could only be specified over the height of the cross-section of the beam.

Support beams

The floor was supported by IPE 160 and IPE 240 beams. The measured tensile strength was 315 MPa for the IPE 160 and 329 MPa for the IPE 240. Only the supporting beams were protected with a layer of intumescent paint as specified for a R60 fire resistance, while the secondary beams were left unprotected, as indicated in Figure 6.7. Shear studs were welded to the beams, which were 100 mm long and had a diameter of 16 mm. The spacing of the studs ranged from 150 mm to 300 mm along a single line. Consistent with previous authors, it has been assumed that full composite action is attained. The IPE 240 beams were connected to each other with long fin plate connections and the IPE 160 beams were connected to the IPE 240 beams with end plate connections. The bolts that were used in the connections were M12 and grade 8.8

For the FBE analysis in this work, and previously, only the passively protected beams were modelled as the unprotected secondary beams are considered part of the slab panel, and hence are rather considered by the SPM. The support beams were discretised into beam elements with a length of 0.5 m, resulting in a total of 80 elements. Stadler's model consisted of 1000 shell elements for the deck and approximately 4500 elements for the steel sections. This results in a computational effort approximately 3000 times greater than the FBE approach. The connections between the beams were modelled as pin connections. This is due to the significant rotations could occur with a fin plate connection. Furthermore, the continuity provided by the concrete slab was ignored, as previous analyses of the second Munich Test (Walls, 2016) showed that more accurate results were obtained when the edge beams were modelled as dis-continuous, hence pinned connection are used throughout.

The cross-section of beams were considered using a total of 69 fibres: 4 fibres for the top and bottom flanges each, 10 fibres for the web, 7 fibres for the $L 120 \times 80 \times 8$ angle, 40 fibres for the slab and 4 fibres for the reinforcement mesh. The cross-sectional analysis considering the fibres are carried out through subroutines to determine the properties of the FBE.

Thermal loading and temperature profiles

The furnace for the experiment was constructed with 240 mm thick aerated concrete bricks and the walls were protected with 12.5 mm gypsum boards. The composite slab was placed with a clear height of 3.0 m. On the longitudinal wall, three openings of $2.0 \text{ m} \times 1.25 \text{ m}$ were provided and on the opposite wall a fan was installed to control the ventilation of the furnace.

21 timber cribs, which equated to 33.8 kg/m^2 , were used to provide a fuel load of 548 MJ/m^2 for the furnace. The aim was to follow the ISO 834 standard fire by controlling the ventilations with the fan. However, due to over-ventilation, the ISO 834 standard fire curve was barely reached and at 40 min the maximum of 900°C was recorded. The mean gas temperature and the measured temperatures of the steel are indicated in Figure 6.8. The measured temperatures of the steel beams were applied directly to the steel beams in this work.

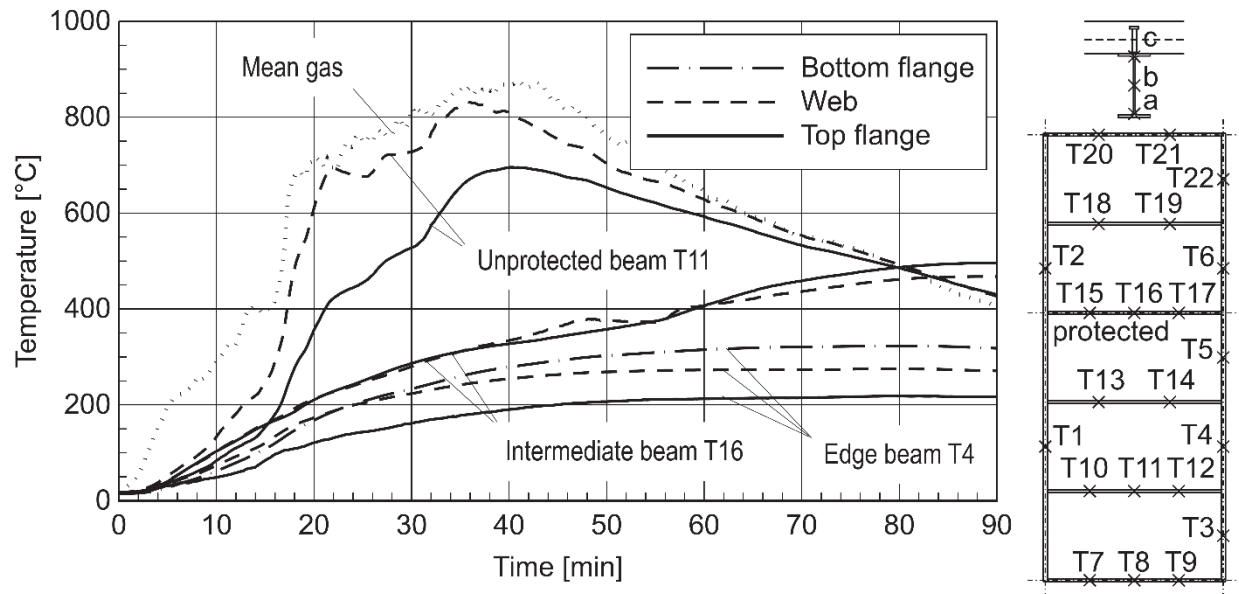


Figure 6.8: Mean gas temperatures and temperatures of the steel beam for the second Munich test (Mensing et al, 2011; Stadler, 2012)

The temperature profile of the concrete was obtained by performing a simple one-dimensional heat transfer calculation for the concrete slab. As an effective height were used for the concrete slab in the FBE analysis, the heat transfer analysis were performed for a concrete slab with an effective height of 111.8 m. The temperatures profile over the height of the concrete slab at 40 min and 90 min were given in Figure 6.9. The temperatures obtained from the heat transfer calculations are provided in Appendix C.

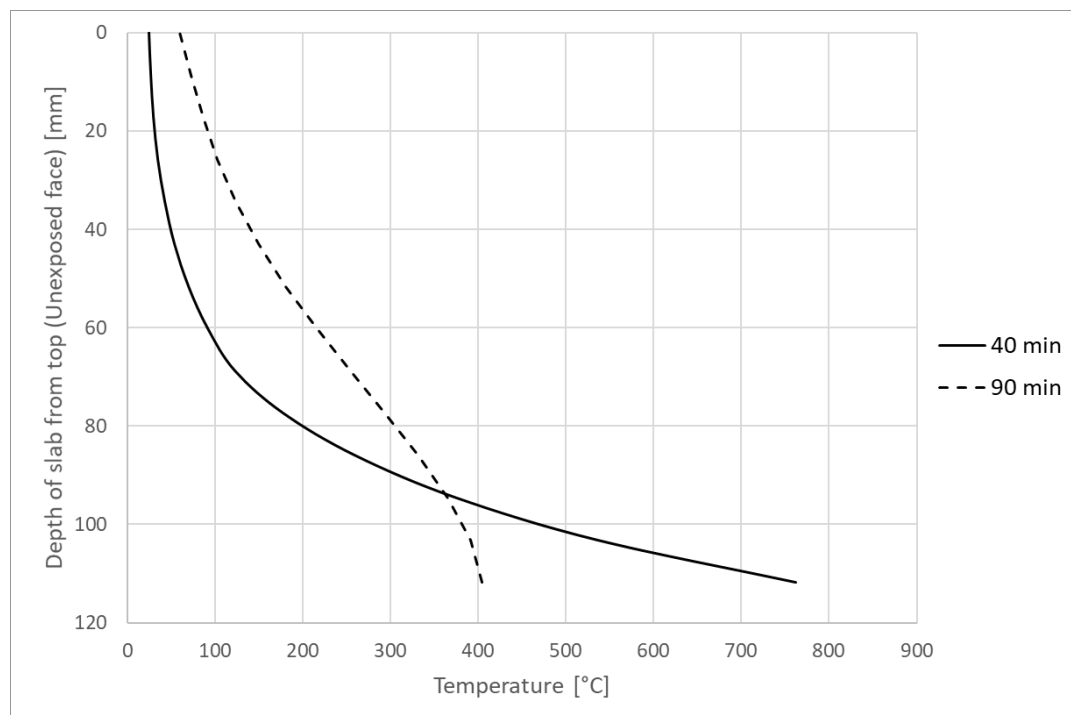


Figure 6.9: Time-temperature curves at different depths of the concrete from the soffit determined with a one-dimensional heat transfer analysis

Mechanical load

On the slab 15 sandbags of 875 kg each were placed to apply a uniformly distributed load of 2.1 kN/m^2 , which is approximately the fire limit state load for an office occupancy according to Eurocode 1991. Including the own weight of the slab the total uniform distributed load applied was 5.1 kN/m^2 . The own weight of the IPE 160 and IPE 240 beams was 0.155 kN/m and 0.301 kN/m , respectively.

The loads from the slab were applied to the support beams based on the yieldline pattern for the slab panels, as discussed in Chapter 5. It was noted that a single crack formed across the whole width of the slab over the intermediate beam at 20 minutes. However, the crack did not lead to structural failure and it appears that continuity of the slab from a load carrying pattern perspective was preserved. Walls (2016) demonstrated that a yieldline pattern that assumes continuity resulted in more accurate results. The yieldline patterns that were calculated for the slab panels were based on simplified ambient temperature plastic analyses and exclude the effect of the secondary beams. It was noted that if the reinforcement had yielded, continuity would have been lost and therefore when designing a structure, different feasible yieldline pattern should be investigated and each beam should be designed for the worst case, especially for complicated layouts. In this research two analyses have been carried out: (1) using a yieldline pattern considering continuity (referred to as 3D FBE below), and (2) using the yieldline pattern calculated according the SPM (referred to as FBE (SPM) below). It was found that the latter predicts significantly lower deflections for the intermediate beams. The yieldline pattern assuming continuity and the yield pattern according to the SPM are illustrated in Figure 6.10.

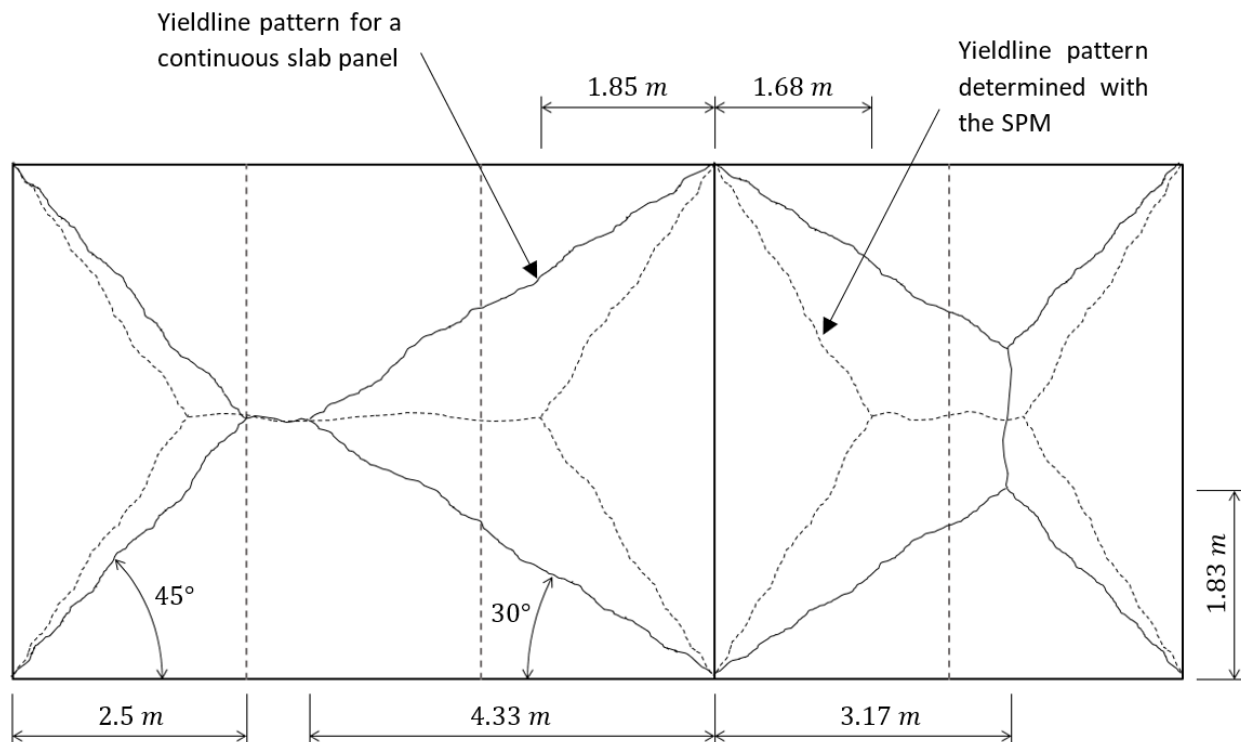


Figure 6.10: Yieldline pattern calculated according to the SPM vs the yieldline pattern assuming continuity at ambient temperature

6.3.2 Results and discussion

Maximum primary beam deflections at 40 min

The vertical displacements of the primary beams obtained from the FBE analysis are compared to the measured displacement of the second Munich test (Stadler, 2012) and previous analyses by Stadler and Walls at 40 minutes in Figure 6.11. Note that only the support beams are modelled with in the FBE analysis and therefore only the deflection of the support beams are predicted. The deflection of the secondary beams predicted by Stadler were included to provide a complete picture.

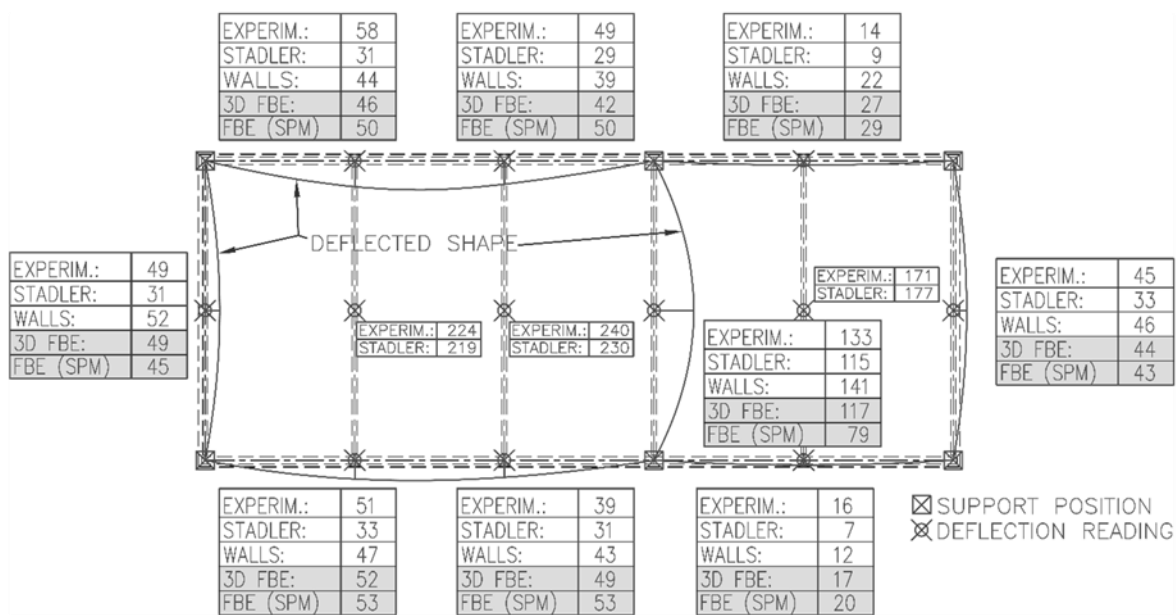


Figure 6.11: Vertical deflection predicted with the FBE analysis compared to the measured displacements and previous analyses of the Second Munich Test (Adopted from Walls (2016))

The displacement obtained from the FBE analyses are typically in good agreement with the measured experimental displacements and the displacements predicted by previous models. In general, the displacements differ by less than 14% from the experimental results. The deflection of the top supporting beam of the $5\text{ m} \times 5\text{ m}$ slab panel is over-predicted by 82%. However, this value is skewed by the fact that the deflection of the support beam was relatively small. The difference in the deflection may be caused by the assumption that the supporting beams are not continuous, which leads to higher deflections being predicted. Also, there are temperature variations along the lengths of beams that are not fully accounted for.

The results obtained in the FBE analysis when the yieldline pattern determined according to the SPM is also included in Figure 6.11. The displacements of the top and bottom supporting beams were slightly over-predicted compared to the previous analysis, but the displacement of the intermediate beam is significant under-predicted at 40% below the measured displacement. This is possibly due to the fact that with the SPM yieldline pattern more load is transferred to the top and bottom beams and significantly less to the intermediate beam, as it does

not account for continuity over the intermediate beam. The influence of failure patterns on predicted results is important to note, and should be considered in future research.

Behaviour of the deflection of the intermediate beam

In Figure 6.12, the behaviour of the intermediate beam predicted by the FBE analysis is compared to the measured displacement of the intermediate beam over time. The deflection of the FBE analysis is based on the yieldline pattern assuming continuity over the intermediate supporting beam. In the previous FBE analysis of this case study the analysis could only be carried out at a specific point in time, whereas in this work the inclusion of the methodology in OpenSees makes analyses across a time domain feasible.

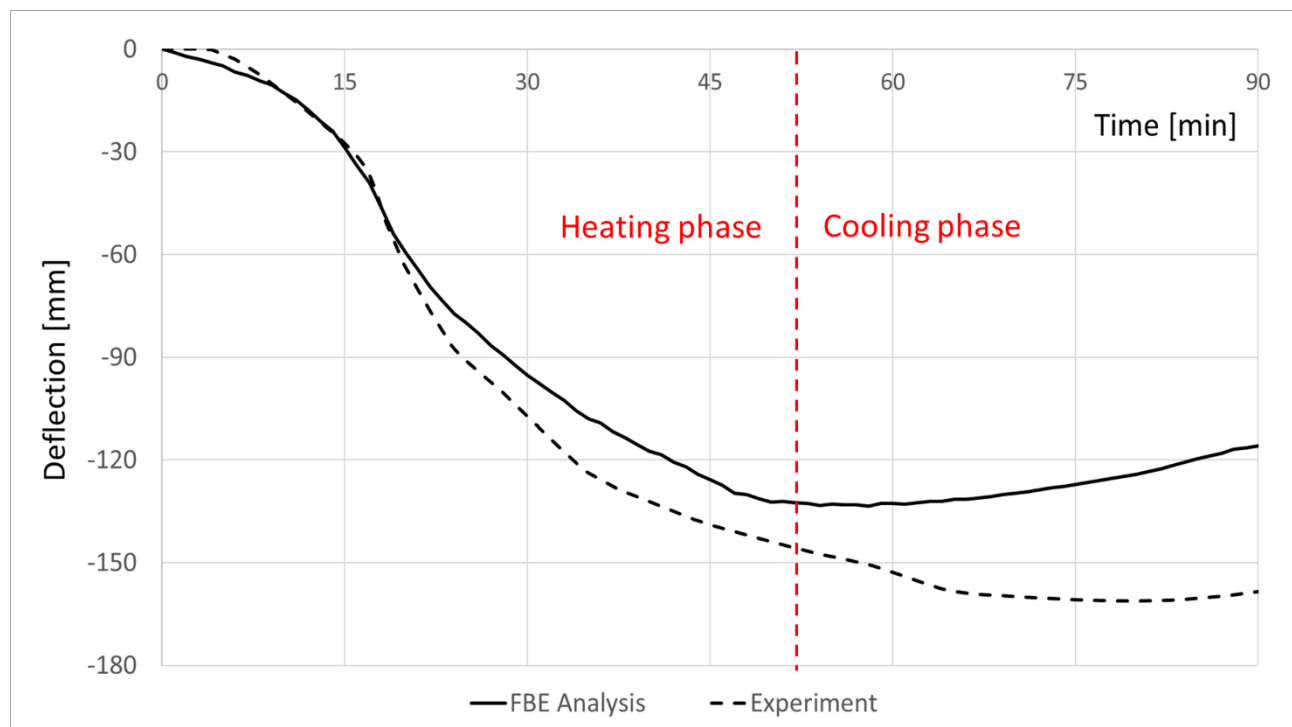


Figure 6.12: Comparison of the displacement at mid-span of the intermediate beam predicted by FBE analysis to the experiment (Stadler, 2012)

From the results it can be seen that the behaviour of the intermediate beam is captured adequately by the FBE analysis during the fire. The FBE analysis under-predicted the displacements by 12 % on average during the heating phase. However, during the cooldown phase, after about 50 min, the behaviour predicted by the FBE analysis diverges from the measured displacement. It is difficult to obtain accurate estimates of concrete and the perimeter steel angle temperatures during the cooling phase which may influence predictions.

6.4 Case 3: Cardington Corner Compartment Test

In 1995, a series of full scale tests were performed on an eight storey composite steel-concrete structure at Cardington. The purpose of the tests was to provide data so that the overall behaviour of the structure could be investigated and understood, especially the membrane action that developed due to large deformations at high

temperature (British Steel plc., 1999). The structure was designed and constructed as a ‘real structure’ to comply with the UK national design codes – BS 5950 (BSI, 2000). Four tests were conducted by British Steel, of which the Corner Compartment Test (Test 3) is used in this work to verify and investigate the FBE analysis. The location of the Corner Compartment Test is indicated in Figure 6.13. The corner compartment is located on the first floor and consisted of a $6\text{ m} \times 9\text{ m}$ slab panel with an area of 76 m^2 (British Steel plc., 1999). Various authors have carried out numerical analyses on the Cardington tests such as Gillie et al (2001), Huang et al (2003) and Sanad (2000). However, the focus of these analysis were the behaviour of the slab and the unprotected beams. The results were included were included if it was applicable.

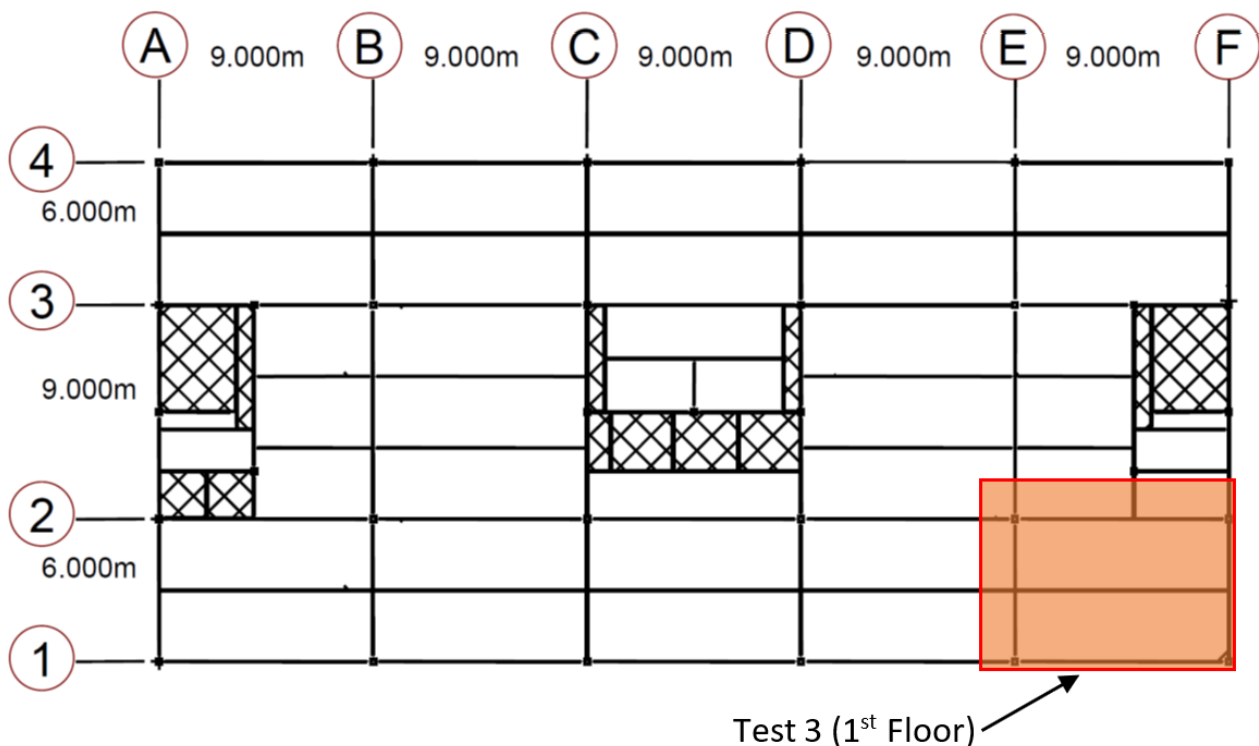


Figure 6.13: Layout of the Cardington structure. The highlighted area indicated the area of the floor subjected to the fire for Corner Compartment Test (Test 3) (adopted from British Steel plc (1999))

6.4.1 Test setup and modelling consideration

Concrete slab layout and details

The composite slab had a trapezoidal profile, and was constructed with a Grade 35 light weight concrete and a 0.9 mm steel deck, PMF CF70, as shown in Figure 6.14. Based on EN 2-1-1 (BSI, 2004) the compression strength were taken as 45 MPa , the tensile strength taken as 2.2 MPa and the Modulus of Elasticity was taken as 34 GPa . The concrete were reinforced with an A142 anti-crack mesh, which had a bar diameter of 6 mm with a spacing of 200 mm . The A142 anti-crack mesh was placed at 55 mm from the top of the slab, and had a yield stress of 460 MPa . The composite slab was connected to the beams with shear studs with a diameter 19 mm and a length of 95 mm .

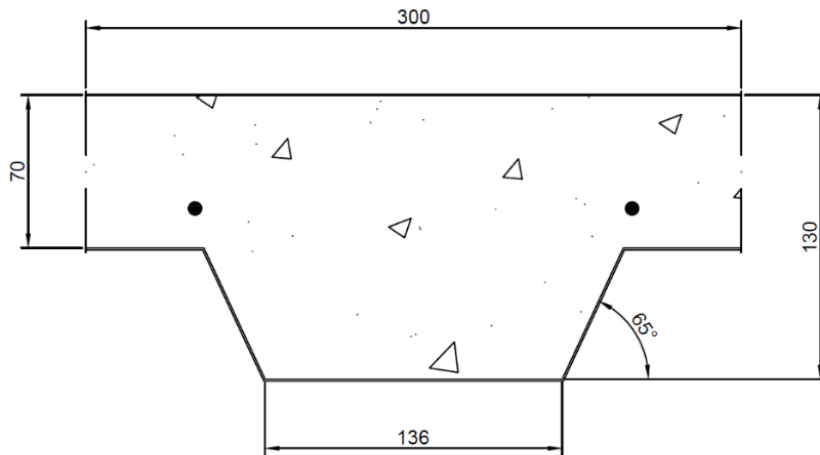


Figure 6.14: The dimensions of the trapezoidal profile of the composite slab (Sanad, 2000)

Support beams and columns

The primary beams and edge beam consisted of a $356 \times 171 \times 51$ UB of Grade S355 steel and the secondary beams consisted of $305 \times 165 \times 40$ UB sections of Grade S275 steel. The columns consisted of $305 \times 305 \times 137$ UC and $254 \times 254 \times 89$ UC sections. The latter were used in the outer corner of the slab panel, while the former were used for the rest of the columns. The yield strength of the Grade S355 steel was 390 MPa and of the Grade S275 steel was 308 MPa and the Modulus of Elasticity was 210 GPa . The beam-to-beam connections consisted of fin plates and the beam-to-column consisted of flexible end-plate connections. As these connections allowed some rotations, they were assumed to behave as pinned connections.

All the edge beams and columns were protected, while all the inner beams, primary and secondary beams were left unprotected. The edge beams and columns were protected with a 25 mm ceramic fibre blanket.

In the FBE analysis, the support beams on Gridline 1 and 2 were discretised into 18 beam elements each and the support beams on Gridline E and F into 12 beam elements each. Each columns was discretised into 2 elements and the beams adjacent to the slab panel were discretised into 3 beam elements each. Therefore, the FBE analysis consisted of total of 85 elements. The cross sections were modelled with a fibre section and the slab, the top flange, the web and the bottom flange were discretised into 40 fibres, 4 fibres, 10 fibres and 4 fibres, respectively.

Thermal loading and temperature profiles

The corner compartment was subject to a natural fire, which was controlled with adjustable ventilation. The compartment was constructed with concrete blockwork. The compartment wall left a 400 mm gap open below the decking to allow deformations to occur, and this gap was covered with a ceramic fibre. An opening factor of 0.031 m^2 was provided which was increased to 0.034 m^2 during the test.

The fuel load provided by was 45 kg/m^2 of timber cribs. This equated to a fire load of about 720 MJ/m^2 . The average measured time-temperature curve of the compartment is given in Figure 6.15.

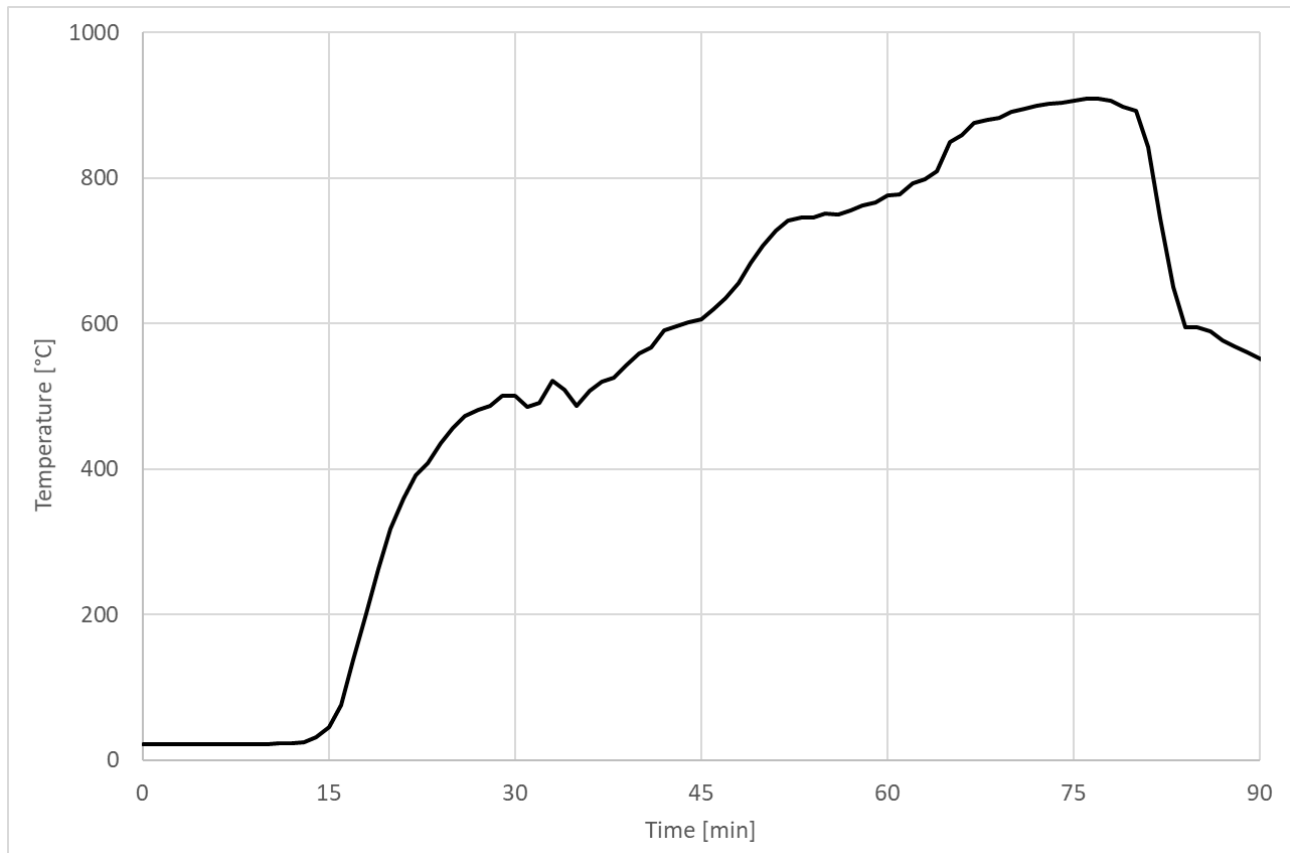


Figure 6.15: Time-temperature curve of the corner compartment subjected to a natural fire

The temperatures in the steel beams were measured extensively and the locations where the temperatures were measured is provided in the literature (British Steel plc., 1999). These temperatures were used to apply temperatures to the steel beams in the FBE analysis. However, for simplicity a constant temperature were provided for the bottom flange, the web and the top flange each. Figure 6.16 is an example of the temperatures applied to the midspan of beam on Gridline 2.

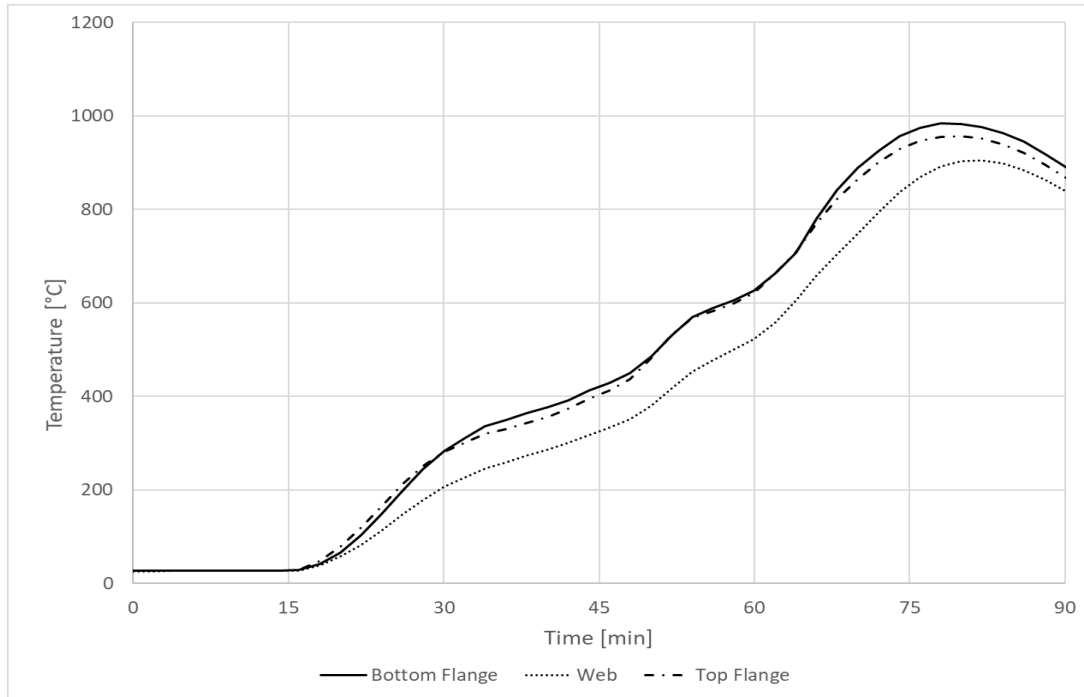


Figure 6.16: Time-temperature curve of the bottom flange, web and top flange of the unprotected steel beam on Gridline 2

To obtain the temperature profile of the concrete slab, a simple one-dimensional heat transfer for the concrete slab with the equivalent thickness of 102.8 mm was carried out. The temperature profile of the concrete slab at 80 min is shown in Figure 6.17 based on the experimental time-temperature curve of the compartment. The temperatures obtained from the heat transfer calculations are provided in Appendix C.

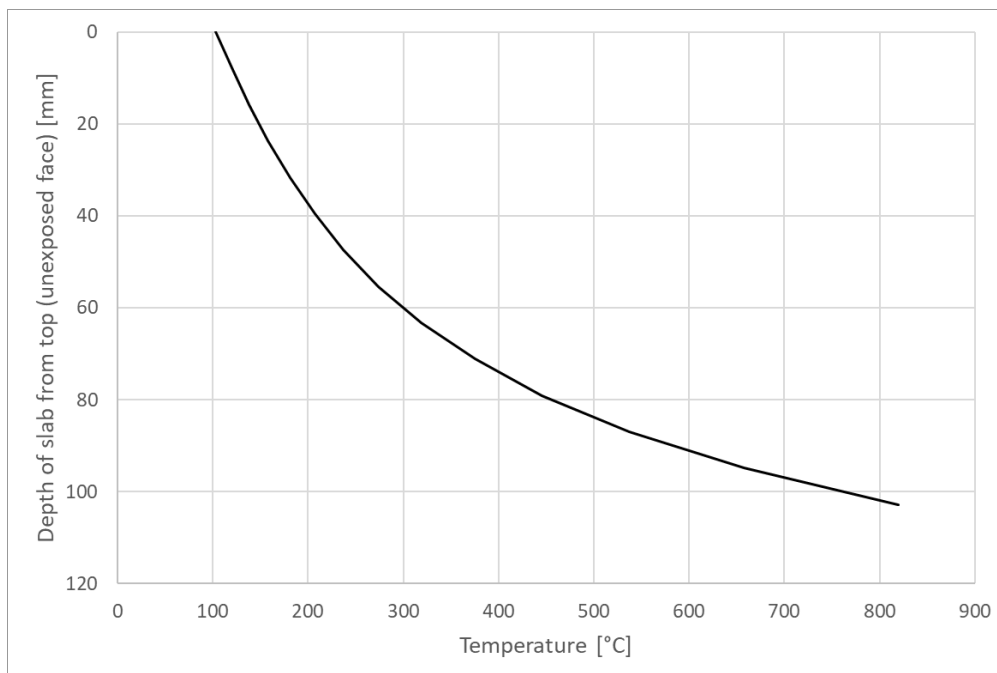


Figure 6.17: Temperature profile of the concrete slab with an equivalent thickness of 102.8 mm at 80 min

Mechanical load

The Cardington structure had a design load of 2.5 kN/m^2 for each floor, except for the roof which had a design load of 7.5 kN/m^2 . The own weight of the floor were reported to be 3.11 kN/m^2 . This included the composite slab, steel sections, raised floor, services, ceiling and the partitions. The imposed load of 0.83 kN/m^2 , which was a third of the design load, was applied through uniformly distributed sandbags which each weighing 11 kN . Therefore, the total load of each floor was 3.94 kN/m^2 . In a structural analysis of the Corner Compartment Test, Gillie et al (2001) included a line load of 19.2 kN/m to take into account the own weight of the compartment walls. This was adopted in the FBE analysis and therefore an additional load of 19.2 kN/m has been applied to support edge beams.

The slab panel adjacent to the corner compartment, which was not significantly affected by the fire, was assumed to transfer the loads as at ambient temperature conditions. Therefore, the loads were modelled as if they would be transferred from the composite slab to the secondary beam and then to the primary beams as illustrated in Figure 6.18. The loads that were applied to the top of the columns are the loads that are transferred from the storeys above the floor. These loads were calculated through considering the loads in the area of the floor that would be supported by the column.

The loads on the composite slab that were subjected to the fire were transferred to the supporting beams according to yieldline pattern determined according to the SPM. The yieldline pattern is indicated in Figure 6.18.

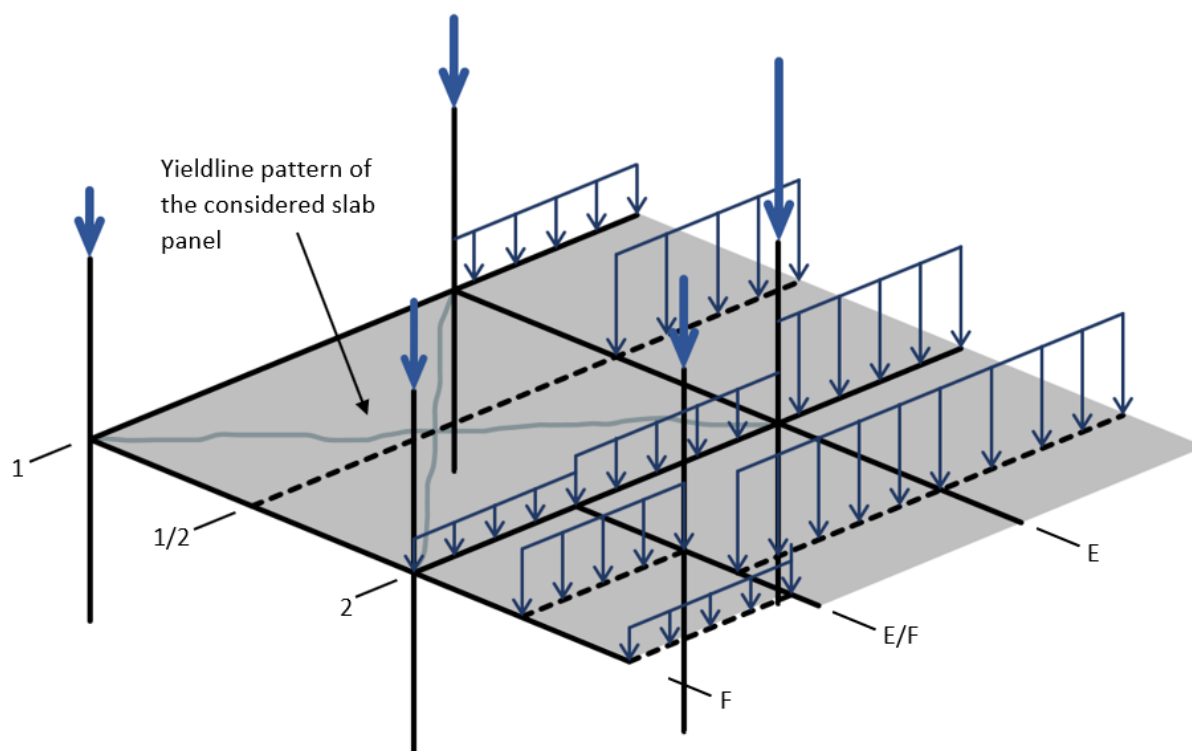


Figure 6.18: Loads applied to the adjacent slab panels that are not subjected to the fire.

6.4.2 Results and discussion

Behaviour of the unprotected support beams

The FBE analysis failed to converge at 55 *min* due to the failure of the unprotected support beams. This differs significant from the test results where the structure did not fail. The lack of convergence is due to the fact that the unprotected beams lost most of their strength after reaching high temperatures: the support beam at Gridline E reached a temperature of 917°C and the beam at Gridline 2 reached a temperature of 984 °C. Therefore, the “primary” beams becomes supported by the slab as for the case of the secondary beams, which are considered part of the slab panel. Figure 6.19 shows the behaviour and failure of the support beam at Gridline E predicted by the FBE analysis compared to the measured displacement. The results obtained by Gillie et al (2001) and Sanad (2000) are included in Figure 6.19 as well. Note that thsesse results were presented as displacement against the temperature of the bottom flange in the original work and had to be processed in order to compare them to the results of the FBE Analysis.

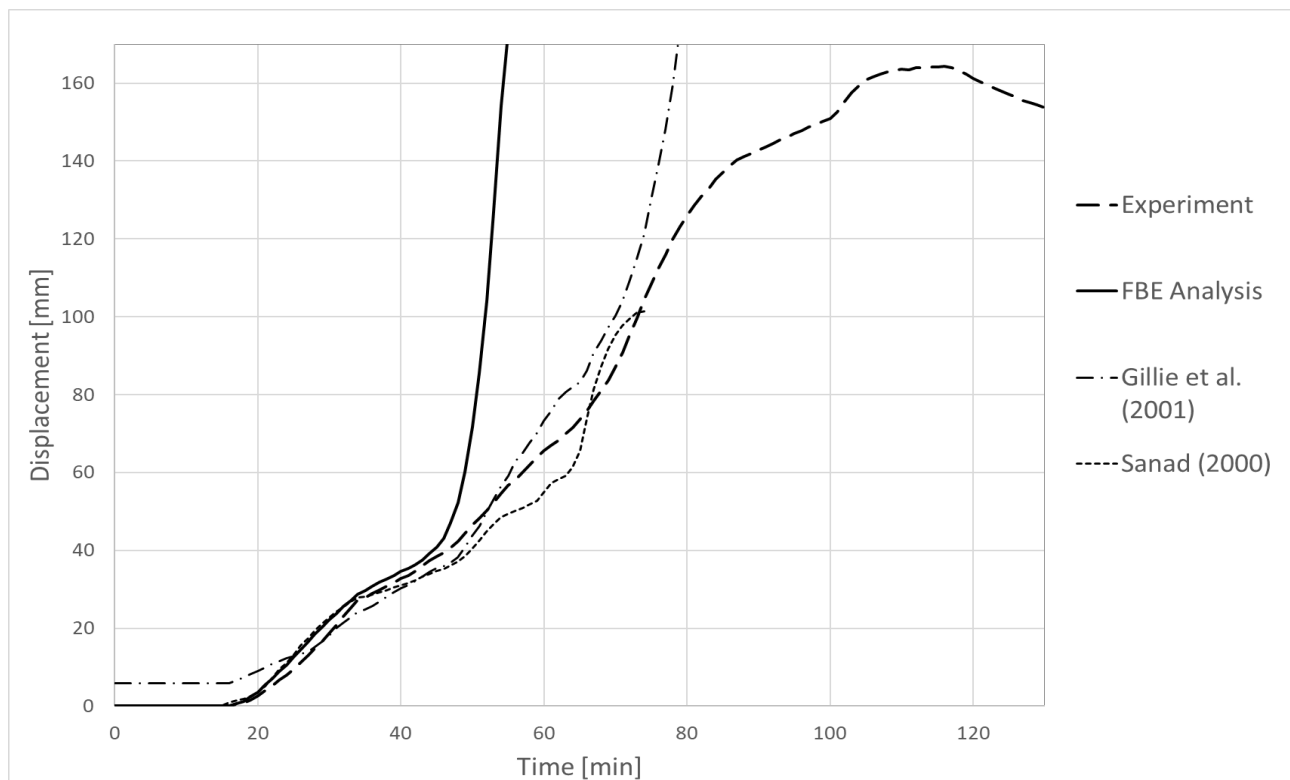


Figure 6.19: The predicted displacement of the support beam at Gridline E by the FBE Analysis compared to the measured displacement and previous analyses of the Cardington Corner Test

Gillie et al (2001) have modelled the Corner Compartment with 8-noded shell elements and 2-noded beam elements and Sanad (2000) used a grillage model to the behaviour of the slab. Although these two models were able to capture the behaviour of the support beam to a greater extent than the FBE analysis, they also failed to capture the true behaviour of the support beam after it has lost its strength. Taking into account that these

models require more computational effort than the FBE analysis, the FBE analysis compares well to the results obtained by Gillie et al (2001) and Sanad (2000).

However, the results above highlight the limitation of the design methodology in cases where the support beams lose significant strength due to reaching high temperatures, and components not modelled provide significant additional load carrying capacity. The temperature of the web of the beam at 55 *min* was 625°C which would imply that only around 15% of the strength of the steel remained. However, it should be noted that FBE analysis predicted the behaviour of the beam up to 45 *min* accurately. Since the FBE methodology has been developed for skeletal frames where it assumed that Euler-Bernoulli assumptions apply, cases where primary beams experience tensile membrane behaviour should not be considered, and this is an important limitation which is highlighted by this case study.

A possible solution for the situation where the strength of the “support” beams reduces significantly and is unable to support the slab panel, is to choose a different size for the design panel. For example, the slab panel could be extended to the edge of the compartment that are affected by the fire. Thus, the slab panel will be vertically supported by the protected edge beams and by the rest of the adjacent slab that are not subjected to the fire. However, the FBE methodology would not be able to model and analyse the behaviour of the edge of the slab panel that is supported by the adjacent slab that is not subjected to the fire. Therefore, further research will be required to investigate the behaviour of the edge of the slab panel that is supported by the adjacent slab that is not subjected to a fire. Nevertheless, such complicated behaviour is outside that which would typically be considered in normal structural fire design procedures.

Behaviour of the protected support beams

The maximum temperature reached in the protected edge beams was 395°C at Gridline 1 and 374°C for the beam at Gridline F, and these did not fail. The support beam at Gridline F reached a predicted maximum displacement of 24 *mm*, while the maximum measured displacement was 19 *mm*. The support beam at Gridline 1 reached a maximum displacement of 102 *mm* according to the FBE analysis, while the maximum displacement measured was 97 *mm*. Figure 6.20 compares the behaviour of the support beam at Gridline 1 predicted by the FBE analysis compared to the measured displacements. The displacement were under-predicted by 4 *mm* on average, with a maximum difference of 8 *mm*. In this case the FBE analysis captures the behaviour of the beam up to 82 *min* very well. However, thereafter the rate of change of displacement of the test reduces, which is not captured by the FBE analysis. This probably occurred due to the structure starting to cool down, leading to a variety of complex structural interactions and temperature profiles which are not fully captured. Nevertheless, overall results are in good agreement. It should also be noted that the temperature in the protected edge beams would still be increasing, while the slab and the rest of the structure would started to cool down, which would contribute to the complex interactions, which are not captured with FBE analysis.

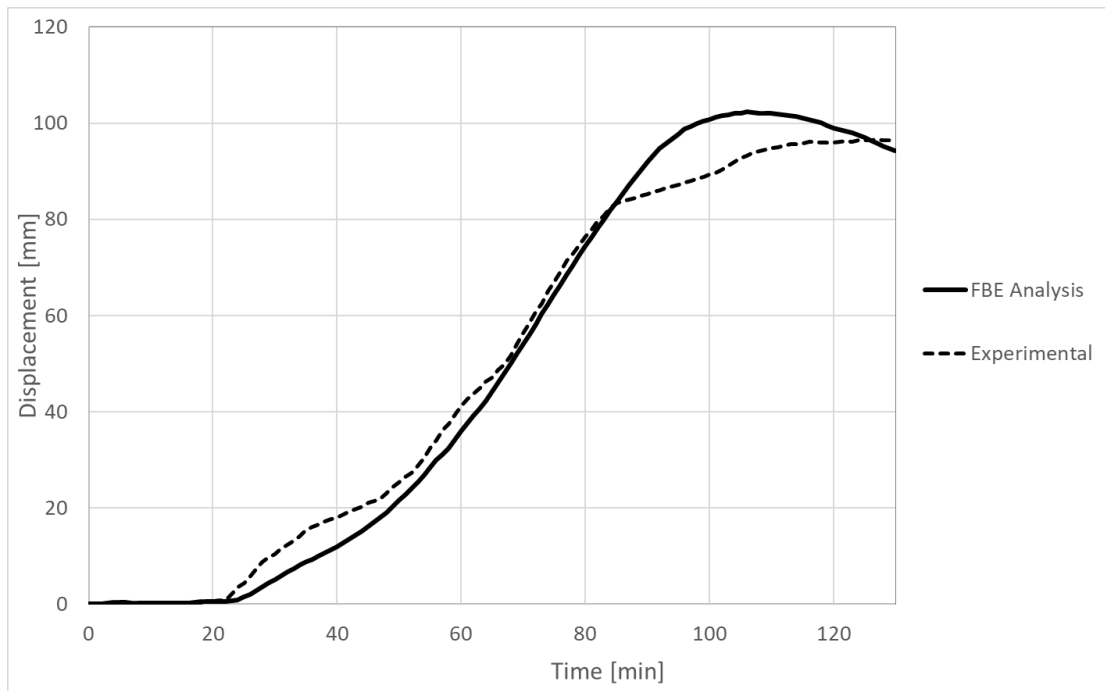


Figure 6.20: The predicted displacement of the support beam at Gridline 1 by the FBE Analysis compared to the measured displacement of the Cardington Corner Test

6.5 Conclusion

In this chapter, the design methodology proposed has been validated with three case studies that vary in complexity. The focus of the validation is the FBE analysis of the supporting skeletal structure with the use of the SPM to determine the loading on the support structure. Thus, the yieldline pattern determined by the SPM was validated indirectly (but also showed limitations where continuity was not considered in the second case study). The three case studies that were considered were a benchmark study of a single composite slab with four columns, the Second Munich Test and the Cardington Corner Compartment Test. The computational effort of the FBE approach was shown to be significantly lower than models used to analyse the same case studies.

The first case study was a benchmark study of a composite slab supported by protected beams on its edge and four columns on the corners of the slab panel, which was modelled in Vulcan. The behaviour predicted by the FBE analysis compared well to the Vulcan model. The deflection of the short span (x-direction) differed by 7.44% and the long span (y-direction) by 5.73%. The displacements were slightly under-predicted by the FBE analysis. This case study indicated that the 3D FBE is a suitable beam element to model the beam-column-panel interaction in conjunction with the SPM.

The second case study consisted of the Second Munich Test which was conducted by Mensinger et al (2011) and analysed by Stadler (2012). The results obtained from the FBE analysis compared well to the measured experiments and previous analyses. Two yieldline patterns were considered in the FBE analysis, the yieldline pattern determined by the SPM and a yieldline pattern determined at ambient temperature taking into account the continuity of the slab panel. The case study indicated that the continuity has a significant impact on the

loading on the intermediate beam over which the slab panel was continuous. This indicates that it is necessary for the continuity of the slab panel to be taken into account in the yieldline pattern and the loading on the beams. However, further research is required to investigate the influence that the continuity of a slab panel has on the yieldline pattern before it is incorporated in the design methodology.

The third and last case study was the Cardington Corner Compartment Test. The FBE analysis was able to capture the behaviour of the protected support beams adequately. However, the FBE analysis indicated that the unprotected beams would fail after 45 *min* which is not what was observed in the experiment, where no failure occurred for the full duration of the test. This is due to the fact that after the unprotected beams lose their strength, the beams are supported by the slab. This highlights an important limitation of the FBE analysis, that it is not able to capture the tensile membrane behaviour of the “support” beams when they lose their supporting function. Once again, such behaviour would typically be beyond the scope considered by the FBE methodology, and such behaviour justifies the use of FE software such as Abaqus.

7 Application of the FBE and SPM design methodology to an office building

7.1 Introduction

In this chapter, the FBE analysis and design methodology developed through this work will be applied to a compartment in a ten-storey office building. The office building is adopted from the work of Fischer et al (2019). In this chapter the structure will be designed for a 60 min standard fire rating. This will be done by designing the flooring system with the SPM and analysing the skeletal supporting structure with the FBE analysis. Therefore, the 3D FBE that was implemented in OpenSees in Chapter 4 and the interaction between the FBE analysis and SPM discussed in Chapter 5 will be applied in this case study.

The load-carrying capacity that is required will then be compared to the load-carrying capacities calculated by the SPM when the effect of the deflection of edge support beams are (a) not accounted for, (b) approximated as span/75, and (c) updated based on predicted deflections from the FBE analysis. This comparison shows the impact edge deformations have on the load-carrying capacity, as well as the effect of linking the SPM with the FBE analysis to obtain the deflection of the edge support beams.

The novel contribution of this chapter is the consideration of the interaction between the FBE and SPM analyses, along with illustrating how the proposed procedures can be applied to real buildings. Global structural interactions are considered (such as axial forces within members and P-delta effects) which are not considered by simplified methods. Further research is required to analyse a wide variety of floor and structural configurations and determine the extent to which SPM predictions are influenced by including deflections predicted by the FBE, but this chapter provides a proof of concept of the general design system and an illustration of updated SPM predictions.

7.2 Building details

The structure that the design methodology is applied to is based on an office building designed by Fischer et al (2019) using a performance-based design approach. Fischer et al (2019) investigated two designs with different lateral force resisting systems. The structure used for this example adopted the geometry of the structure with an interior rigid core. The layout of the office building can be found is illustrated in Figure 7.1.

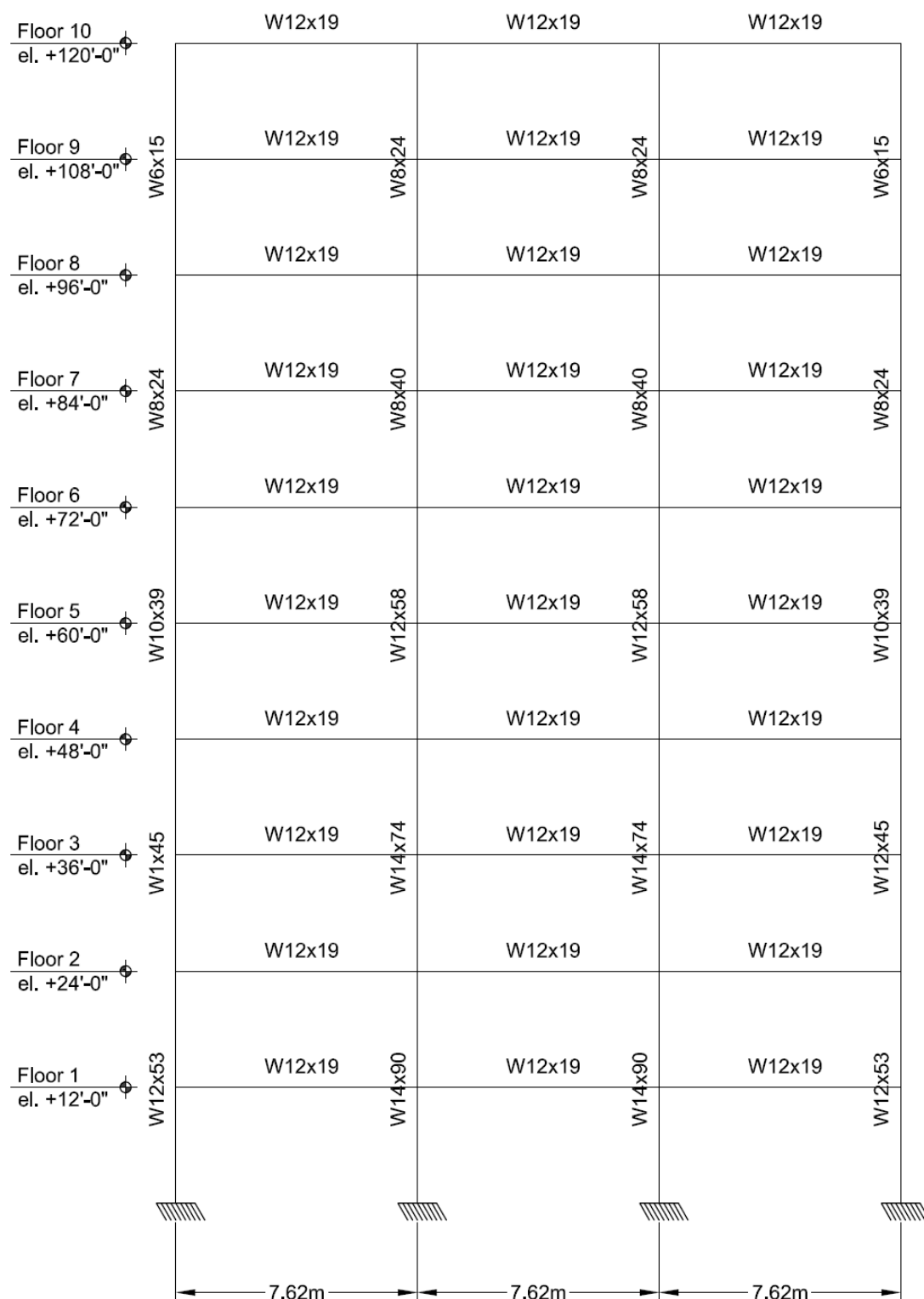


Figure 7.1: Layout of the structure indicating the columns and secondary beam sections (Fischer et al, 2019)

The fire compartment that is designed, is located on the fourth floor at the corner of the building. However, similar results are obtained when different floors are considered. The profile of the composite slab, the beams

and column sections as specified by Fischer et al (2019) was used. The loading on the beams is determined according to EN 1991 during the design of the building.

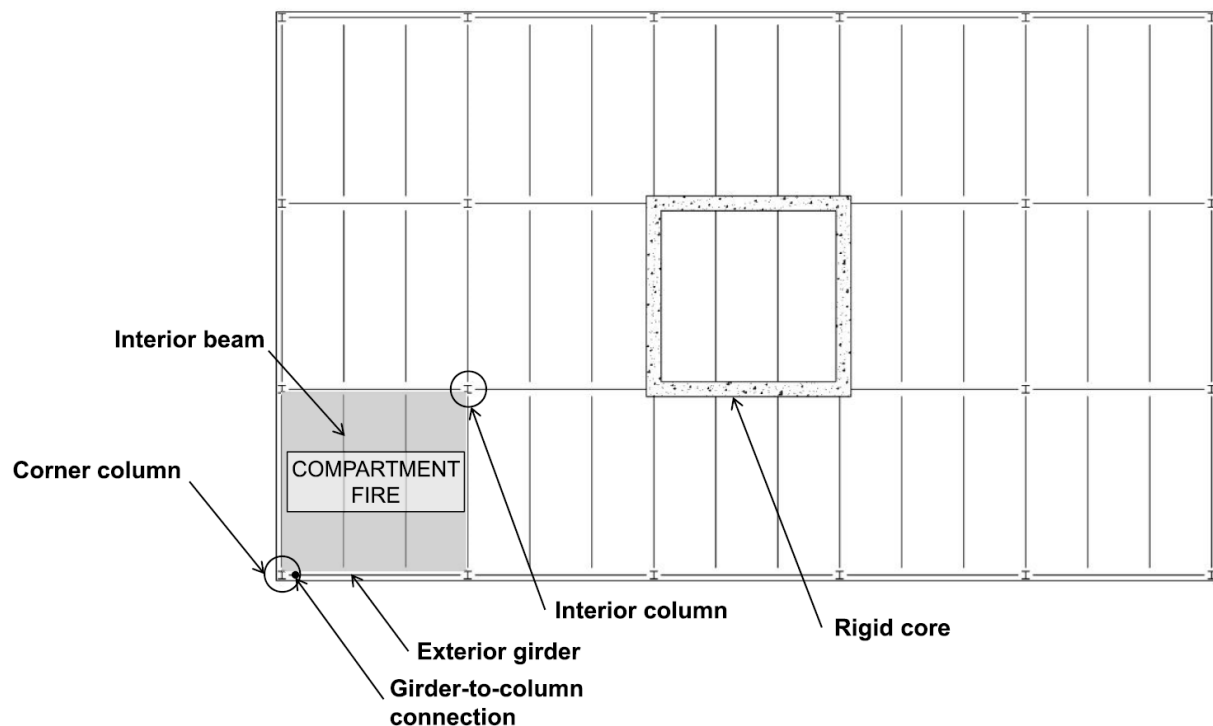


Figure 7.2: Typical layout of the floor indicating the compartment to which the design methodology will be applied (Fischer et al, 2019)

In the analysis of the structure by Fischer et al (2019), the structure failed due to the buckling of the interior column at around 83 *min* of standard fire exposure time. However, the focus of this example is the ultimate load-carrying capacity of the slab panel. Therefore, the passive protection and the reinforcement for this example were determined such that the load-carrying capacity of the slab panel will govern the design of the structure. Hence, this structure is used as a good case study, but without specific comparison to results of the original authors. Temperatures and passive protection specifications listed below have been determined in this research to allow the specific slab panel arrangement to be considered.

According to SANS 10400-T (SABS, 2011b), and similar international codes of practice, structural components in office occupancies of up to ten-storeys require a fire resistance of 60 *min* for stability.

7.2.1 Composite slab

The composite slab has a trapezoidal profile with a total depth of 140 *mm* and a rib height 65 *mm* as shown in Figure 7.3. The slab is constructed with a lightweight concrete of a class C35/45. Therefore, it is assumed that the compression strength of the concrete is 35 *MPa*, the tensile strength is 2.2 *MPa* and the modulus of elasticity is 34 *GPa*. For this example, the slab is reinforced with a mesh consisting of bars with a diameter of 6 *mm* and a spacing of 150 *mm*. The centre of the mesh is placed at 45 *mm* from the top of the slab. The yield stress of reinforcement is 420 *MPa*.

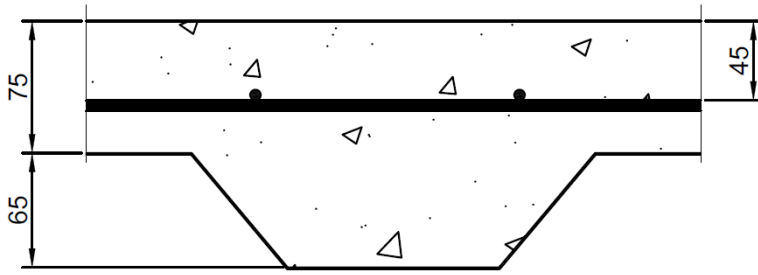


Figure 7.3: Dimensions of the composite slab with a trapezoidal deck profile

7.2.2 Steel beams and columns

The steel of the beams and the columns is assumed to be S355JR. Thus, the yield strength of the steel is 355 MPa and the modulus of elasticity is 210 GPa. The support beams and columns are protected with Isolatek Type-D C/F spray-applied fire resistive material. The thickness of the spray was determined for this example so that the load-carrying capacity of the slab panel will govern the design. Therefore, the thickness of protection for the $W12 \times 58$ columns was 17 mm protection, for the $W18 \times 35$ primary beams was 17 mm and for the $W12 \times 19$ secondary beams with 18 mm. The temperatures of the steel beams and columns that are applied to the structure in OpenSees was determined in OZone 3.0.3 (Cadorin, 2003) based on the standard fire curve. The time temperature curve for the protected columns and beam are given in Figure 7.4.

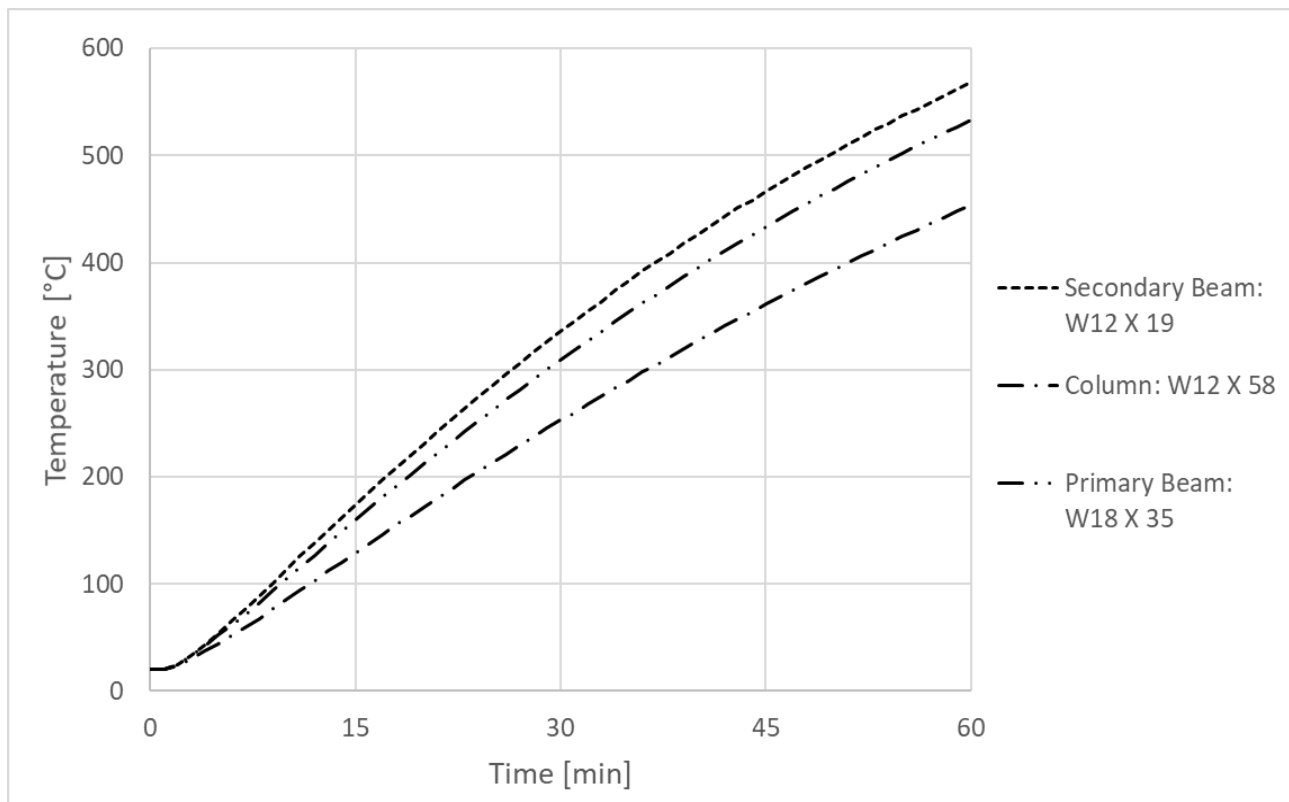


Figure 7.4: Time-temperature curve of the $W12 \times 58$ columns, $W18 \times 35$ beams and $W12 \times 19$ beams subjected to the Standard Fire Curve

The temperatures within the concrete slab were determined with one-dimensional heat transfer calculations. An effective height of 107.5 mm was used in the heat transfer calculations. The temperature profile of the concrete slab at 60 min is provided in Figure 7.5. The temperatures obtained from the heat transfer calculations are provided in Appendix C.

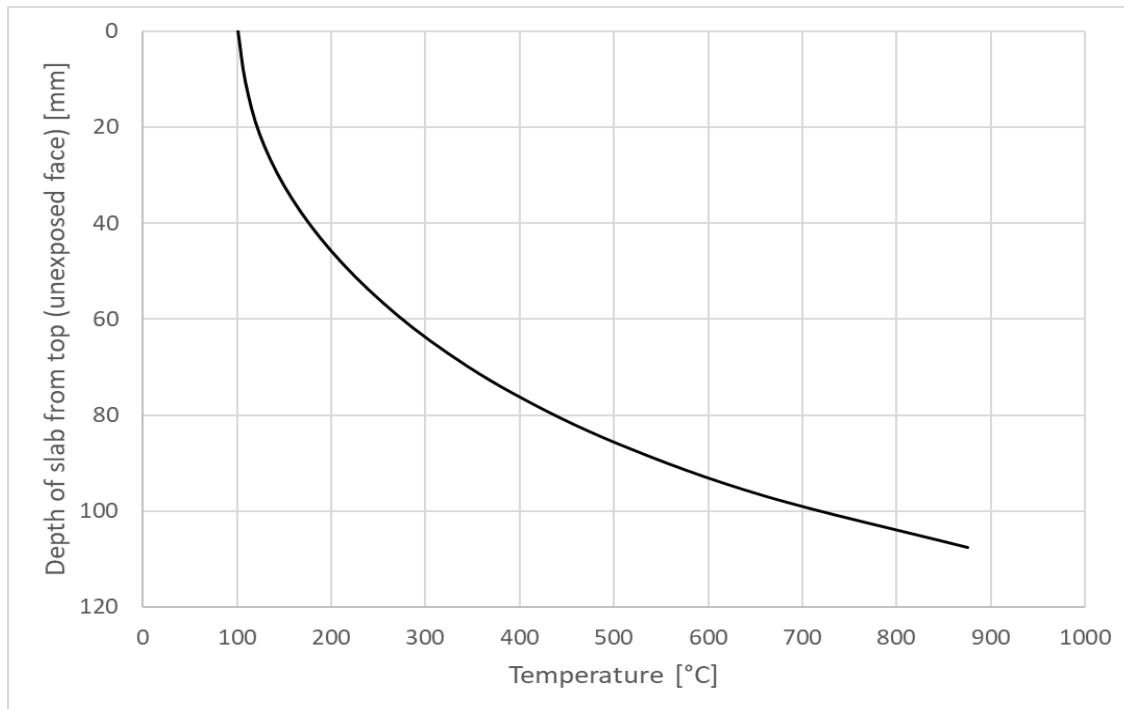


Figure 7.5: Temperature profile of the concrete slab with an equivalent thickness of 107.5 mm at 60 min

7.2.3 Loading of the structure

The structure is classified as an office building, which according to the EN 1991 (BSI, 2002b, 2002c) is a Category B structure. Therefore, the structure was designed for an imposed load, Q_k , of 3 kN/m^2 and a fire load density of 511 MJ/m^2 . The loads contributing to the dead load are summarised in Table 7.1.

Table 7.1: Dead loads applied to the slab panel

Load Case	Value [kN/m^2]
Composite Slab	1.30
Services	0.25
Partitions	1.00
Secondary Beams	0.10
Total dead Load	2.65

The fire limit state design load is calculated according to the EN 1990 load combinations (BSI, 2002a) as follows:

$$\begin{aligned}
 w_f &= G_k + 0.5 Q_k \\
 &= 2.65 \text{ kN/m}^2 + 0.5 \cdot 3 \text{ kN/m}^2 \\
 &= 4.15 \text{ kN/m}^2
 \end{aligned}
 \tag{7.1}$$

This load will be used to provide an estimate of the capacity that the structure needs to provide. However, the load applied to the structure is based up the maximum capacity of the floor based on SPM predictions.

7.3 Design of the compartment

The SPM software, SPM version 3.1.1 (Clifton, 2006) was used to determine the yieldline pattern and load-carrying capacity, w_u , of the slab panel, which has been used to calculate the loads on the support beams. The input for the SPM software is provided Appendix C, with further details provided below.

Layout of the skeletal model

The fire compartment considered in this case study has been modelled as a 3D substructure of the ten-storey building. The supporting structure of the slab panel in consideration is constrained by the rest of the structure. This was taken into account by modelling half of the supporting beams of the adjacent slab panels, as illustrated in Figure 7.6. A symmetry boundary condition was applied at the end of the support beams, which allowed vertical displacement, but fixed the rotation of the beam. The columns were assumed to be fully fixed at the bottom. At the top, the horizontal displacement of the columns was prevented, but rotation was allowed and the top of the columns were free to displace vertically to allow for axial deformations. The continuity that the concrete slab provides to the steel beam-column connections is assumed to be limited and so all the beams are connected to the columns with a pin connection. The TCL script for the model is provided in the online repository (Strauss and Walls, 2021).

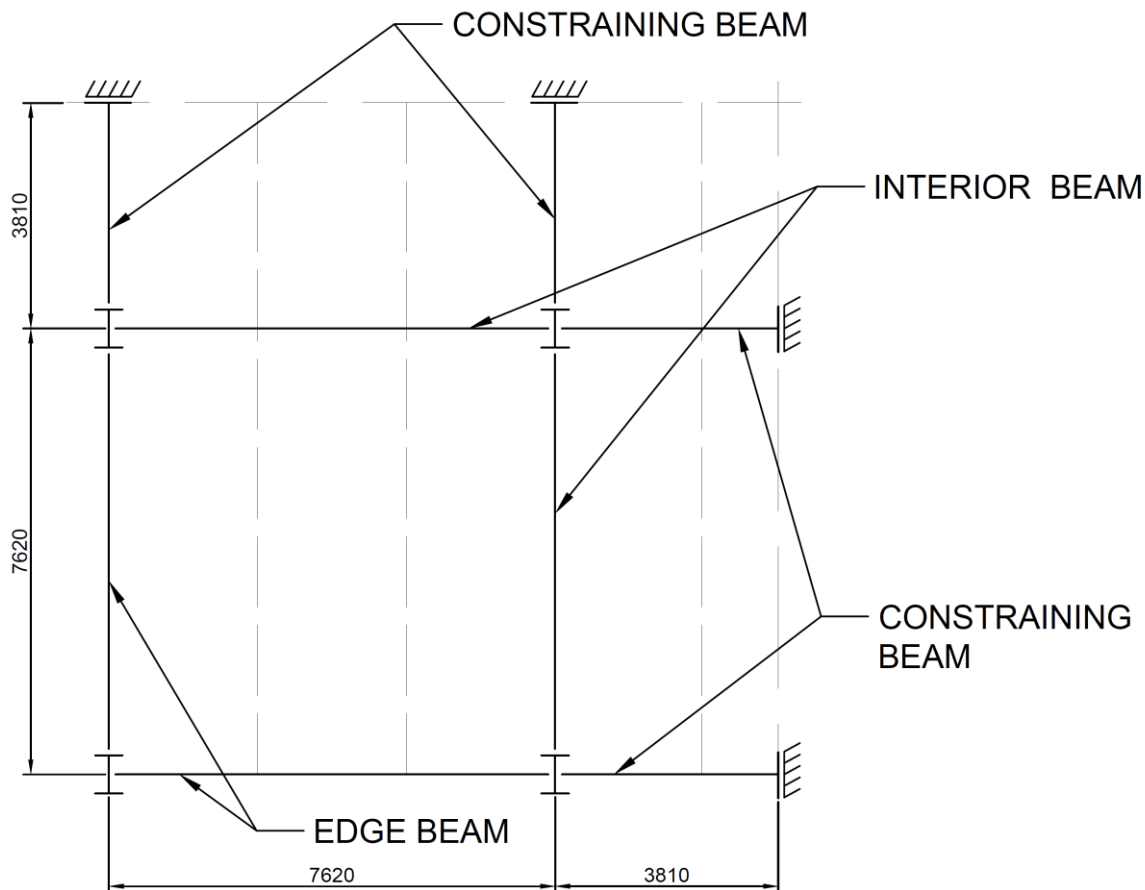


Figure 7.6: Layout of the substructure that were modelled in the FBE Analysis

For the FBE analysis was carried out by discretising each of the supporting beams into 10 elements of equal length, the constraining beams were discretised into 3 elements and the columns being analysed into 6 elements. Cross-sections were considered using 62 fibres, with 4, 10, 4, 40 and 4 fibres for the bottom flange, web, top flange concrete slab and reinforcement respectively. Hence, the entire model consists of 76 beam elements. The analysis required of 60 load steps and iterations to analyse the structure for a one hour standard fire. The OpenSees analyses took approximately 22 seconds to run on a Lenovo computer, with a 1.80 GHz Intel(R) Core(TM) i5-3337U processor. This shows that the computational effort required is low and analyses can be completed quickly. As introduced previously, cross-sectional analyses considering fibres are carried out through subroutines so global analyses only need to consider the 76 beam elements specified.

Modelling of the composite beams

The concrete in the composite beams was modelled with an effective rectangular area, which had an effective depth of 107.5 mm. The effective width of the concrete at ambient temperature was calculated according to SANS 10162-1 (SABS, 2011a), which was multiplied by 60 % to obtain the effective width of the concrete during at the fire limit state (as discussed in Section 5.2.3). The effective width of the edge beams is 548.6 mm and the effective width of the interior beams is 1143 mm.

Mechanical loads applied to the supporting structure

The yieldline pattern determined by the SPM is shown in Figure 7.7. Note that the loads from the adjacent slab panels will also be transferred to the interior beams, and thus are included.

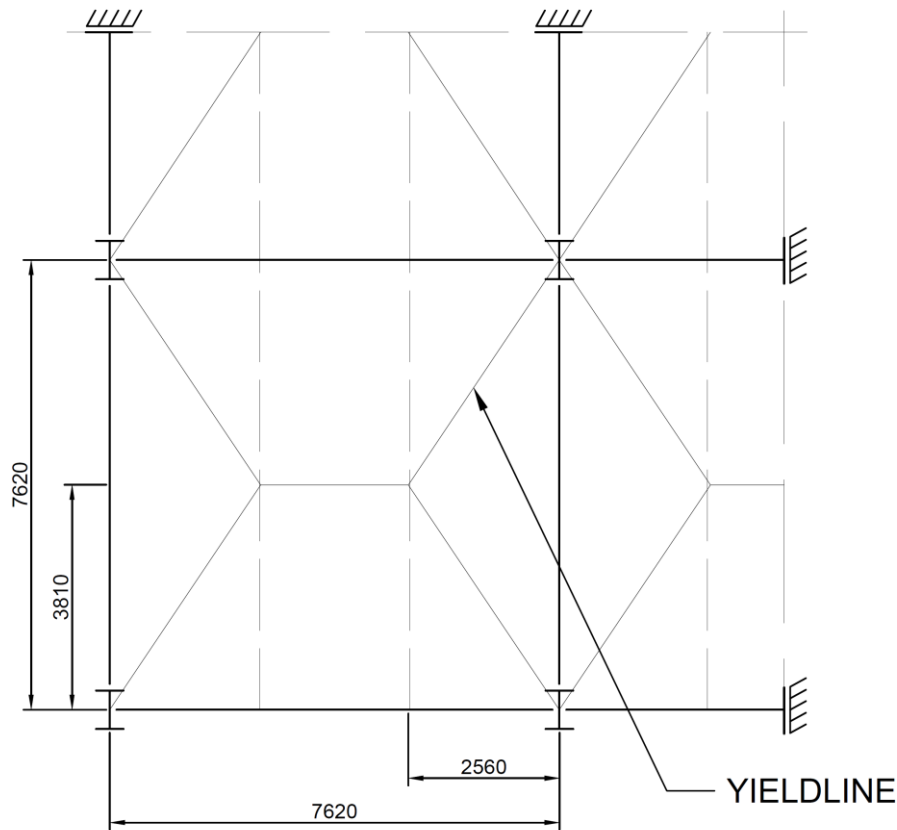


Figure 7.7: Yieldline pattern of the slab panel determined with the SPM

The loads from the sixth storey and up would be carried by the columns (since the 5th floor is being considered which is heated by a fire on the 4th floor). These loads were modelled as point loads which were applied at the top of each column. The point loads were calculated based on the tributary area supported by each column at ambient temperature, utilising the fire limit state listed above. Thus, a fire limit state point load of 301 kN was applied to the column at the corner of the structure, a point load of 602 kN to the two edge columns and 1204 kN was applied to interior column. Such loads are important when considering the behaviour of the columns, as they might cause buckling to occur.

7.4 Results and comparison of the design methodology

The FBE analysis and SPM were coupled together by iteratively updating both models, the former with updated load patterns and floor loads (based on the predicted SPM capacity) and the latter with updated primary beam deformations which leads to an updated prediction of floor capacity. The FBE model converged for all cases indicating that the resistance of the structural system was sufficient. In this work the interaction between models

was carried out manually, with the software models running separately. However, the two models could readily be combined within OpenSees to allow for seamless interaction and easy updating of results.

7.4.1 Analysis of skeletal structure

Support beams

The midspan deflections of the interior primary and secondary beams are given in Figure 7.8 and the axial forces in the support beams are given in Figure 7.9. Secondary beams refers to the passively protected W12x19 beams that support the slab panel, not those secondary beams that form part of the slab panel and fail. These results are based on the load-carrying capacity of the slab panel being 5.56 kN/m^2 . The large deformations of the secondary beams were due to the fact that less protection were applied to these beam, and therefore higher temperature developed within them. The secondary beams reached a temperature of 568°C , whereas the primary beams reached a maximum temperature of 533°C . However, about 50% of the deformation of the secondary beam was caused by thermal deformation, whereas thermal deformation only contributed about 20% of the deflection of the primary beams. Lastly, from the behaviour of the two beams, it can be seen that the rate of deflection is increasing towards the end, which indicate that the support beams are approaching their capacity.

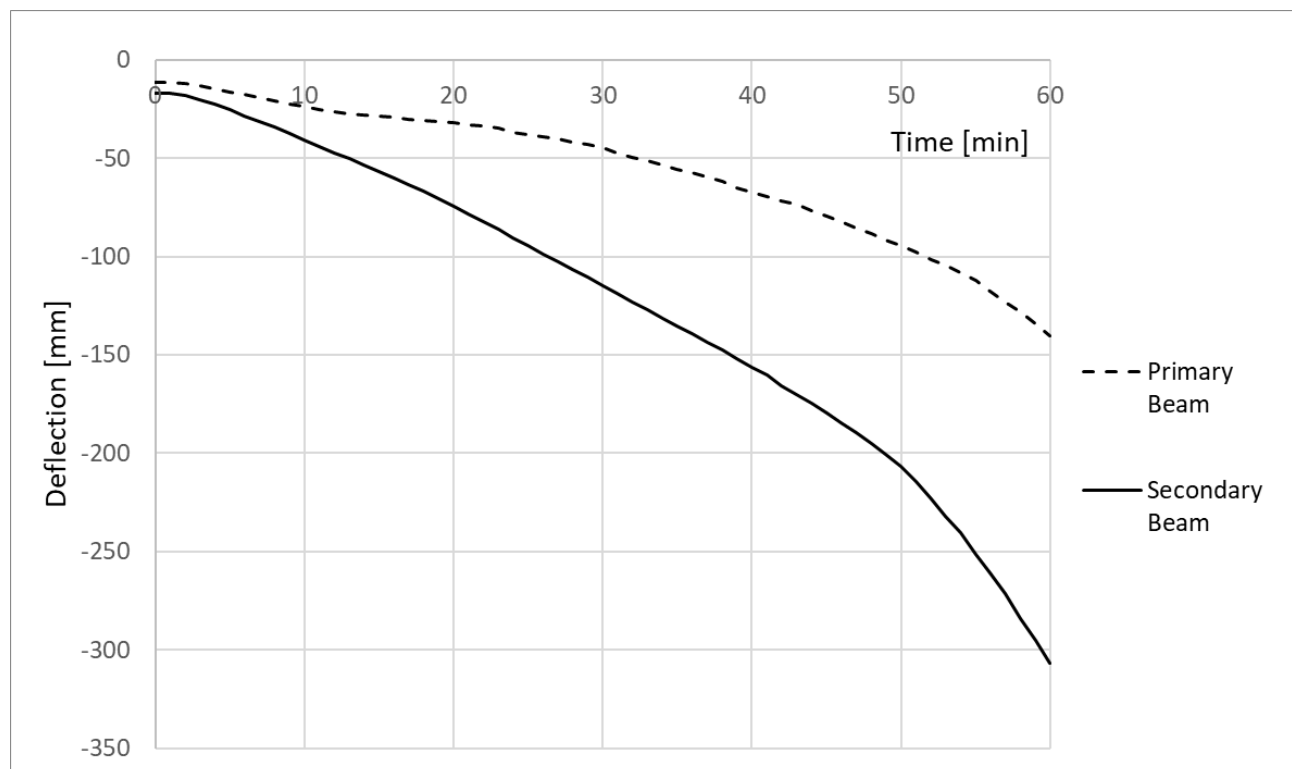


Figure 7.8: Vertical deflection at the midspan of the interior support beams during the fire

The compression forces that develop in the support beams are shown in Figure 7.9. These compression forces are caused by the thermal expansion of the beams which are constrained by the surrounding structure and the columns on the edge of the structure. The maximum force within the secondary beams was 119 kN and in the

primary beams was 38 kN . The large difference between the maximum compression forces within the secondary and primary beams are due the orientation of the columns. The secondary beams were constrained by strong axis of the beam, which allowed less movement and therefore induces a larger compression forces. Whereas, the primary beam was constrained by the weak axis of the column which allowed more movement and therefore induced a smaller compression force. The maximum compression forces within the beam occurred at 43 min . Thereafter, the compression force starts to reduce as the stiffness of the beams and the columns have reduced significantly. This illustrated the impact that the surrounding structure can have on a single element, which would not be captured by analysing the beams in isolation. It is important to note that simplified analyses, and the SPM, do not calculate or consider the axial forces that occur develop in beams, and these can be important for identifying failure modes.

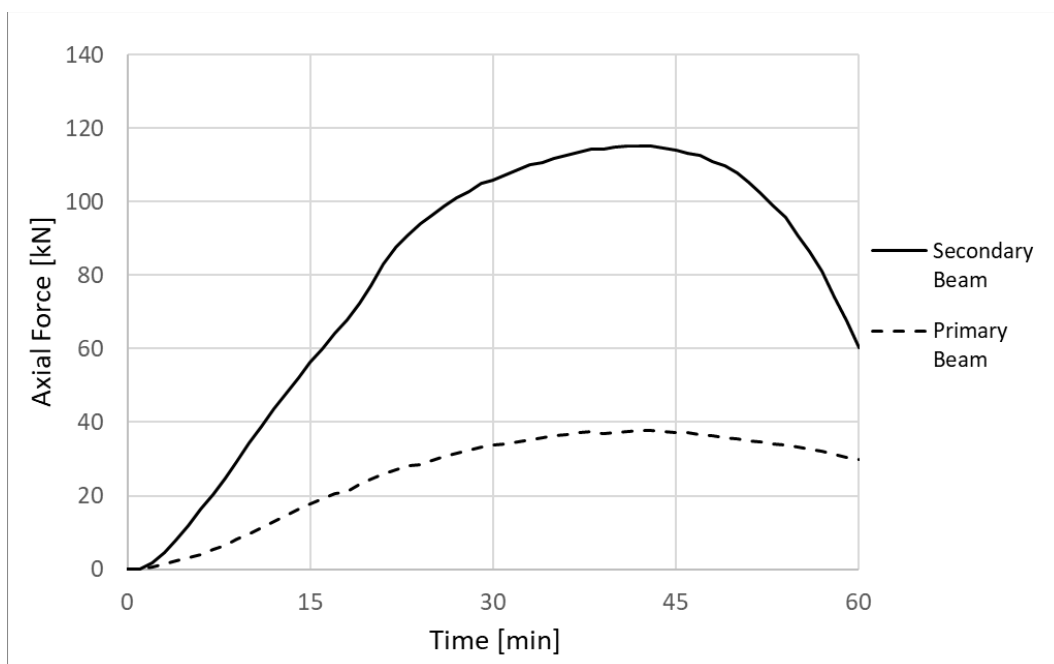


Figure 7.9: Axial forces (Compression) within the supporting beams induced by the thermal expansion

Columns

The lateral deflection in the direction of the strong and the weak axis of the corner column of the structure are shown in Figure 7.10. The column reached a maximum deflection of 18 mm about the strong axis and 37 mm about the weak axis at about 55 min . The smaller deflection of the column about its strong axis corresponds to the higher compression forces in the secondary beams and the larger deflection about the weak axis corresponds to the lower compression forces within the primary beams.

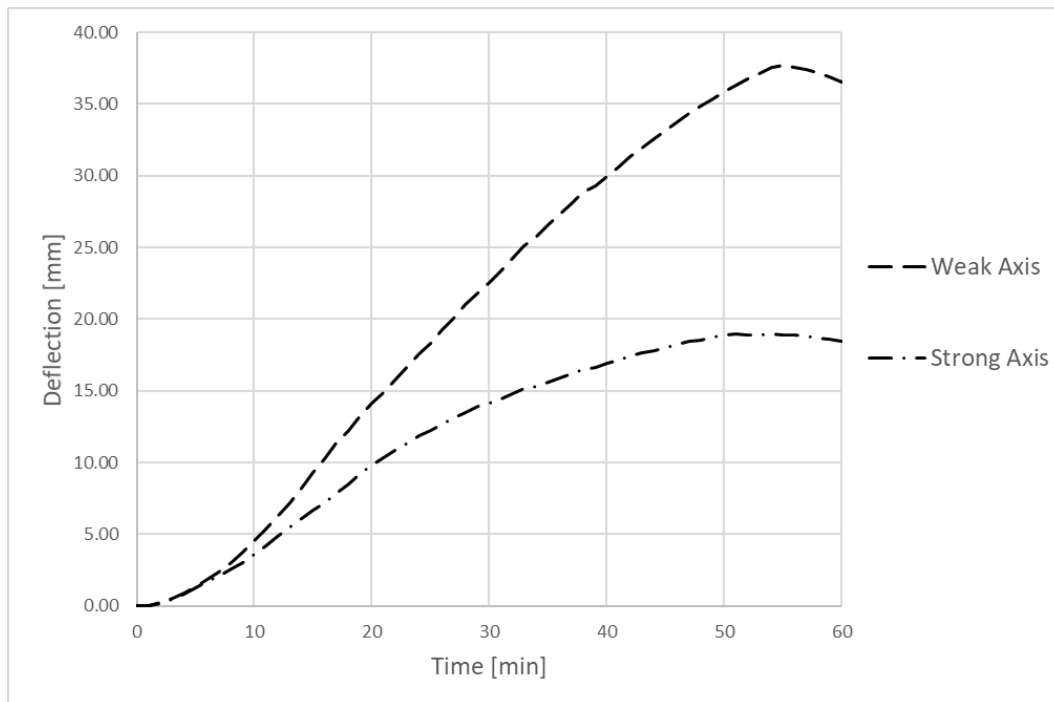


Figure 7.10: Lateral deflection of column about its weak and it strong axis

Figure 7.11 shows the bending moment within the corner column about the strong and the weak axis. The moment is mainly caused due to the expansion of the support beams. However, the P-Delta effect also contributes to the moment within the column. The maximum moments within the beams was 163 kNm about the strong axis and 60 kNm about the weak axis. The compression force within the column, due to the mechanical loads, are 382 kN . Such results illustrate the need to consider global structural interactions and non-linear effects as the additional moments may cause failure.

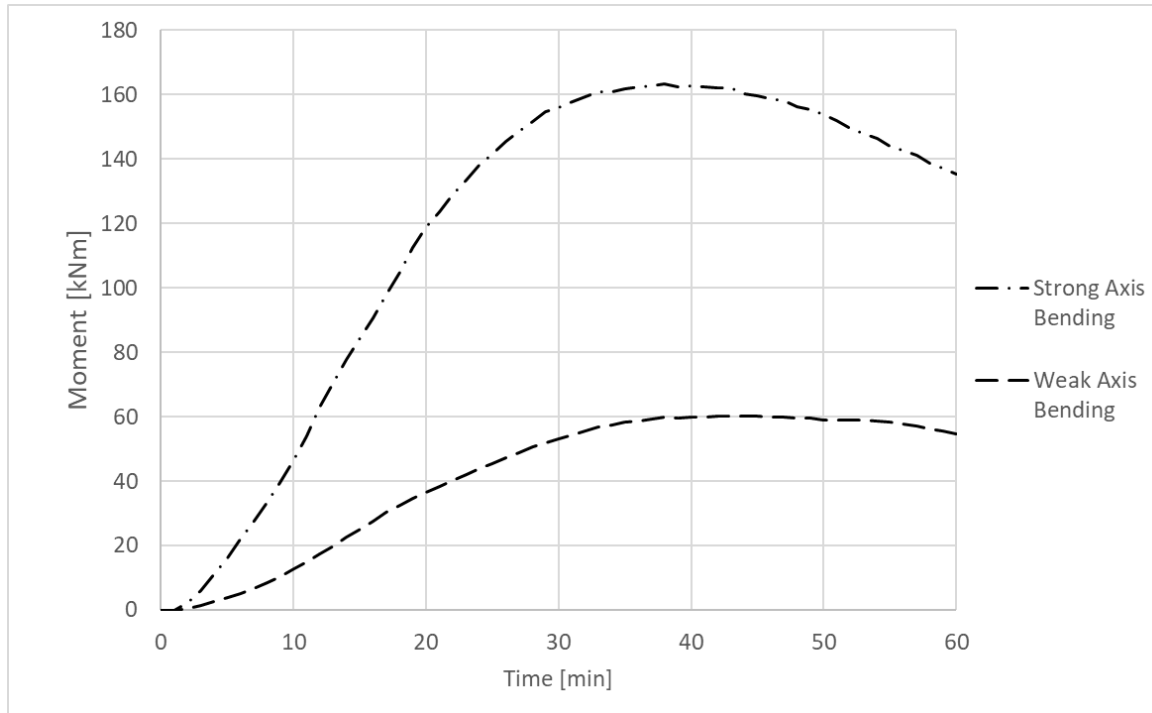


Figure 7.11: The bending moment about the weak and the strong axis within the corner column due to expansion of the support beams

If the column are simplified as a propped cantilever, with the bottom of the column being fixed and no lateral supported at the top, the moment can be calculated analytically and the results obtained from the FBE Analysis can be found to be reasonable. The moment about the weak axis at 40 *min* is calculated as follows

$$\begin{aligned}
 M &= \frac{5}{32} \cdot P \cdot l + N \cdot \Delta \\
 &= \frac{5}{32} \cdot 119 \text{ kN} \cdot 7.302 \text{ m} + 382 \text{ kN} \cdot 0.017 \text{ m} \\
 &= 142 \text{ kNm}
 \end{aligned} \tag{7.2}$$

where P is the compression force within the beam
 N is the compression force within the column
 l is the length of the column and
 Δ is the lateral deflection of the column

Similarly, the moment about the strong axis can be calculated, which result in moment of 55 *kNm*. The analytical results compare well to the results obtained from the FBE Analysis, which indicate that reasonable results were obtained from the FBE Analysis.

7.4.2 Calculation of load-carrying capacity of the slab panel

The load-carrying capacity, the edge support deflection and the limiting and maximum deflections are summarised in Table 7.2. The calculated displacement of the initial iteration, step 0, was based on the assumed deflection of span/75 (i.e. 102 mm), whereas the displacements thereafter were determined with the FBE

analysis. The limiting (Δ_{lim}) and maximum (Δ_{max}) displacements were calculated with Equation 5.6 and Equation 5.7, as discussed in Chapter 5. The deflection of the slab panel at failure, $\min(\Delta_1; \Delta_2)$, was determined as 440 mm. The limiting deflection in each iteration was manually inputted into the SPM software and the load-carrying capacity was calculated for the limiting deflection. The ultimate load-carrying capacity of the slab panel ($w_{u,i}$) converged after five iterations (step 4) to 5.77 kN/m². It is interesting to note in this case study that the nature of the iteration process is such that after Iteration Step 1 the predicted capacity did not change substantially (in relation to the level of accuracy possible in structural fire analyses). After the first iteration, the load-carrying capacity was reduced by 20%, but in subsequent iterations steps the load-carrying capacity were updated from 5.34 to 5.56 kN/m², which is an increase of 3.9%. Thus, conservatively the iterative procedure could conservatively have been stopped after Step 1 as the load-carrying capacity of 5.34 kN/m² would be sufficient for the design load. However, the overall approach shows that the predicted capacity of the floor slab decreased from 6.43 kN/m² to 5.56 kN/m², representing a change of 13.5%. Furthermore, the FBE analysis provides axial forces and bending moments in columns and beams, which assist with identifying failure.

Table 7.2: Summary of the results obtained in each iteration of the design method starting with an edge deflection approximated as Span/75. The successive deflections are based upon the FBE analysis results.

Step: i	$\Delta_{x,spsb}$ [mm]	$\Delta_{y,spsb}$ [mm]	Δ_{lim} [mm]	Δ_{max} [mm]	$w_{u,i}$ [kN/m ²]
0	102	102	397	544	6.43
1	345	165	281	589	5.34
2	298	135	310	568	5.61
3	310	142	303	573	5.54
4	307	140	305	571	5.56

The results from the design method above can be compared to two other cases, giving three different predictions of floor capacity based on the SPM: (1) where the deflection of the support beams are ignored and (2) where the deflection of the edge beams are approximated as span/75, and (3) the case where FBE results are included. The limiting deflection and load-carrying capacity for each case are given Table 7.3.

Table 7.3: Comparison between different cases where the edge deflection are ignored, approximated as span/75 or determined with the FBE Analysis

Edge Deflection	Δ_{lim} [mm]	$w_{u,i}$ [kN/m ²]
No Edge Deflection	533	7.71
Span / 75	397	6.43
FBE Analysis	328	5.56

By comparing these three cases it can first be observed that it is important to account for the edge deflection when the load-carrying capacity is calculated, as the capacity is updated from 7.71 kN/m^2 to between 6.43 and 5.54 kN/m^2 . By not taking into account the edge deflection of the slab panel, the load-carrying capacity can be over-predicted by 20% to 39%. The case where the deflections are approximated to $\text{span}/75$ yield a suitable load-carrying capacity which differs from the FBE Analysis by 16% (i.e. the FBE linked prediction is 13.5% lower). In most simple structures such predictions will be of sufficient accuracy. However, when unusual column or beam arrangements are present there is likely to be a much higher discrepancy between results. Note that simplified edge deflection of $\text{span}/75$ will not always predict a higher, i.e. less conservative, load-carrying capacity. For example, when the support beams are over designed (e.g. if governed by seismic requirements), it will result in reduced edge deflections and a deflection of $\text{span}/75$ will be conservative. However, the FBE analysis enables designers to optimise layouts and complex systems by permitting larger deflections of the support beams, which can lead to decreased amounts of passive protection required.

7.5 Conclusion

In this chapter the combined FBE and SPM design methodology was applied to a sub-structure of a composite 10-storey office building as an example. The geometry of the structure were adopted from the work of Fisher et al (2019), which included the steel beam and column sizes and the profile of the concrete deck. However, the passive protection and the reinforcement in the concrete deck were design for this example such that the slab panel would govern the design. The design load for the structure were calculated as 4.15 kN/m^2 and the Fire Load Energy Density of 511 MJ/m^2 . The predicted slab capacity exceeded the capacity required.

A FBE analysis of the supporting skeletal structure was performed in OpenSees, which consisted of 76 beam elements of which the cross-sections consisted of 62 fibres. It took about 22 seconds to perform the analysis. The results of the FBE analysis were discussed, highlighted the impact that the surrounding structure have on the support beams. The compression forces that the developed in the secondary beams was 119 kN and in the primary beams was 38 kN . The secondary beams had a maximum deflection of 307 mm and the primary beams had a maximum deflection of 140 mm .

The load-carrying capacity of the slab panel was determined through an iterative process in which the SPM software was used to calculate the load-carrying capacity of the slab panel based on the edge deflections and the edge deflections were determined with the FBE analysis. In the first Iterations step the load-carrying capacity of the slab panel was reduced by 20%, but subsequent iterations increased the load-carrying capacity by only 3.6%. The ultimate load-carrying capacity of the slab panel was 5.56 kN/m^2 . This chapter provides a proof of concept linking the SPM and FBE methodologies together, which now requires further work to investigate a wide variety of structural layouts and geometries.

8 Conclusion

8.1 Overview

The aim of thesis research was to develop a design methodology that can be used to analyse a full 3D structure that is subjected to a compartment fire. This was done by using the Fire Beam Element (FBE), to model and analyse the supporting skeletal structure and the Slab Panel Method (SPM), developed by Clifton (2006), to design the slab. These two methods were able to interact with each other through an iterative process, where the loads on the supporting structure are transferred from the slab panel and the deflection of the support beams are used to update the SPM.

In order to apply the FBE in the design methodology, the FBE formulation had to be developed further so that it could be used in FBE analysis of 3D structures, building on the work of Walls (2016) and Volkmann (2018). For a 3D FBE, the position of the neutral axes (NA) had to be calculated for the strong and the weak axes, using the Fibre Section approach. The Finite Element Matrices that accounts for the eccentricity of the NA were derived for the 3D FBE based on the Euler-Bernoulli assumptions. The FBE formulation for the FBE were then implemented in a Finite Element Software, OpenSees. The *FireFiberSectionGJ*-class was developed for the cross-section which is able to calculate the position of the NA. The *FireEl3d* and *FireEl3dUni*-classes were developed for the 3D FBE of which the latter class represents a continuous laterally supported beam which is only able to deflect in the y-direction. This class was used for the composite beams that are laterally supported by the slab panel.

After the 3D FBE was developed and implemented, the FBE analysis and the SPM were linked to each other with an iterative process. The SPM is used to determine the loads on the supporting beams in the FBE Analysis. In return, the FBE Analysis is used to update the edge deflections of the slab panel which are used in calculating the load-carrying capacity of the slab panel.

The FBE analysis of 3D skeletal structure were validated with three case studies. The case studies varied in complexity and consisted of a numerical benchmark study of a composite slab with four columns modelled in Vulcan, the Second Munich Test and the Cardington Corner Compartment Test (Test 3). The focus of the validations was the use of FBE analysis for the supporting skeletal structure to predict the behaviour of the support beams.

Lastly, the FBE and SPM design methodology was applied to a ten-storey office building. The geometry of the building was adopted from the work of Fischer et al (2019) in which the building was considered using performance-based design. The results obtained using the FBE analysis were presented, which included the axial forces within the support beams, the bending moment within the columns, the horizontal displacement of the columns and the vertical displacement of the beams. The effect of updating the deflections of the support beams on the load-carrying capacity of the slab panel was discussed.

8.2 Consideration of objectives

The objectives of the research, presented in Chapter 1, have been addressed throughout the thesis as follows:

- The FBE methodology was developed for a 3D element in Chapter 3. The FBE formulations were extended so that the position of the NA are calculated for the strong and the weak axes, the resultant Thermal Strain Load (RTSL) and Moments (RTSM) and the section stiffness are calculated for a cross-section of a 3D beam element. In Chapter 4, the FBE methodology was implemented into OpenSees.
- In Chapter 5, the interaction between the FBE analysis and the SPM was addressed, in which the SPM was used to determine the loads on the support beams based on the yieldline pattern and the load-carrying capacity of the slab panel. In return, the deflections of the support beams determined in the FBE analysis were used to calculate the limiting and maximum deflection which are used to calculate the load-carrying capacity of the slab panel. This is done through an iterative process.
- The behaviour of the 3D FBE in FBE analysis was validated in Chapter 6, with three case studies, which illustrated the behaviour of the FBE in 3D model. Typically good correlations with experimental and numerical data was obtained. In these case studies limitations of the FBE analysis were also identified.
- The design methodology was applied to a ten-storey structure in Chapter 7 and the effect that the updating of the deflections of the support beams have on the ultimate load capacity of the slab panel.

8.3 Summary of findings

8.3.1 *Interaction between the FBE analysis and SPM*

A key aspect of the design methodology is the interaction between the FBE analysis and the SPM through an iterative process. The loads that are applied to the support beams in the FBE analysis are calculated based on the load applied over the tributary area of the support beams according to the yieldline pattern of the slab panel, as recommended by Clifton (2006). The load-carrying capacity of the slab panel are used as the magnitude of the load that is transferred to the support beams. For the first iteration, the load-carrying capacity of the slab panel are calculated, assuming a support beam deflection of $\text{span}/75$. Thereafter, in the subsequent iterations, the support beam deflections determined in the FBE analysis are used to calculate the load-carrying capacity.

To incorporate the deflection of the support beams determined with the FBE analysis, the equations, in the SPM, to calculate the limiting and maximum deflection had to be modified. In the SPM about 60% to 70% of the edge deformation, which are approximated as $\text{span}/75$, affects the limiting and maximum deflection of the slab panel. Therefore, in the modified equations for the limiting and maximum deflections, the deflection of the support beams were multiplied by a factor of 0.7.

8.3.2 *Validation of FBE analysis*

The first case study is based on a benchmark study modelled in Vulcan by Burgess and Alexandrou (COST, 2014). The behaviour of the 3D FBE compared well to the results of the Vulcan model and differ on average

with 7.4% in the short span (x-direction) and 5.7% in the long span (y-direction). This case study illustrated the behaviour of the 3D FBE without any effects due to continuity or constraint through the rest of the structure.

The second case study was based on the Second Munich Test, conducted by Mensinger et al (2011) and analysed by Stadler (2012). In this case study the results using a 3D FBE were compared to previous analyses done by Walls (2016) applying the FBE methodology with 2D elements. The displacements of the support beams at 40 min were typically in good agreement with the experiment and the models of Stadler and Walls and the FBE was able to capture the behaviour of the intermediate beam during the heating phase adequately. The case study indicated that continuity of the slab panel should be investigated further to be taken into account in the yieldline pattern and loading of the edge beam.

In the third case study the ability of the FBE methodology to capture complex phenomena for some beams is illustrated. However, the limitations of the FBE methodology where the predictions become less accurate were also highlighted. The FBE analysis was not able to capture the behaviour of the unprotected support beams after they have lost most of their strengths and the beams become supported by the slab. Although, more complex models than the FBE analysis were also not able to fully capture the behaviour of the considered beam after it lost most of its strength. This case study highlighted the limitation of the FBE analysis, that it should not be applied to cases where tensile membrane cases govern the behaviour of the “support” beam.

8.3.3 *Application of the FBE and SPM design methodology*

The ultimate-load carrying-capacity of the a ten-storey building was determined by applying the FBE and SPM design methodology. The predicted load-carrying capacity of the slab panel exceeded the capacity required to resist the design loads.

It was illustrated that the computational effort required to perform the FBE analysis is low and that the analysis could be performed quickly. Besides the deflections of the support beams, the FBE analysis was able to provide the axial forces within the support beams and the bending moments in the columns that developed due to thermal expansion of the support beam, which are constrained by the columns and the rest of the structure that are not subjected to the fire. This behaviour cannot be captured with simplified methods.

In the iterative process when the ultimate load-carrying capacity were calculated, it was shown that the process converges quickly and after the first iteration, the load-carrying capacity is within a reasonably accurate compared to the final predicted ultimate-load carrying capacity of the slab panel. Furthermore, the FBE analysis combined with the SPM would allow complex systems to be optimised by permitting larger deflections of the support beams.

8.4 Future work

This research built upon the development of the FBE methodology by Walls (2016) and the implementation of the FBE methodology for 2D structures with restraint by Volkmann (2018). In this research, the FBE

methodology were extended to 3D structures and linked with the SPM to develop a design methodology for a full 3D structure. In the research the following aspects in the design methodology that require further research were highlighted:

- The determination of the torsional stiffness of the cross-section at elevated temperatures,
- The effect of large edge displacements of the slab panel on the yieldline pattern of the slab panel,
- The effect of the continuity of the slab panel over a support beam on the yieldline pattern of the slab panel and
- The design methodology should be extended to include cases where the slab panel is not supported by a protected steel beam, but by the adjacent slab panel that is not subjected to the fire.

Furthermore, the SPM and the FBE analysis can be combined in OpenSees, especially if the deflection of the support beam will influence the yieldline pattern of the slab panel. The combined FBE and SPM design methodology should be investigated for a wide variety of structural layouts and geometries.

8.5 Closing remarks

A simplified design and modelling methodology, which incorporated the FBE methodology and the SPM, to design full structures subjected to fire was developed in this research. This design methodology can be applied to standard composite structures with rectangular slab panels that are supported on their edges with protected steel beams. This design methodology has the potential to minimise the use of passive protection as the interior secondary beams of a slab panel does not require passive protection with the SPM and the protection of the support beams can be optimised with the FBE analysis. Hence, the design methodology can possibly lead to a more cost effective design. Further research is required investigating the effect large deflections and the continuity of the slab panel on the yieldline pattern of a slab panel, as well as the effect of an adjacent structure to a slab panel that is not affected by the fire, so that the design methodology could be applied to more complex design scenarios. The work could be expanded to be applied to construction technologies such as composite timber-concrete systems, mass timber structures in general when charring is accounted for and even typical concrete frames.

9 References

- Abu, A. K. (2008) *Behaviour of Composite Floor Systems in Fire*. The University of Sheffield.
- Abu, A. K. and Burgess, I. W. (2010) 'The effect of edge support on tensile membrane action of composite slabs in fire', in *Proceedings of SDSS' Rio 2010: International Colloquium Stability and Ductility of Steel Structures*, pp. 21–32. Available at: <https://www.researchgate.net/publication/47537775>.
- ASFP (2007) *The Yellow Book - Fire protection for structural steel in buildings 5 th Edition*. 5th edn. Hampshire, UK: Association for Specialist Fire Protection.
- Bailey, C. G. (2001) 'Membrane action of unrestrained lightly reinforced concrete slabs at large displacements', *Engineering Structures*, 23(5), pp. 470–483. doi: 10.1016/S0141-0296(00)00064-X.
- Bailey, C. G. and Moore, D. B. (2000a) 'The structural behaviour of steel frames with composite floorslabs subject to fire: Part 1: Theory', *Structural Engineer*, 78(11), pp. 19–27.
- Bailey, C. G. and Moore, D. B. (2000b) 'The structural behaviour of steel frames with composite floorslabs subject to fire: Part 2: Design', *Structural Engineer*, 78(11), pp. 28–33.
- Bhatti, M. A. (2006) *Bhatti, M. Asghar. Advanced Topics in Finite Element Analysis of Structures : with Mathematica and MATLAB Computations*. New Jersey: John Wiley & Sons, Ltd.
- Bresler, B., Iding, R. and Nizamuddin, Z. (1977) *FIRES RC II-a computer program for the fire response of structures-reinforced concrete frames (revised version).*, Report No. UCB FRG 77-8.
- British Steel plc. (1999) *The Behaviour of Multi-storey Steel Framed Buildings in fire: a European joint research programme*. Moorgate, UK: British Steel plc, Swinden Technology Centre.
- BSI (2000) *BS 5950 : Structural use of steelwork in building - Part 1: Code of practice for design - Rolled and welded sections*. London: British Standards Institute.
- BSI (2002a) *BS EN 1990: 2002 - Eurocode 0 - Basis of structural design*. London: British Standard Intitute.
- BSI (2002b) *BS EN 1991-1-1:2002 - Eurocode 1: Actions on structures - Part 1-1: General actions - Densities, self-weight, imposed loads for buildings*. London: British Standards Institute.
- BSI (2002c) *BS EN 1991-1-2:2002 - Eurocode 1: Actions on structures - Part 1-2: General actions - Actions on structures exposed to fire*. London: British Standards Institute.
- BSI (2004a) *BS EN 1992-1-2:2004 - Eurocode 2: Design of concrete structures - Part 1-2: General rules - Structural fire design*. London: British Standards Institute.

- BSI (2004b) *BS EN 1994-1-1: 2004 - Eurocode 4: Design of composite steel and concrete structures - Part 1-1: General rules and rules for buildings*. London: British Standards Institute.
- BSI (2005) *BS EN 1993-1-2:2005: Eurocode 3: Design of steel structures - Part 1-2: General rules - Structural fire design*. London: British Standards Institute.
- Buchanan, A. H. and Abu, A. K. (2017) *Structural Design For Fire Safety*. 2nd edn. New York: Wiley.
- Burgess, I. W. and Chan, B. (2020) ‘An integrated yield-line approach to tensile and compressive membrane actions in thin lightly-reinforced concrete slabs’, *Engineering Structures*. Elsevier, 208, pp. 1–20. doi: 10.1016/j.engstruct.2020.110321.
- Cadorin, J.-F. (2003) ‘On the application field of OZone V2’, p. 25.
- Cai, Y., Paik, J. K. and Atluri, S. N. (2009) ‘Large deformation analyses of space-frame structures, with members of arbitrary cross-section, using explicit tangent stiffness matrices, based on a von karman type nonlinear theory in rotated reference frames’, *CMES - Computer Modeling in Engineering and Sciences*, 53(2), pp. 117–145. doi: 10.3970/cmcs.2009.053.123.
- Clifton, G. C. (2001) ‘Design of multi-storey steel framed buildings with unprotected secondary beams or joists for dependable inelastic response in severe fires’, *HERA*, (60), pp. 1–58.
- Clifton, G. C. (2006) ‘Design of composite steel floor systems for severe fires, HERA Report R4-131’, *HERA*. Manukau City: New Zealand Heavy Engineering Research Association.
- Clifton, G. C. (2011) ‘Design of Composite Steel Floor Systems for Severe Fires: The Slab Panel Method’, in *Fire Forum*. The University of Auckland.
- Clifton, G. C. and Abu, A. K. (2014) *Modifications to the Application of the SPM:2006 Edition and Application to C/VM2*. Auckland.
- COST (2014) *Benchmark studies Experimental validation of numerical models in fire engineering*. Prague: CTU Publishing House, Cech Technical University.
- Deeny, S. M. (2010) *The implications of compartment fire non-uniformity for the membrane action of reinforced concrete slabs*. The University of Edinburgh. Available at: <http://hdl.handle.net/1842/5077>.
- Fischer, E. C., Varma, A. H. and Agarwal, A. (2019) ‘Performance-Based Structural Fire Engineering of Steel Building Structures: Design-Basis Compartment Fires’, *Journal of Structural Engineering*, 145(9). doi: 10.1061/(asce)st.1943-541x.0002370.
- Franssen, J.-M. (2005) ‘SAFIR: A thermal/structural program for modeling structures under fire’, *Engineering Journal*, 42(3), pp. 143–150. Available at: <https://www.researchgate.net/publication/292660602>.

- Gales, J., Maluk, C. and Bisby, L. (2012) ‘Large-scale structural fire testing - How did we get here, Where are we, and where are we going?’, in Gomes, J. F. S. and Vaz, M. A. P. (eds) *15th International conference on experimental mechanics: Fire symposium*. Porto, Portugal, pp. 1–22. Available at: <http://hdl.handle.net/1842/6176>.
- Gillie, M. (2009) ‘Analysis of heated structures: Nature and modelling benchmarks’, *Fire Safety Journal*, 44(5), pp. 673–680. doi: 10.1016/j.firesaf.2009.01.003.
- Gillie, M., Usmani, A. S. and Rotter, J. M. (2001) ‘A structural analysis of the Cardington British Steel Corner Test’, *Journal of Constructional Steel Research*, 58(4), pp. 427–442. doi: 10.1016/S0143-974X(01)00066-9.
- Gu, T. (2016) *Effect of Edge Beam Deformations on the Slab Panel Method*. University of Canterbury.
- Guo, Q. *et al.* (2013) ‘Probabilistic Evaluation of Structural Fire Resistance’, *Fire Technology*, 49(3), pp. 793–811. doi: 10.1007/s10694-012-0293-6.
- Huang, Z., Burgess, I. W. and Plank, R. J. (1999) ‘The influence of shear connectors on the behaviour of composite steel-framed buildings in fire’, *Journal of Constructional Steel Research*, 51(3), pp. 219–237. doi: 10.1016/S0143-974X(99)00028-0.
- Huang, Z., Burgess, I. W. and Plank, R. J. (2003) ‘Modeling Membrane Action of Concrete Slabs in Composite Buildings in Fire. II: Validations’, *Journal of Structural Engineering*, 129(8), pp. 1103–1112. doi: 10.1061/(asce)0733-9445(2003)129:8(1103).
- ISO (1999) *ISO 834 Fire-resistance test - Elements of building construction. Part 1-12*. Geneva: International Organization for Standardization.
- Jiang, J. (2012) *Nonlinear thermomechanical analysis of structures using OpenSees*. The University of Edinburgh.
- Jiang, J. *et al.* (2015) ‘OpenSees software Architecture for the Analysis of Structures in Fire’, *Journal of Computing in Civil Engineering*, 29(1), pp. 1–13. doi: 10.1061/(ASCE)CP.1943-5487.0000305.
- Jiang, J. *et al.* (2020) ‘Reduced-Order Modeling of Composite Floor Slabs in Fire. II: Thermal-Structural Analysis’, *Journal of Structural Engineering*, 146(6). doi: 10.1061/(asce)st.1943-541x.0002607.
- Jiang, J. and Usmani, A. S. (2013) ‘Modeling of steel frame structures in fire using OpenSees’, *Computers and Structures*, 118, pp. 90–99. doi: 10.1016/j.compstruc.2012.07.013.
- Jiang, J., Usmani, A. S. and Li, G.-Q. (2014) ‘Modelling of steel-concrete composite structures in fire using OpenSees’, *Advances in Structural Engineering*, 17(2), pp. 249–264. doi: 10.1260/1369-4332.17.2.249.

- Jiang, L. (2017) *OpenSees for fire*. Available at: <https://openseesforfire.github.io/>.
- Khorasani, N. E., Gernay, T. and Fang, C. (2019) ‘Parametric Study for Performance-Based Fire Design of US Prototype Composite Floor Systems’, *Journal of Structural Engineering*, 145(5). doi: 10.1061/(ASCE)ST.1943-541X.0002315.
- Law, A. and Bisby, L. (2020) ‘The rise and rise of fire resistance’, *Fire Safety Journal*. Elsevier Ltd, 116. doi: 10.1016/j.firesaf.2020.103188.
- Lennon, T. and Moore, D. B. (2003) ‘The natural fire safety concept - Full-scale tests at Cardington’, *Fire Safety Journal*, 38(7), pp. 623–643. doi: 10.1016/S0379-7112(03)00028-6.
- Lim, Z. Y., Clifton, G. C. and Pennington, A. (2012) *Testing of Slab Panel Method Program in Severe Fires*. University of Auckland.
- McGuire, W., Gallagher, R. H. and Ziemian, R. D. (2014) *Matrix Structural Analysis*. 2nd edn. New York: Wiley.
- McKenna, F., Scott, M. H. and Fenves, G. L. (2010) ‘Nonlinear Finite-Element Analysis Software Architecture Using Object Composition’, *Journal of Computing in Civil Engineering*, 24(1), pp. 95–107. doi: 10.1061/(asce)cp.1943-5487.0000002.
- Mensingher, M. *et al.* (2011) *Nutzung der Membran-wirkung von Verbundtrager-Decken-Systemen im Brandfall*. DAST-Forschungsbericht.
- Mróz, K., Hager, I. and Korniejenko, K. (2016) ‘Material Solutions for Passive Fire Protection of Buildings and Structures and Their Performances Testing’, *Procedia Engineering*, 151, pp. 284–291. doi: 10.1016/j.proeng.2016.07.388.
- O’Loughlin, E. and Lay, S. (2015) ‘Structural fire resistance: Rating system manifests crude, inconsistent design’, *Case Studies in Fire Safety*, 3, pp. 36–43. doi: 10.1016/j.csfs.2015.03.001.
- SABS (2011a) ‘SANS 10162-1:2011 The structural use of steel Part 1: Limiting-states design of hot-rolled steelwork’. Pretoria: South African Bureau of Standards.
- SABS (2011b) *SANS 10400-T:2011 The application of the National Building Regulations Part T: Fire protection*. Pretoria: South African Bureau of Standards.
- Sanad, A. M. (2000) *British Steel Fire Test3 : Reference ABAQUS model using grillage representation for slab Research Report*. Edinburgh, UK.
- SCI (1991) *Investigation of Broadgate Phase 8 Fire, Structural Fire Engineering*. Cheshire, UK: County Offset.

- Scott, M. H. *et al.* (2008) ‘Software Patterns for Nonlinear Beam-Column Models’, *Journal of Structural Engineering*, 134(4), pp. 562–571. doi: 10.1061/(asce)0733-9445(2008)134:4(562).
- Stadler, M. (2012) *Design of Composite Slab Systems in Case of Fire Using Simplified Finite Element Analyses*. Technischen Universität München.
- Strauss, L. and Walls, R. S. (2021) *Modelling of 3D structures in fire as skeletal frames using the Fire Beam Element (FBE) for simplified analysis and design - MEng Thesis - Lourens Strauss*. doi: doi.org/10.25413/sun.13950794.
- Usmani, A. S. and Jiang, L. (2013) ‘Modelling of structures in fire using OpenSees’, in *OpenSees Webinar*. The University of Edinburgh. Available at: <https://www.wiki.ed.ac.uk/display/opensees>.
- Volkman, J. F. (2018) *Implementation of the Fire Beam Element (FBE) in OpenSees for the analysis of structures in fire*. Stellenbosch University.
- Volkman, J. F., Walls, R. S. and de Koker, N. (2020) ‘Implementation of the fire beam element method into OpenSees for the analysis of structures in fire’, *Advances in Structural Engineering*, 23(15), pp. 3239–3250. doi: 10.1177/1369433220933451.
- Walls, R. S. (2016) *A beam finite element for the analysis of structures in fire*. Stellenbosch University.
- Walls, R. S., Viljoen, C. and de Clercq, H. (2018) ‘Analysis of Structures in Fire as Simplified Skeletal Frames Using a Customised Beam Finite Element’, *Fire Technology*, 54(6), pp. 1655–1682. doi: 10.1007/s10694-018-0762-7.
- Walls, R. S., Viljoen, C. and de Clercq, H. (2019a) ‘A nonlinear, beam finite element with variable, eccentric neutral axis’, *Engineering Structures*, 187, pp. 341–351. doi: 10.1016/j.engstruct.2019.02.056.
- Walls, R. S., Viljoen, C. and de Clercq, H. (2019b) ‘Parametric investigation into the cross-sectional stress-strain behaviour, stiffness and thermal forces of steel, concrete and composite beams exposed to fire’, *Journal of Structural Fire Engineering*, 11(1), pp. 100–117. doi: 10.1108/jsfe-10-2018-0031.
- Yang, Y. and McGuire, W. (1986) ‘Stiffness Matrix for Geometric Nonlinear Analysis’, *Journal of Structural Engineering*, 112(4), pp. 853–877. doi: 10.1061/(ASCE)0733-9445(1986)112:4(853).

Appendix A – Functions developed for the FireFiberSectionGJ and FireEl3d classes in OpenSees

The functions developed for the *FireFiberSectionGJ*-class and the *FireEl3D*-class are presented in this appendix. The code were in C++ in Microsoft Visual Studio 2017.

A.1 Functions developed for *FireFiberSectionGJ*-class

A.1.1 *calculateC*-function

The *calculateC*-function is an additional function in the *FireFiberSectionGJ*-class that calculates the NA of the cross-section and returns the components of the NA in a Vector. The method receives a Vector containing the location and temperature of the 25 temperature points over the height of the cross-section.

```
const Vector&
FireFiberSectionGJ::calculateC(Vector &dataMixed)
{
    DataMixed = dataMixed;
    double stiffnessData[3]; //declare storage array for stiffness
    stiffnessData[0] = 0.0;
    stiffnessData[1] = 0.0;
    stiffnessData[2] = 0.0;
    Vector dataTV;
    double fiberY[10000];
    double fiberZ[10000];
    double fiberArea[10000];

    for (int i = 0; i < numFibers; i++) {
        fiberY[i] = matData[3 * i];
        fiberZ[i] = matData[3 * i + 1];
        fiberArea[i] = matData[3 * i + 2];
    }

    for (int i = 0; i < numFibers; i++) {
        // initializing material strain and set it
        UniaxialMaterial *theMat = theMaterials[i];
        double secant = 0;
        double tangent = 0.0;
        double ThermalElongation = 0.0;
        double FiberTemperature = 0;
        double FiberTempMax = 0;

        if (fabs(DataMixed(1)) <= 1e-10 && fabs(DataMixed(49)) <= 1e-10)
        {
            FiberTemperature = 0;
            FiberTempMax = 0;
        }
        else
        {
            //calculate the fiber temp, T=T1-(Y-Y1)*(T1-T2)/(Y1-Y2)
            FiberTemperature = this->determineFiberTemperature(DataMixed,
                -fiberY[i], fiberZ[i]);
        }

        // get the data from thermal material
    }
}
```

```

static Vector tData(4);
static Information iData(tData);
tData(0) = FiberTemperature;
tData(1) = tangent;
tData(2) = ThermalElongation;
tData(3) = FiberTempMax;
iData.setVector(tData);
theMat->getVariable("ElongTangent", iData);
tData = iData.getData();
ThermalElongation = tData(2);
tangent = tData(1);

double y = fiberY[i];
double z = fiberZ[i];
double A = fiberArea[i];
double strain = theMat->getStrain(); //gives mechanical strain
double stress = theMat->getStress();
if (strain == 0) {
    secant = theMat->getInitialTangent();
}
else {
    secant = abs(stress / strain);
}
double EA = secant * A;
double EAy = EA * y;
double EAz = EA * z;
stiffnessData[0] += EA;
stiffnessData[1] += EAy;
stiffnessData[2] += EAz;
}

cData[0] = stiffnessData[1] / stiffnessData[0]; //EAy/EA;
cData[1] = stiffnessData[2] / stiffnessData[0]; //EAz/EA;

return *c;
}

```

A.2 Functions developed for *FireEl3d*-class

The following functions of the *FireEl3d* class that are presented were modified in order to account for the eccentric NA of the FBE.

A.2.1 *addLoad*-function

The *addLoad*-function receives a element load or thermal action and converts it to an equivalent nodal load. The *addLoad*-function only had to be modified to receive 25 temperature points. The code regarding the mechanical loads remained unchanged.

```
int
FireEl3d::addLoad(ElementalLoad *theLoad, double loadFactor)
{
    int type;
    const Vector &data = theLoad->getData(type, loadFactor);
    double L = crdTransf->getDeformedLength();

    if (type == LOAD_TAG_Beam3dUniformLoad) {
        double wy = data(0)*loadFactor; // Transverse
        double wz = data(1)*loadFactor; // Transverse
        double wx = data(2)*loadFactor; // Axial (+ve from node I to J)

        double Vy = 0.5*wy*L;
        double Mz = Vy * L / 6.0; // wy*L*L/12
        double Vz = 0.5*wz*L;
        double My = Vz * L / 6.0; // wz*L*L/12
        double P = wx * L;

        // Reactions in basic system
        p0[0] -= P;
        p0[1] -= Vy;
        p0[2] -= Vy;
        p0[3] -= Vz;
        p0[4] -= Vz;

        // Fixed end forces in basic system
        q0[0] -= 0.5*P;
        q0[1] -= Mz;
        q0[2] += Mz;
        q0[3] += My;
        q0[4] -= My;
    }
    else if (type == LOAD_TAG_Beam3dPointLoad) {
        double Py = data(0)*loadFactor;
        double Pz = data(1)*loadFactor;
        double N = data(2)*loadFactor;
        double aOverL = data(3);

        if (aOverL < 0.0 || aOverL > 1.0)
            return 0;

        double a = aOverL * L;
        double b = L - a;

        // Reactions in basic system
        p0[0] -= N;
        double V1, V2;
        V1 = Py * (1.0 - aOverL);
```

```

V2 = Py * aOverL;
p0[1] -= V1;
p0[2] -= V2;
V1 = Pz * (1.0 - aOverL);
V2 = Pz * aOverL;
p0[3] -= V1;
p0[4] -= V2;

double L2 = 1.0 / (L*L);
double a2 = a * a;
double b2 = b * b;

// Fixed end forces in basic system
q0[0] -= N * aOverL;
double M1, M2;
M1 = -a * b2 * Py * L2;
M2 = a2 * b * Py * L2;
q0[1] += M1;
q0[2] += M2;
M1 = -a * b2 * Pz * L2;
M2 = a2 * b * Pz * L2;
q0[3] -= M1;
q0[4] -= M2;
}
else if (type == LOAD_TAG_BeamThermalAction) {
    counterTemperature = 1;
    for (int i = 0; i < 5; i++) {
        residThermal[i] = 0;
    }

    Vector dataMixV(75);
    for (int m = 0; m < 25; m++) {
        dataMixV(2 * m) = data(2 * m);
        dataMixV(2 * m + 1) = data(2 * m + 1);
        dataMixV(50 + m) = 1000;
    }

    for (int m = 0; m < 75; m++) {
        dataMix[m] = dataMixV(m);
    }

    const Vector &s1 = theSections[0]->getTemperatureStress(dataMixV);
    const Vector &s2 = theSections[numSections - 1]
        ->getTemperatureStress(dataMixV);
    residThermal[0] += (s1(0) + s2(0)) / 2;
    residThermal[1] -= s1(1);
    residThermal[2] += s2(1);
    residThermal[3] -= s1(2);
    residThermal[4] += s2(2);

    AverageThermalElong = 0;
}
else {
    opserr << "FireEl3dBi::addLoad() -- load type unknown for element with tag: "
        << this->getTag() << endl;
    return -1;
}

return 0;
}

```


A.2.2 *update-function*

In the *update*-function updates the strains and curvature of the cross-sections and calculates the updated NA for the FBE. The calculation of the axial strain and curvature of the cross-sections had to be modified to account for eccentricity of the NA.

```
int
FireEl3d::update(void)
{
    int err = 0;

    // Update the transformation
    crdTransf->update();

    // Get basic deformations
    const Vector &v = crdTransf->getBasicTrialDisp();
    double L = crdTransf->getDeformedLength();
    double oneOverL = 1.0 / L;

    Vector e(workArea, 4);

    // For Node A
    e(0) = oneOverL * (v(0) - 3.0*cy*(v(1) + v(2)) + 3.0*cz*(v(3) + v(4)))
           - AverageThermalElong + SectionThermalElong[0];
    e(1) = oneOverL * (-6.0 * oneOverL*cz*v(5) - 4.0 * v(1) - 2.0 * v(2));
    e(2) = oneOverL * (-6.0 * oneOverL*cy*v(5) - 4.0 * v(3) - 2.0 * v(4));
    e(3) = oneOverL * (v(5));
    err += theSections[0]->setTrialSectionDeformation(e);

    // For Node B
    e(0) = oneOverL * (v(0) + 3.0*cy*(v(1) + v(2)) - 3.0*cz*(v(3) + v(4)))
           - AverageThermalElong + SectionThermalElong[0];
    e(1) = oneOverL * (6.0 * oneOverL*cz*v(5) + 2.0 * v(1) + 4.0 * v(2));
    e(2) = oneOverL * (6.0 * oneOverL*cy*v(5) + 2.0 * v(3) + 4.0 * v(4));
    e(3) = oneOverL * (v(5));
    err += theSections[numSections - 1]->setTrialSectionDeformation(e);

    this->updateC();

    if (err != 0) {
        opserr << "FireEl3dBi::update() - failed setTrialSectionDeformations()\n";
        return err;
    }
    return 0;
}
```

A.2.3 *getTangentStiff-function*

The *getTangentStiff*-function calculates the finite element matrices of the FBE that is used in the global analysis. The function was modified to convert the section properties and forces from the RA to the NA and to calculate the modified stiffness matrix of the FBE.

```
const Matrix&
FireEl3d::getTangentStiff()
{
    double L = crdTransf->getDeformedLength();

    //ELASTIC STIFFNESS MATRIX
    //assemble the basic (6x6) compressed form of the elastic stiffness matrix kb
    static Matrix kb(6, 6);

    // Zero for integral
    kb.Zero();
    q.Zero();

    //get section proerties from FireFiberSection
    //For Node A
    const Matrix ks1 = theSections[0]->getSectionTangent();
    double EIz1 = ks1(1, 1) + cy * ks1(0, 1) + cy * ks1(1, 0) + cy * cy*ks1(0, 0);
    double EIy1 = ks1(2, 2) - cz * ks1(0, 2) - cz * ks1(2, 0) + cz * cz*ks1(0, 0);
    double EIyz1 = ks1(1, 2) + cy * ks1(2, 0) - cz * ks1(1, 0) - cy * cz*ks1(0, 0);

    //Fore Node B
    const Matrix ks2 = theSections[numSections - 1]->getSectionTangent();
    double EIz2 = ks2(1, 1) + cy * ks2(0, 1) + cy * ks2(1, 0) + cy * cy*ks2(0, 0);
    double EIy2 = ks2(2, 2) - cz * ks2(0, 2) - cz * ks2(2, 0) + cz * cz*ks2(0, 0);
    double EIyz2 = ks2(1, 2) + cy * ks2(2, 0) - cz * ks2(1, 0) - cy * cz*ks2(0, 0);

    double EAoverL = (ks1(0, 0) + ks2(0, 0)) / (2.0*L);
    double EIzoverL2 = (EIz1 + EIz2) / L;
    double EIyoverL2 = (EIy1 + EIy2) / L;
    double EIyzoverL2 = (EIyz1 + EIyz2) / L;

    double EIzoverL4 = 2 * EIzoverL2;
    double EIyoverL4 = 2 * EIyoverL2;
    double EIyzoverL4 = 2 * EIyzoverL2;

    kb(0, 0) = EAoverL;
    kb(1, 1) = kb(2, 2) = EIzoverL4;
    kb(3, 3) = kb(4, 4) = EIyoverL4;

    kb(1, 2) = kb(2, 1) = EIzoverL2;
    kb(3, 4) = kb(4, 3) = EIyoverL2;

    kb(1, 3) = kb(3, 1) = kb(2, 4) = kb(4, 2) = EIyzoverL4;
    kb(1, 4) = kb(4, 1) = kb(2, 3) = kb(3, 2) = EIyzoverL2;

    if (theSections[0]->getOrder() >= 4)
    {
        kb(5, 5) = (ks1(3, 3) + ks2(3, 3)) / (2.0*L);
    }

    //create Qk which shifts matrix in basic form
    Matrix Qb(6, 6);
    Qb.Zero();
    Qb(0, 0) = Qb(1, 1) = Qb(2, 2) = Qb(3, 3) = Qb(4, 4) = Qb(5, 5) = 1;
    Qb(0, 1) = cy; Qb(0, 2) = -cy;
```

```

Qb(0, 3) = -cz; Qb(0, 4) = cz;
Qb(1, 5) = Qb(2, 5) = cz / L;
Qb(3, 5) = Qb(4, 5) = cy / L;

//initialise k_12 : stiffness around reference axis, and include shift
Matrix kb_12(6, 6);
kb_12.Zero();
kb_12.addMatrixTripleProduct(1, Qb, kb, 1); //transform basic matrix

//GEOMETRIC STIFFNESS MATRIX
//is not in a compressed form, but already in a local form : 6x6
//get load vector from FireFiberSection

//For Node A
const Vector resultant1 = theSections[0]->getStressResultant();

//For Node B
const Vector resultant2 = theSections[numSections - 1]->getStressResultant();

q(0) = 0.5*resultant1(0) + 0.5*resultant2(0);
q(1) = -resultant1(1);
q(2) = resultant2(1);
q(3) = -resultant1(2);
q(4) = resultant2(2);
q(5) = 0.5*resultant1(3) + 0.5*resultant2(3);

q(5) -= (cy*q(1) + cy * q(2) + cz * q(3) + cz * q(4)) / L;
q(4) -= q(0)*cz;
q(3) += q(0)*cz;
q(2) += q(0)*cy;
q(1) -= q(0)*cy;

// Add effects of element loads, q = q(v) + q0

q(0) += q0[0];
q(1) += q0[1];
q(2) += q0[2];
q(3) += q0[3];
q(4) += q0[4];

// Transform to global stiffness
K = crdTransf->getGlobalStiffMatrix(kb_12, q, cy, cz);

return K;
}

```

Appendix B – SPM software input details for the design example of the ten-storey office building

Figure B.1 present the input regarding the loading of the slab panel, the geometry of the slab panel and the reinforcement of the slab and secondary beams. These input remained the same during the iterative process when the ultimate load-carrying capacity of the slab panel were determined. The limiting deflection of the slab panel were manually updated for each iteration under the Research-tab of the SPM software.

Fire Load Energy Density MJ/m² Fire Hazard Category

☐ Fire Cell

Inside height of firecell, H m
 Area of vertical Openings, A_v m²
 Floor area of firecell, A_f m²
 Construction Material
 Thermal inertia for firecell, b J/m² Cs^{0.5}

☒ Time Equivalent

Time equivalent, t_{eq} min

Applied load

w* kN/m²

(w* must include the floor system self weight)

Slab mesh reinforcement and concrete strength

f_c'20 MPa
 Rib height or depth, h_{rc} mm
 Total slab thickness, t₀ mm
 Slab type

Reinforcement details

Reinforcement layer 2 used?

	Reinforcement layer 1	Reinforcement layer 2
f _{yr} 20, reinforcement	<input type="text" value="420"/> MPa	<input type="text" value="0"/> MPa
TOP cover x direction, C _{xre0}	<input type="text" value="51"/> mm	<input type="text" value="0"/> mm
TOP cover y direction, C _{yre0}	<input type="text" value="45"/> mm	<input type="text" value="0"/> mm
bar spacing in x, S _{xre0}	<input type="text" value="150"/> mm	<input type="text" value="0"/> mm
bar diameter in x, d _{xre0}	<input type="text" value="6"/> mm	<input type="text" value="0"/> mm
bar spacing in y, S _{yre0}	<input type="text" value="150"/> mm	<input type="text" value="0"/> mm
bar diameter in y, d _{yre0}	<input type="text" value="6"/> mm	<input type="text" value="0"/> mm
Reinforcement type	<input type="text" value="Cold-worked mesl"/>	<input type="text" value="Hot-formed"/>

Compression Reinforcement

f_{yr}20,cr MPa
 cover to bottom, C₃ mm
 bar diameter, d_{cr} mm
 Number of bars

Slab panel and support beam dimensions

L_x, slab panel m
 L_y, slab panel m
 L_{xb}, max m
 L_{yb}, max m

Slab panel edge conditions

Side 1
 Side 3
 Side 2
 Side 4

Sides 1 to 4 can be either simple or fixed. Select fixed if the side is able to resist bending moment and that moment capacity is to be included in the slab panel capacity. Select simple otherwise. If the side cannot resist bending moment then select simple. For example, in the diagram shown, slab panel 1 side 3 can resist bending moment across into slab panel 2 and so can be fixed or simple. Sides 1, 2 and 4 are on the edge of the building and cannot resist bending moment so must be selected as simple.

Secondary beam input

Secondary Beam
 Beam direction (Lx is default)

Top Flange

Beam top flange yield stress, f_ytsb20 MPa
 Beam top flange width, b_f,t_f mm
 Beam top flange thickness, t_f,t_f mm

Web

Beam web yield stress, f_ywsb20 MPa
 Beam web thickness, t_w mm
 (set to 0 for continuous web openings)
 Depth of web openings mm

Bottom Flange

Beam bottom flange yield stress, f_ybsb20 MPa
 Beam bottom flange width, b_f,b_f mm
 Beam bottom flange thickness, t_f,b_f mm

Beam depth, d mm
 Beam spacing, S_{sb} m
 Beam shear capacity, φ_i V_v kN

Speedfloor joist Input

Joist spacing m

Interior support bars, x direction

f_{yr}20, isbx MPa
 bar diameter mm
 bar spacing mm
 Top Cover mm

Interior support bars, y direction

f_{yr}20, isby MPa
 bar diameter mm
 bar spacing mm

Slab reinforcement; deck trough bars

f_{yr}20,dtb MPa
 bar diameter mm
 bar spacing mm

BOTTOM covers for heat flow calculations

c1 mm
 c2 mm
 c3 mm

Secondary beam to primary beam connection

No. of bolts in each secondary beam to primary beam connection
 Ambient temperature design shear capacity of bolt, (φ_i V_{fn}) kN

Figure B.1: Input details of the slab panel for the ten-storey building for the SPM software

Appendix C – One-dimensional heat transfer of concrete slabs

The one-dimensional heat transfer calculations to obtain the temperatures within the concrete slabs and results are presented in this Appendix.

C.1 Second Munich Test

The temperatures obtained for the concrete slab for the Second Munich Test are presented in Table C.1.

Table C.1: Temperatures within the concrete slab determined with heat transfer calculations for the Second Munich Test

Time [mm]	Depth of slab from top (unexposed face) [mm]													
	111.8	103.2	94.6	86	77.4	68.8	60.2	51.6	43	34.4	25.8	17.2	8.6	0
0	20	20	20	20	20	20	20	20	20	20	20	20	20	20
10	115	73	48	33	26	22	21	20	20	20	20	20	20	20
20	424	210	112	75	54	40	32	27	24	22	21	20	20	20
30	651	413	264	166	108	78	57	44	35	29	25	23	22	21
40	762	536	375	260	178	123	92	70	54	43	35	30	27	25
50	704	569	437	328	242	175	127	97	77	61	50	41	35	31
60	602	528	440	355	279	216	164	125	99	80	65	54	45	39
70	522	478	419	356	295	239	190	150	119	97	80	67	56	47
80	466	437	395	347	297	250	207	168	136	111	93	78	65	54
90	404	391	365	331	293	254	216	181	150	124	103	87	73	60

C.2 Cardington Corner Test (Test 3)

The temperatures obtained for the concrete slab for the Cardington Corner Test (Test 3) are presented in Table C.2.

Table C.2: Temperatures within the concrete slab determined with heat transfer calculations for the Cardington Corner Test (Test 3).

Time [mm]	Depth of slab from top (unexposed face) [mm]													
	102.8	94.9	87.0	79.1	71.2	63.3	55.4	47.4	39.5	31.6	23.7	15.8	7.9	0
0	22	22	22	22	22	22	22	22	22	22	22	22	22	22
10	22	22	22	22	22	22	22	22	22	22	22	22	22	22
20	56	44	35	30	26	24	23	22	22	22	22	22	22	22
30	130	106	86	71	58	49	42	36	32	30	28	28	28	28
40	216	175	144	119	99	84	72	62	55	50	46	44	44	44
50	361	280	224	184	154	130	112	98	87	78	73	69	67	66
60	512	404	329	272	228	193	165	143	126	112	102	94	88	84
70	744	559	443	361	302	256	219	191	167	149	134	121	111	108
80	820	658	537	446	375	319	274	237	207	181	158	138	125	117
90	766	660	566	486	419	362	314	274	239	209	183	164	149	140
100	674	616	553	493	436	386	341	302	267	238	212	189	173	163
110	601	565	523	479	435	394	355	320	288	259	234	211	192	181
120	542	521	492	460	426	392	359	329	300	273	249	226	210	200
130	489	477	458	436	411	384	357	330	305	280	258	236	222	210

C.3 Design Example: Ten-storey office building

The temperatures obtained for the concrete slab of the ten-storey office building are presented in Table C.3

Table C.3: Temperatures within the concrete slab determined with heat transfer calculations for the design example of the ten-storey building

Time [mm]	Depth of slab from top (unexposed face) [mm]										
	107.5	96.75	86	75.25	64.5	53.75	43	32.25	21.5	10.75	0
0	20	20	20	20	20	20	20	20	20	20	20
10	355	185	103	65	43	31	25	22	21	20	20
20	585	361	228	143	97	69	51	39	32	28	26
30	708	475	327	225	155	110	84	66	53	46	43
40	783	553	400	291	213	154	116	94	79	70	65
50	835	612	458	345	262	199	152	120	102	92	87
60	875	659	505	391	305	239	188	150	124	109	101